*MSC THESIS REPORT*:

# *DESIGN AND REALIZATION OF A SETUP FOR MECHANICAL TESTS ON A MEMS BASED MICRO GRAVITY-GRADIOMETER*

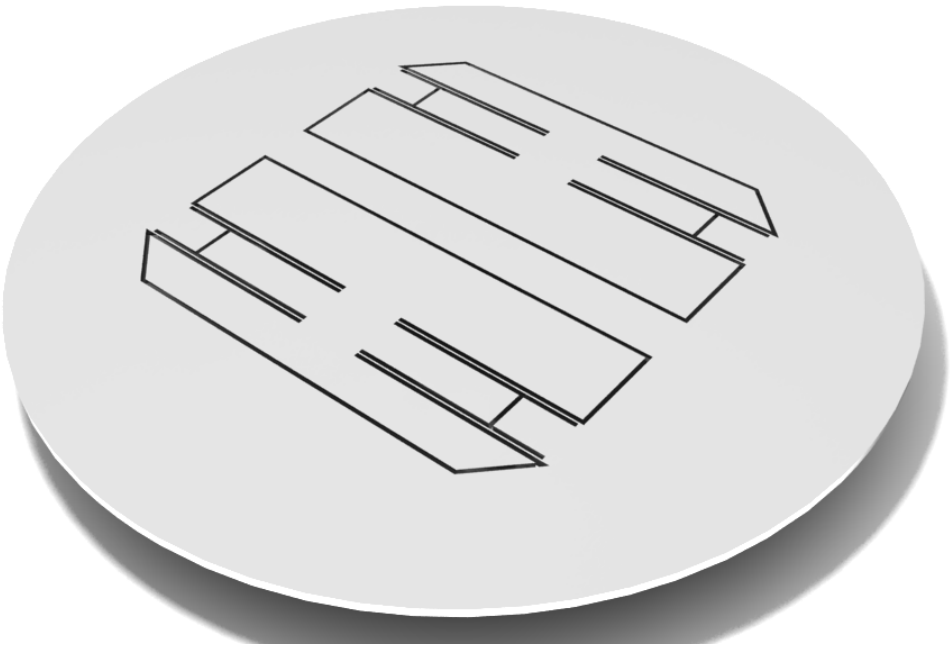


DELFT UNIVERSITY OF TECHNOLOGY
FACULTY OF AEROSPACE ENGINEERING
DEPARTMENT OF EARTH OBSERVATION AND SPACE SYSTEM (DEOS), ASTRODYNAMICS AND SATELLITE SYSTEMS

**CANDIDATE:**
ALESSANDRO DE SIMONE
STUDENT NO.:1287680

**SUPERVISORS:**
DR. IR. P.N.A.M. VISSER –DELFT UNIVERSITY OF TECHNOLOGY
DR. IR. J. FLOKSTRA, IR. R. CUPERUS – UNIVERSITY OF TWENTE
DR. J. M. SMIT – SRON

# 1. Introduction

The work presented in this report is a part of a project involving TUDelft, SRON, UTwente within MicroNed program. MicorNed program is supported by Dutch Government and it is aimed to increase and spread knowledge in the field of Micro System Technology (MST) and Micro Electro-Mechanical Systems (MEMS). [1]

The project is aimed to the development of an innovative micro gravity-gradiometer based on MEMS (Micro Electro-Mechanical Systems) technology.

A gravity-gradiometer is a device capable to measure the gradient of the gravity field of an object by performing a differential measurement of two masses. Knowledge of the gravity field of a celestial object carries several information regarding the composition and the inner structure of the object. It has a crucial role in defining processes of planet formation and evolution.

Measurement of the gravity field is often the only way to derive this kind of information; other approaches, seismology for instance, need to have sensors placed on the surface of the planet. This operation is always extremely difficult to realize; so far, planetary missions comprising this objective have been only planned for the Moon and Mars.

This makes remote measurements of the gravity field the only suitable technique for planetary missions. Gradiometry is not the only gravity field remote retrieval technique. Satellite-to-satellite tracking is also a widely used technique both for Earth observation and planetary missions. This technique, however, is especially sensible to lower degrees of the harmonic expansion of the gravity field potential, while gradiometry is more sensitive to higher degrees (more information about this argument can be found in [2]). The two techniques are, hence, substantially complementary.

Another major advantage of the innovative micro-gradiometer is represented by its dimensions and weight. The only gravity-gradiometer adapted for space missions is the one onboard the ESA's mission GOCE. This instrument has a baseline (distance between the two test masses) of *0.5* meter and an overall weight (electronics and subsystems, like cooling apparatus, included) of several hundreds of kg. The MEMS based micro gravity-gradiometer will have a *5 cm* long baseline and an overall weight of few kg. This makes the instrument particularly suitable for planetary missions. Several preliminary studies have been performed to test the capability of the instrument in missions to the Moon, Mars and Jovian system, with focus on Jovian moon, Europa [7], [8], [18].

The main efforts are now directed to the development of a ground demonstrator of the micro gravity-gradiometer able to verify that the principles can work and that the theoretical design (performed at UTwente by R. Cuperus [38]) can be realized.

The work presented in this report has the goal to design and realize a test setup specifically dedicated to perform mechanical tests on the prototype of the micro gravity-gradiometer. The innovative and unusual design of the micro gravity-gradiometer makes it impossible to be tested by normal apparatus development for testing both MEMS structures and accelerometers.

The micro gravity-gradiometer will be composed of two masses attached to a frame by means of springs. This structure will be etched on a *10 cm* diameter silicon wafer using DRIE (Deep Reaction Ion Etch) technique. The resulting structure can be regarded and analyzed as a mass-spring system. The expected system will be characterized by a low resonance frequency $\omega_n$ (in the *1-10 Hz* bandwidth) and high quality factor $Q$ (values of the quality factor for MEMS structures can reach $10^5$). The scope of the tests that will be performed on the structure by means of the setup presented in this report will be to determine the values of the resonance frequency $\omega_n$, spring constant $k$ and quality factor $Q$.

The basic idea is thus to excite the structure with an external signal and measure its response. In practice a frequency response or a step response of the system has to be measured.

The tests have to be performed under specific conditions; these conditions make the setup so particular. They have to be performed under vacuum in order to minimize Brownian noise and air damping. The movement of the masses has to be in horizontal direction (in-plane direction) in order to minimize the effect of the local gravity vector. The amplitude of the input signal needs to be very small (*1 μm* or less) since the gap between the masses and the frame is only *50 μm*. The signal amplitude has to be provided with enough accuracy. The frequency of the input signal (in the case of frequency response) has to be low (*1-10 Hz*). This is not a usual condition for MEMS structure and the low frequency bandwidth is the one that presents the biggest problems in terms of external noise. Finally, the (small) displacement of the masses has to be recorded and analyzed with high accuracy. Since the system has to be placed in a vacuum chamber, optical read-out systems, like laser interferometry or based on Doppler Effect, would add huge complexity to the test setup, for they would need space, glasses, compensation chambers and so on. Moreover, the setup needs to be flexible, since the further step for development of the prototype will be to include capacitive read-out to the structure, the setup should be able to perform tests with these different conditions as well.

From close look to the required conditions, it is possible to recognize that the most delicate choice involves the actuator (instrument that has the role to provide the input signal). In the end a piezo-electrical actuator has been selected. For what concerned the read-out system, a Micro System analyzer for MEMS structure, present at TST (Transducers Science and Technology) department at University of Twente, has been chosen as suitable read-out. Although the machine is primarily designed for vertical, high frequency displacement analysis, it still offers good accuracy and reliability for our conditions. A this point, some structures (vacuum chamber and support structures) have been designed and realized in order to meet all the other requirements (like vacuum and in-plane actuation).

*Report Structure*

Chapter 2 is dedicated to a theoretical introduction to the gradiometry technique: description of the mathematical framework of the technique, an example of possible application of the instrument and a survey of the gradiometry/accelerometry state of art.

Chapter 3 presents a more detailed description of the MEMS based micro gravity-gradiometer design and some issues regarding its realization. All the elements that compose the structure are described: proof masses, springs, damping to air, electrical read-out. Further in the chapter, a mathematical description of the mass-spring system is provided. This model will be used to define the characteristics of the micro-gravity gradiometer, regarded as a mass-spring system. The chapter is concluded by a brief description of the processing

technique that will be used to etch out the system from a silicon wafer, and a description of the most common errors, due to the technique, that may be present in the structure.

In chapter 4, the test setup is described in details. The test concept will be presented and then, all the elements that compose the setup are described and analyzed, namely: the piezo-electrical actuator, the supporting structures and the vacuum chamber. Finally, the read-out system is presented. The working principle of the acquisition system, its advantages and weak points will be discussed.

Chapter 5 presents the results of the calibration of the test setup. The tests performed are:

- Vacuum tests: in order to check that all the connections of the vacuum chamber are tight and not affected by leakage, and to define an out-gassing procedure.

- Quasi-static measurements: in order to define the behavior of the piezo-electric actuator in DC (quasi-static) operation. This behavior is largely dominated by hysteresis.

- Dynamic measurements: in order to define the behavior of the whole assembled test setup in dynamic operations. Linear region, peak(s) in displacements, cut-off frequency will be measured. The output of this kind of tests will be a bode plot of the test setup that will define the performance of the systems in terms of useful bandwidth.

- Noise characterization: the tests on the micro gravity-gradiometer will involve very small displacements; a quiet environment is a major requirement. Two error sources are considered and analyzed: environmental noise and electrical noise.

Finally, a simulation test has been designed to challenge the setup with a system with characteristics that are similar to the ones of the micro gravity-gradiometer: low resonance frequency and high quality factor.

Chapter 6, in the end, presents the conclusions and the outlook of the work.

# 2. Gradiometry

## 2.1. Mathematical foundations of Gradiometry

A gradiometer is a device capable to measure the gradient of the gravity field of an object by measuring the differential motion of two proof masses. According to the Equivalence Principle, announced by Einstein in 1907, it is not possible to distinguish between inertial and gravitational acceleration in a single point or in a differential region around it. One way to isolate the two components of the acceleration is to perform an acceleration measurement in two different points separated by a finite distance (not differential distance). The difference between these two measurements is an approximation of the gradient of the gravity field.

This section presents the mathematical framework behind a gradiometry measurement. [3]

### 2.1.1. Gradiometry Principles

In order to separate the two contribution of the so called *Specific Force* (*inertial* and *gravitational* accelerations) we need to introduce a model for the gravity field. As already pointed out, the equivalence of gravitational and inertia holds only for a single point (single proof mass) or for a differential region around it, so small that gravitational field can still be considered uniform.

The classical Newtonian theory of universal gravitation states that an object 1 exerts a force $\overline{F}_{12}$ on an object 2; this force is:

$$\overline{F} = -G\frac{m_1 m_2}{l_{12}^2}\overline{e}_{12} \tag{2.1}$$

Where $G$ is the gravitational constant (it is only known to the third digit and probably the fundamental constant with the largest uncertainty; its value is $G=6.67\cdot10^{-11}\ Nm^2kg^{-2}$); $m_1$ is the heavy mass of the first object; $m_2$ is the heavy mass of the second object; $l_{12}$ is the distance between object 1 and object 2; $\overline{e}_{12}$ is the unit vector from object 1 to object 2.

It is customary, when referring to the gravitation property of an object, to speak in terms of *field strength* or *intensity*. In order to introduce the concept of field strength we need to write the inverse square law with the help of a field function. It describes the gravitational field of those particles which are considered the attracting particles (the active masses). The active attracting particle with active heavy mass $m_Q$ at location $Q$ (the so called source-point), generates a gravitational field at every point $x \in R^3$ with strength:

$$\overline{a}_Q(x) = -Gm_Q\frac{x - x_Q}{\left|x - x_Q\right|^3} \tag{2.2}$$

The field is measured in $m/s^2$ or, in CGS units, in *gal* (short for Galileo), $1gal=10^{-2}$ $m/s^2$ ($1mgal=10^{-5}$ $m/s^2$).

Mathematical consideration around the structure of the field strength leads to the conclusion that the attraction field is a rotational free vector (consequence of the second basic equation of the gravitational field, see [4]) and, therefore, it can be written as the gradient of a scalar field *V*, the so called *Gravitational Potential* (measured in $m^2/s^2$):

$$\bar{a} = \nabla V \tag{2.3}$$

Another important property of the gravitational field states that the flux of $\bar{a}$ through any closed surface *S* is $-4\pi G$ times the total mass *M* within *S* (consequence of the first basic equation of the gravitational field, see [4]). This property is expressed by the equation:

$$div\bar{a} = div\left(\nabla V\right) = \nabla^2 V = -4\pi G\rho \tag{2.4}$$

Equation (2.4) is also known as *Poisson Equation*. In an area with $\rho=0$ (free-mass area), equation (2.4) becomes:

$$div\bar{a} = div\left(\nabla V\right) = \nabla^2 V = 0 \tag{2.5}$$

Equation (2.5) is known as *Laplace Equation*. The gravitational potential of a mass fulfils the Laplace equation outside the mass and the Poisson equation inside the mass.

We can now introduce the *Gradient of the attraction field*:

$$\Gamma = \nabla\bar{a} \tag{2.6}$$

Using the relation $\bar{a} = \nabla V$, we obtain:

$$\Gamma = \nabla\left(\nabla V\right) \tag{2.7}$$

$\Gamma$ is a tensor, defined as:

$$\Gamma = \begin{pmatrix} V_{xx} & V_{xy} & V_{xz} \\ V_{yx} & V_{yy} & V_{yz} \\ V_{zx} & V_{zy} & V_{zz} \end{pmatrix} \tag{2.8}$$

The quantity $\Gamma$ is called *Eötvös Tensor*. Since $rot\bar{a} = 0$, the Eötvös tensor is symmetric: $V_{ij} = V_{ji}$. Moreover, the diagonal elements fulfil in mass free area ($\rho=0$) the equation:

$$V_{11} + V_{22} + V_{33} = 0 \tag{2.9}$$

The gradient of the gravity force has many applications in geological and planetary exploration fields, since it can provide valuable information about anomalous mass distribution in the shallow sub-surface of an object (see [4], [5] and section 2.2).

### 2.1.2. Basic Equations

It is possible to determine the components of the Eötvös Tensor by means of a gravity gradiometer. The basic working principle of a gradiometer is the following: it measures the relative acceleration of two or more test masses under the influence of the gravitational field of an object.

Let us consider the motion of a proof mass $m_1$ with respect to another proof mass $m_2$ under the gravitational influence of a third mass $m_3$. Within this representation, $m_1$ and $m_2$ may be two proof masses onboard a satellite while $m_3$ may represent any celestial object which gravitational field we want to determine.

After mathematical manipulation (see [4] for a more complete derivation), we can describe the motion of the proof mass $m_2$ with respect to $m_1$, under the influence of a third body $m_3$ as:

$$\mu_{12}\ddot{R}_{12} = G_{(21)3} + m_2 g_1\left(R_2\right) \tag{2.10}$$

Where the quantity:

$$G_{(21)3} = \mu_{12}\left[g_3\left(R_2\right) - g_3\left(R_1\right)\right] \tag{2.11}$$

is said *Tidal Force*; it is the difference between the gravitational interaction of $m_1$ and $m_2$ respectively, with $m_3$; the quantity:

$$\mu_{12} = \frac{m_1 m_2}{m_1 + m_2} \tag{2.12}$$

is referred to as *Reduced Mass*.

A Gravity Gradiometer is capable to directly measure the tidal force $G_{(21)3}$. It can be found in two variants:

- In-line Gradiometer: it measures the force difference between two proof masses in direction of $R_{12}$ i.e. in the direction of the line connecting the two masses.
- Cross-component gradiometer: the two proof masses are rigidly connected and the angular momentum generated by the tidal field is measured.

In reality, each test mass is an accelerometer itself. They must be precisely located with respect to each other. When taking the difference between the acceleration they measure and dividing by the distance between the accelerometers, we obtain an approximation of the second derivative of the gravitational potential (described by the components of the Eötvös Tensor) in the direction connecting the two proof masses.

### 2.1.3. Observables for SGG

When the distance between the two proof masses is small (few decimetres or less) as in the case of a Gravity gradiometer, we can expand the specific gravitational force (force per unit of mass) due to $m_3$, acting on $m_1$ and $m_2$ respectively, $g_3(R_i)$, $i=1,2$ in a Taylor series around the point $R_s=(R_2+R_1)/2$:

$$g_3(R_i) = g_3(R_s) + \nabla g_3(R_s)(R_i - R_s) + o\left(|R_i - R_s|^2\right), \quad i = 1,2 \tag{2.13}$$

Neglecting quadratic and higher terms, and inserting equation (2.13) in equation (2.11), we obtain, for the tidal force, the approximation (remembering that $g = \nabla V$ ):

$$G_{(21)3} \approx \mu_{12} \nabla\left(\nabla V(R_s)\right) R_{12} \tag{2.14}$$

The tensor $\nabla(\nabla V)$ is again the gravitational (or Eötvös) tensor $\Gamma$, described in section 2.1.1. The elements of $\Gamma$ are the second derivatives of the gravitational potential of the body $m_3$. The equation of motion of $m_2$ with respect to $m_1$ is approximately:

$$\mu_{12}\ddot{R}_{12} \approx \mu_{12}\Gamma(R_s)R_{12} + m_2 g_1(R_2) \tag{2.15}$$

If the gravitational interaction between the two proof masses $m_1$ and $m_2$ is small (for instance, when the masses are small), we can neglect the term $m_2 g_1(R_2)$, and obtain:

$$\ddot{R}_{12} \approx \Gamma(R_s)R_{12} \tag{2.16}$$

Hence, if the distance of the two proof masses is $\Delta x$, we obtain, for the x-component of the acceleration:

$$\ddot{x} = V_{xx}\Delta x \Rightarrow V_{xx} = \frac{\ddot{x}}{\Delta x} \tag{2.17}$$

Analogously, we have for the other components:

$$V_{xy} = \frac{\ddot{y}}{\Delta x}, \quad V_{zx} = \frac{\ddot{z}}{\Delta x} \tag{2.18}$$

According to equations (2.17) and (2.18), the second derivatives of the gravitational potential can be determined from the relative acceleration of two proof masses onboard a satellite, measured in three different directions.

As an example, we report the orders of magnitude of the gravitational tensor components *Vij* of the Earth; they are:

$$V_{xx} = V_{yy} = -1540 \times 10^{-9}\, s^{-2} = -1540E$$
$$V_{zz} = 3080E$$
$$V_{xy} = V_{xz} = V_{yz} = 0$$

Where *x-axis* in North direction, *y-axis* is in East direction and *z-axis* in vertical direction. The physical quantities used for Earth are: $GM \approx 398600x10^{9}\ m^{3}s^{-2}$ and $R \approx 6.371x10^{6}\ m$, and 1 E (Eötvös) equal to $10^{-9}s^{-2}$. [6]

The analysis we discussed so far was based on the hypothesis that the axis of the instrument is not rotating. In this case we would measure gravity instead of gravitation. In reality, when we deal with an instrument onboard a satellite, the instrument axis is rotating together with the satellite about the planet; hence we need to study the behavior of the instrument in a rotating frame.

If we consider a point *i* (denoted by the position vector $x_i$) in a rotating reference frame fixed with respect to a satellite, the acceleration $\ddot{x}_i$ at that point would read as:

$$\ddot{x}_i \approx \left(\Gamma - \dot{\Omega} - \Omega^2\right) x_i \tag{2.19}$$

Equation (2.19) states that we cannot directly measure the gravitational acceleration ($\Gamma$) from a measurement in a rotating frame fixed to the satellite, but only the sum of the gravitational acceleration, centrifugal acceleration (term $\Omega^2$) and angular acceleration (term $\dot{\Omega}$). A detailed discussion about this topic can be found in [6] and [4]).

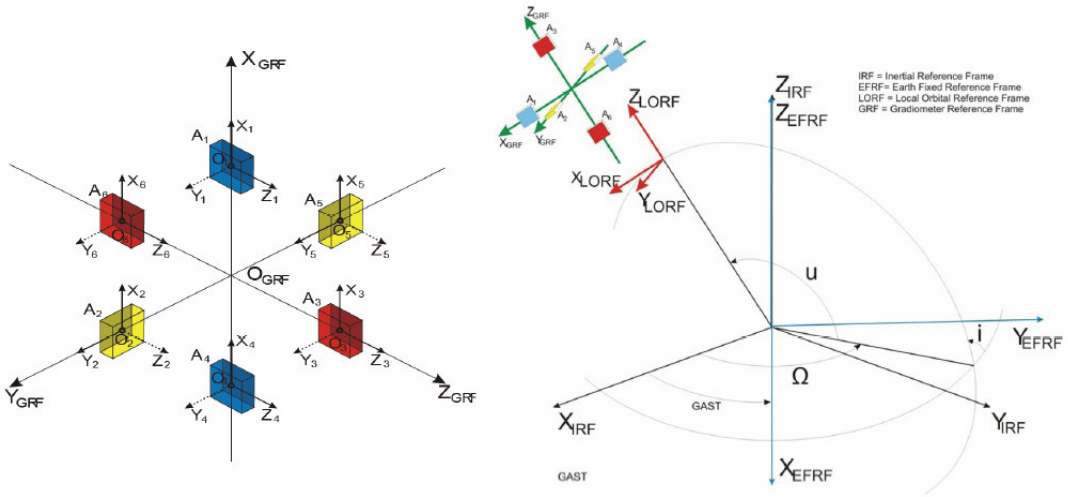


**Figure 2-1: Gravity gradiometer configuration and reference frame**

Let us consider a gradiometer configuration as shown in Figure 2-1, and let us take as example mass 1. We have:

$$R_{14} = \left( \frac{d_{14}}{2}, 0, 0 \right)^T \tag{2.20}$$

Where $d_{14}$ is the distance between mass 1 and mass 4. Furthermore, we have:

$$\ddot{R}_1 = \begin{pmatrix} V_{xx} + \omega_y^2 + \omega_z^2 \\ V_{xy} - \dot{\omega}_z + \omega_x \omega_y \\ V_{xz} - \dot{\omega}_y + \omega_x \omega_z \end{pmatrix} \tag{2.21}$$

For the relative acceleration between the proof masses 1 and 4, we can write:

$$\ddot{R}_{14} = \ddot{R}_1 - \ddot{R}_4 = \left( \Gamma - \dot{\Omega} - \Omega^2 \right) \left( x_1 - x_4 \right) \tag{2.22}$$

Then, we have:

$$\ddot{x}_{14} = \ddot{x}_1 - \ddot{x}_4 = d_{14} \left( V_{xx} + \omega_y^2 + \omega_z^2 \right) \tag{2.23}$$

$$\ddot{y}_{14} = \ddot{y}_1 - \ddot{y}_4 = d_{14} \left( V_{xy} - \dot{\omega}_z + \omega_x \omega_y \right) \tag{2.24}$$

$$\ddot{z}_{14} = \ddot{z}_1 - \ddot{z}_4 = d_{14} \left( V_{xz} - \dot{\omega}_y + \omega_x \omega_z \right) \tag{2.25}$$

In the same way we can derive equations for the accelerometers pairs. A closer inspection of $\Omega^2$ and $\dot{\Omega}$ shows that the former (like $\Gamma$) is symmetric while the latter is anti-symmetric. Thus a separation of $\Lambda = \Gamma - \dot{\Omega} - \Omega^2$,

$$\Lambda = \begin{pmatrix} V_{xx} - \left( \omega_y^2 + \omega_z^2 \right) & V_{xy} + \omega_x \omega_y + \dot{\omega}_z & V_{xz} + \omega_z \omega_x - \dot{\omega}_y \\ V_{yx} + \omega_x \omega_y - \dot{\omega}_z & V_{yy} - \left( \omega_z^2 + \omega_x^2 \right) & V_{yz} + \omega_z \omega_y + \dot{\omega}_x \\ V_{zx} + \omega_z \omega_x & V_{zy} + \omega_y \omega_z & V_{zz} - \left( \omega_x^2 + \omega_y^2 \right) \end{pmatrix} \tag{2.26}$$

Into symmetric and anti-symmetric parts yields:

$$\frac{1}{2} \left( \Lambda + \Lambda^T \right) = \Gamma + \Omega^2 \tag{2.27}$$

$$\frac{1}{2} \left( \Lambda - \Lambda^T \right) = \dot{\Omega} \tag{2.28}$$

And

$$trace \Lambda = \Lambda_{xx} + \Lambda_{yy} + \Lambda_{zz} = -2 \left( \omega_x^2 + \omega_y^2 + \omega_z^2 \right) = -2\omega^2 \tag{2.29}$$

Time integration of equation (2.28) yields angular velocities, which are then used to isolate Γ from $\Omega^2$ using equation (2.27). Moreover, the angular acceleration, equation (2.28), can be integrated and employed for the angular control of the spacecraft.

In more details, the angular accelerations can be isolated according to equation (2.28), which means that we have to form differences of two pairs of accelerometers measurements. For instance, we can show that:

$$\begin{aligned}\dot{\omega}_x &= \frac{\ddot{y}_{36}}{d_{36}} - \frac{\ddot{z}_{25}}{d_{25}} \\ \dot{\omega}_y &= \frac{\ddot{z}_{14}}{d_{14}} - \frac{\ddot{x}_{36}}{d_{36}} \\ \dot{\omega}_x &= \frac{\ddot{x}_{25}}{d_{25}} - \frac{\ddot{y}_{14}}{d_{14}}\end{aligned} \tag{2.30}$$

The angular velocities $\omega_x$, $\omega_y$, $\omega_z$ can be reconstructed by time integration of the last equations. Once they are known, the components of the gravitational tensor can be reconstructed:

$$\begin{aligned}&V_{xx} = \frac{\ddot{x}_{14}}{d_{14}} - \omega_y^2 - \omega_z^2, \quad V_{yy} = \frac{\ddot{y}_{25}}{d_{25}} - \omega_x^2 - \omega_z^2, \quad V_{zz} = \frac{\ddot{z}_{36}}{d_{36}} - \omega_x^2 - \omega_y^2 \\ &V_{yx} = \frac{\ddot{y}_{14}}{d_{14}} + \dot{\omega}_z - \omega_x\omega_y, \quad V_{xy} = \frac{\ddot{x}_{25}}{d_{25}} + \dot{\omega}_z - \omega_x\omega_y, \quad V_{zx} = \frac{\ddot{z}_{14}}{d_{14}} + \dot{\omega}_y - \omega_x\omega_z \\ &V_{xz} = \frac{\ddot{x}_{36}}{d_{36}} + \dot{\omega}_y - \omega_x\omega_z, \quad V_{zy} = \frac{\ddot{z}_{25}}{d_{25}} + \dot{\omega}_x - \omega_y\omega_z, \quad V_{yz} = \frac{\ddot{y}_{36}}{d_{36}} + \dot{\omega}_x - \omega_y\omega_z\end{aligned} \tag{2.31}$$

Note that $V_{ij}=V_{ji}$, because the gravitational tensor $\Gamma$ is symmetric and $V_{xx}+V_{yy}+V_{zz}=0$, since the tensor fulfils the Laplace's equation. The result is that only 5 component of the gravitational tensor are independent.

## 2.2. Application of Micro Gravity-Gradiometer

Knowledge of the gravity field, together with other measurable characteristics of a planet, such as mass, size, rotational period and so on, can provide information about the internal structure of the planet. Several mission proposal already formulated ([7], [8], [23]) could be suitable for carrying a micro gravity gradiometer in order to have gravity field retrieval of planets or moons.

A better understanding of the internal structure of planets and satellites is the next step to planetary exploration. Although the atmosphere and surface properties of most planets and satellites have been largely studied, the internal structure is almost unknown for all planets. Knowledge of the internal structure of a planet is fundamental information for theory about planet formation and evolution.

Interesting targets for such a mission would be Mars, the Moon and the Jovian satellite Europa (Figure 2-2).

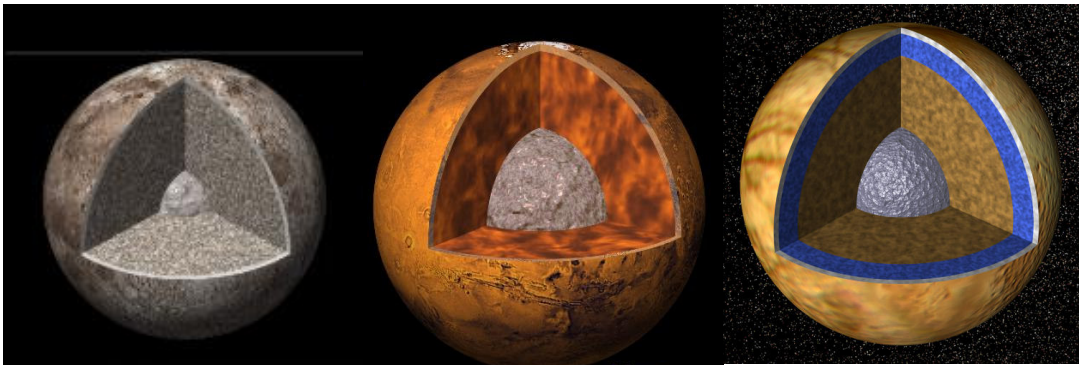

**Figure 2-2: Internal structure of Moon, Mars and Europa (in the picture the proportions are not respected)**

If we take Europa as example, the knowledge of its gravity field would be useful to gain information in different subjects. Table 1 lists the topic that may benefit form gravity field measurement and the required accuracy a gravity gradiometer should have. [9], [10], [11], [12], [13]

| ***Topic*** | ***Gravity Accuracy [mGal]*** | ***Spatial Resolution [km]*** |
|---|---|---|
| ***Ocean floor topography: canyon/trench*** | *0.5 – 1* | *70 – 140* |
| ***Volcanoes*** | *0.1 – 3* | *50 – 200* |
| ***Convection/ plumes*** | *<1* | *50 – 100* |
| ***Ocean currents*** | *<1* | *10 – 200* |
| ***Slush rheology*** | *1* | *>500* |
| ***Mantle rheology*** | *<1* | *<100* |
| ***Lateral heterogeneities*** | *<1* | *<100* |

**Table 1: Expected gravitational values for different features on Europa**

Those values have been taken as starting requirement for the development of an innovative MEMS based micro gravity gradiometer.

## 2.3. Approaches to Gradiometry

A gravity gradiometer is basically composed by two or more accelerometers; this section will briefly report the state of art of the accelerometry techniques.

### 2.3.1. Accelerometers sensitivity

The resolution of an accelerometers is governed by the sensitivity (or, the magnitude of the response for a given input), and the noise. [14]

The simplest representation of an accelerometer is a mass-spring system plus a read-out (see section 3.2 for a more complete description). It can be regarded as composed by a mechanical transducer converting acceleration in displacement (mass-spring system) and a displacement sensor (section 2.3.2). Transducers sensitivity can be improved by lowering the resonant frequency. All else being equal, a device with lower resonant frequency will exhibit better resolution. Since, however, reducing the resonant frequency also lowers the device's tolerance to mechanical shock, practical considerations set an application dependent lower bound on acceptable resonant frequency.

Figure 2-3 shows a comparison between noise floors of common commercial accelerometers. [14]

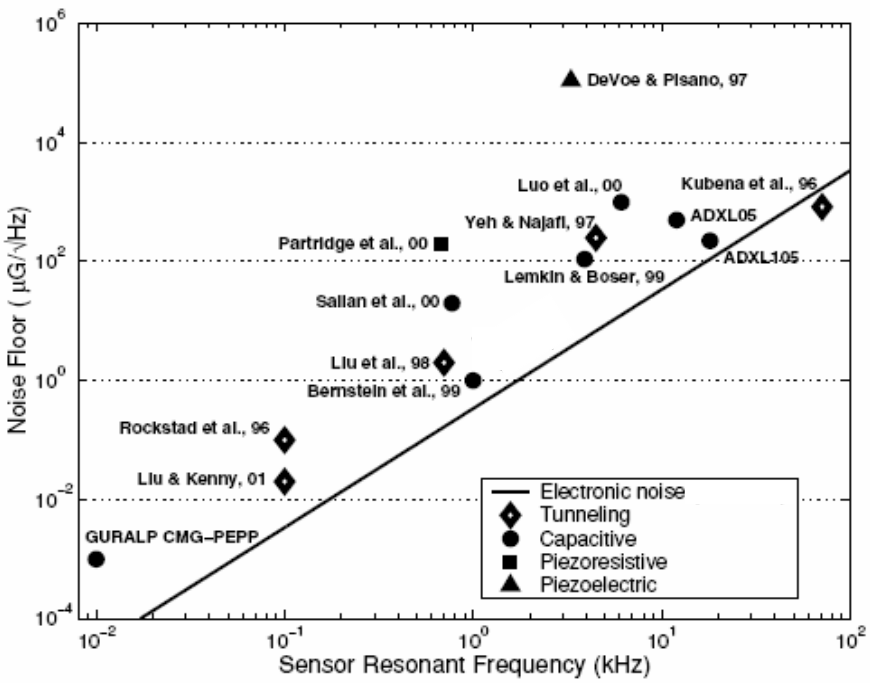


**Figure 2-3: Comparison of noise floors for different types of accelerometer systems**

The transducer is also responsible for noise. Brownian noise (section 2.3.4) is usually the dominant source.

Figure 2-4 shows the displacement resolution of several accelerometers to factor out the transducers performances. From the graph we can conclude that achieved displacement

resolution is worse in high precision accelerometers that use larger proof masses than those that use smaller masses, indicating that the performance of the high precision accelerometers is fundamentally limited by Brownian motion noise.

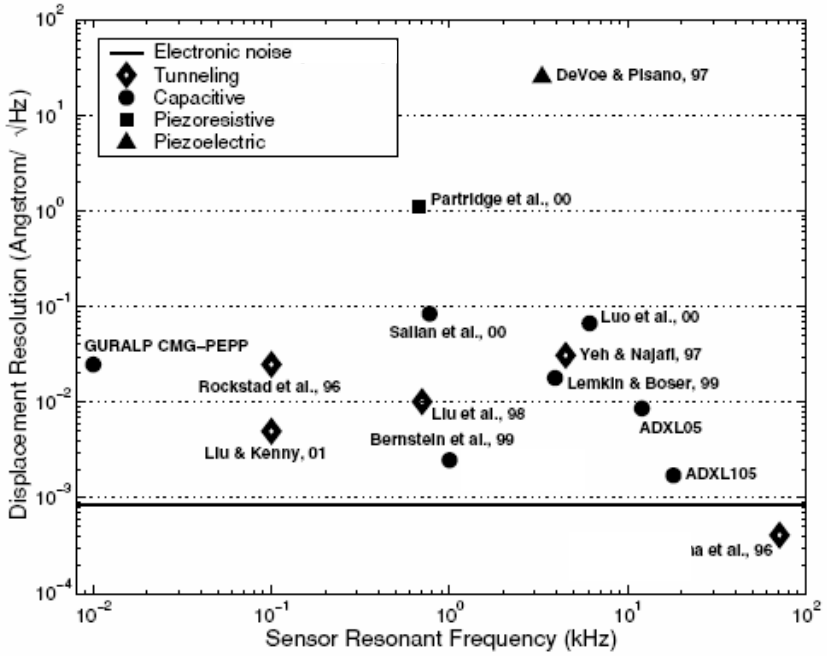


**Figure 2-4: Comparison of displacement resolution for different types of read-out systems**

### 2.3.2. Movement sensing

Accelerometers have different movement sensing strategy; each of them has strong and weak points. The following section will briefly describe the most used methods for movement sensing.

*Piezoresistive*

The beams that compose the mass-spring system can be equipped with piezo-resistive elements on them. The piezo-resistors will elongate or shorten as the beams are bended. This results in a change of the resistance which can be measured. This method is simple in both fabrication and read-out circuitry, but not very sensitive. Due to high temperature dependency of the resistors, drift (change of performance with temperature) is also an issue. [15], [16]

*Capacitive*

The proof masses and the frame are both connected to electrically conducting plates separated by narrow gaps, forming parallel plate capacitors. The capacitors are created by interlocking fingers, where one half of the finger is connected to the proof mass and the other half is connected with the frame. As the proof mass moves, the capacitance between the two half of the fingers, changes. This is at the moment the most used movement sensing method for accelerometers. Capacitive sensors have good DC response and noise performance, low drift, low temperature sensitivity, low power-dissipation. The main drawback is represented by the

susceptibility to electromagnetic interference (EMI). The issue can be addressed by proper packing and shielding of the accelerometer and electronics. [15], [16]

*Electron tunnelling*

When a tunnelling current is setup between the proof mass and the support frame, the deflection of the proof mass can be obtained by measuring the tunnelling current. This current is exponentially dependent on the distance between the tunnelling tip and substrate. This method allows for very high sensitivity to displacement but it shows a larger low-frequency noise level. Moreover, the read-out uses a sharp tip. Difficulty in manufacturing and positioning of the tip makes this method very challenging to realize. [15], [16]

*Other*

Together with the previous methods, optical, resonance and thermal are used methods, although less diffuse and of less interest for our purpose. [15], [16]

### 2.3.3. Gravity-Gradiometer designs

Together with the simple accelerometer design, some specific designs for Gravity Gradiometry have been proposed:

*Superconductive gravity gradiometry*

The read out of a superconductive gravity gradiometer is based on the Meisner effect. The Meisner effect states that no magnetic flux can penetrate a superconductor.

This effect used in a detection loop (
Figure 2-5) has two consequences: first, no magnetic flux can enter or leave a closed loop of superconducting material. Secondly, a magnetic piece of material will repel the flux and thus, influencing the self inductance $L$ of the nearby coil. This makes the value of $L$ dependent on the distance variation $x$. This value can be measured using the formula:

$$\varphi = I(x)L(x) = const. \tag{2.32}$$

This shows that the current $I(x)$ is related to the distance variation $x$. [17]

Two examples of Superconductive gravity gradiometer is represented by the instruments developed for the European STEP and GEM missions. The expected sensitivity of the first devise is $3x10^{-5}$ $E/\sqrt{Hz}$ above $10^{-3}$ $Hz$, while the latter instrument will have a sensitivity of $4x10^{-4}$ $E/\sqrt{Hz}$ above $3x10^{-3}$ $Hz$ ($1E=10^{-9}s^{-2}$). [22]

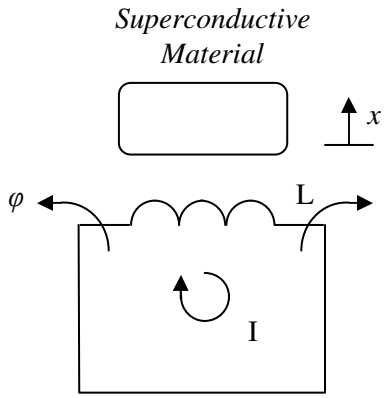


**Figure 2-5: Scheme of superconducting read-out (ref: [17])**

*Laser cooling systems*

Atom interferometry is a very promising technology for space instrumentation. A gravity gradiometer would consist of two atom-interferometers accelerometers separated by a baseline. The two acceleration measurements are performed simultaneously using the same Raman laser beam, so the common mode noise and uncertainties are cancelled.

The limitation in size of the instrument will be mainly determined by the baseline. Vacuum chambers for the atom clouds could be of the order of 10 cm in diameter.

These systems can reach, however, a sensitivity level of $3x10^{-4}$ E/√Hz. [18], [19], [24]

*MEMS based systems*

A gradiometer using MEMS (Micro Electro-Mechanical System) would have several advantages: high fabrication accuracy, allowing very symmetrical structures and low off-axis sensitivity.

Moreover, cooling down the proof mass and suspension structures offer the possibility of further reduction of the noise floor.

This solution has been chosen for realization of the micro gravity gradiometer, subject of this thesis, so it will be further treated in the next chapter. [18]

### 2.3.4. Noises and major errors in gravity-gradient measurement

A Gravity gradiometer is subject to a series of noise and error sources. This section will briefly enumerate the most common and important sources.

*Brownian Noise*

The Brownian motion noise is defined as the result of the thermal motion noise of the test masses. It is given by the equation [20]:

$$S_{\Gamma}(f) = \frac{8}{m\ell^2}\left(\frac{k_b T 2\pi f_0}{Q(f)}\right) \tag{2.33}$$

where $k_B$ is the Boltzmann constant [$m^2kgs^{-2}K^{-1}$]; $m$ is the mass of the proof mass [$kg$] , $\ell$ is the baseline [$m$], $T$ is the temperature [$K$], $f_0$ is the resonance frequency [*rad/sec*], and $Q(f)$ is the quality factor of the system (see section 3.2).

*Alignment*

Gravity Gradiometers are usually operated in a dynamically noisy environment to detect very weak differential signals. Passive vibration isolation is not possible because the signal frequencies of the gradiometer are very low in general (few *Hz*). Active isolation (feedback systems) can be applied to the angular degrees of freedom. It is difficult to achieve active isolation in all six degrees of freedom. Therefore, it is important to build into the device as high common-mode-rejection ratios as possible.

To adequately cancel acceleration along the sensitive axis, the sensitivities of the component accelerometers must be precisely matched. This requires either continuous calibration or extremely precise scale factors. However, even if perfect rejection of the axial component of acceleration would be achieved, the gradiometer would still be sensitive to the transverse component of the acceleration through imperfect alignment of the sensitive axes. In an in-line component gradiometer, linear and angular accelerations of the platform, $\bar{a}$ and $\bar{\alpha}$, generate differential motion of the test masses through departure from parallelism, $\delta\hat{n}$, and concentricity, $\delta\hat{\ell}$, of the sensitive axes of the component accelerometers:

$$\delta\Gamma_a = \frac{1}{\ell}\delta\hat{n}\cdot\bar{a} \tag{2.34}$$

$$\delta\Gamma_\alpha = \left(\delta\hat{\ell}\times\hat{n}\right)\cdot\bar{\alpha} \tag{2.35}$$

Where $\ell$ is the baseline; $\hat{\ell}$ and $\hat{n}$ are the unit vectors along the baseline and the direction of the gradiometer sensitive axis, respectively.

Another important error source for a gradiometer is the centrifugal acceleration of the platform. The high frequency angular velocity noise must be attenuated by applying passive vibration isolation or the platform must be stabilized against the angular motion noise at all the frequencies. [20], [21]

*Linear and angular acceleration errors*

The linear and angular acceleration of the spacecraft, $\ddot{x}$ and $\ddot{\omega}$, couple to the gradiometer by:

$$\delta\Gamma_{\ddot{x}} = \frac{1}{\ell}\left(\hat{n}\delta h + \delta\hat{n}\right)\cdot\ddot{x} \tag{2.36}$$

$$\delta\Gamma_{\ddot{\omega}} = \left(\delta\ell\times\hat{n}\right)\cdot\ddot{\omega} \tag{2.37}$$

where $\delta h$ is the mismatch of the scale factors, and $\delta \hat{n}$ and $\delta \hat{\ell}$ represent the misalignment of the sensitive axes from parallelism and concentricity, respectively. [22]

*Attitude rate error*

On a platform rotating with an instantaneous angular velocity $\dot{\omega} = \dot{\omega}_0 + \delta\dot{\omega}$, a gradiometer measures:

$$\Gamma' = \Gamma + \left[ \dot{\omega} \cdot \dot{\omega} - \left( \dot{\omega} \cdot \hat{n} \right) \left( \dot{\omega} \cdot \hat{n} \right) \right] \tag{2.38}$$

The centrifugal acceleration error can be made a second-order error in $\delta\dot{\omega}$ by choosing an inertial orientation of the spacecraft $\left( \dot{\omega}_0 = 0 \right)$. [22]

*Self-gravity errors*

Gravity Gradiometers are very sensitive to time-varying signals due to change in mass or movement of masses on a spacecraft (such as carburant movements in tanks) or thermal distortion of the spacecraft. [22]

*Test-mass charging*

The test masses could be charged by cosmic rays. The charge can disturb accelerometers in three ways [22]:

1. by applying electrostatic forces through asymmetries in the accelerometers
2. by directly transferring momentum
3. through heating

# 3. MEMS based Gravity Gradiometer

## *3.1. MEMS Based micro-gradiometer design*

An innovative approach to gradiometry is represented by the use of MEMS (Micro Electro-Mechanical Systems). This technique allows the creation of very small mechanical structures on silicon wafers. A structure that can work as a gradiometer would be composed by two masses etched in a silicon wafer, attached to the wafer by means of springs. Those simple mass-spring systems alone will act each as an accelerometer, and together as a gradiometer. The design presented in this work has the goal to demonstrate that this kind of system can actually work and it will be the basis for future development of the instrument.

In fact, the masses of the proposed design are not heavy enough to match the required values of accuracy for planetary research missions (see section 2.2). In order to reach these values other masses should be attached to the structure, as will be discussed in the next section.

Moreover, this design does not include electronic read-out. The proposed read-out for this sensor is a capacitive superconductive comb structure. It will be integrated in the structure as soon as the mechanical properties will be measured and the working principle demonstrated. For sake of completeness, the read-out, however, will be briefly described in this chapter.

### 3.1.1. Layout of the wafer

The proposed layout is based on research performed at Twente by R. Cuperus [17] on the optimal shape and dimensions of the different elements present in the gradiometer [38]. The overall aspect of the gradiometer is shown in Figure 3-2 and Figure 3-3 (in those figures, the real dimensions are not respected, in order to make the drawings more clear). At a first glance, the gradiometer is composed by two test masses (trapezoids in the figures) etched from the silicon wafer, attached to the wafer by means of eight beams. Those beams behave like springs, so, from now on they will be referred as and treated as springs.

The noise due to Brownian motion is, recalling equation 2.41:

$$S_\Gamma = \Gamma^2 = \frac{8}{m\ell^2}\left(\frac{k_b T 2\pi f_0}{Q(f)}\right) \tag{3.1}$$

Equation (3.1) gives the guidelines for the design of the structure: in order to have a small Brownian noise (that is the dominant noise source for this kind of instruments) we need to have a structure with a low resonance frequency and high quality factor, that represents the ratio between the input displacement and the output displacement at resonance frequency and, hence, it is related to the energy dissipation in the system. This kind of design will make the structure quite challenging to test as will be explained in details in section 4.

Typical values for MEMS are: $Q=10^5$, at T=77 K (temperature reachable with a reasonably small cooler).

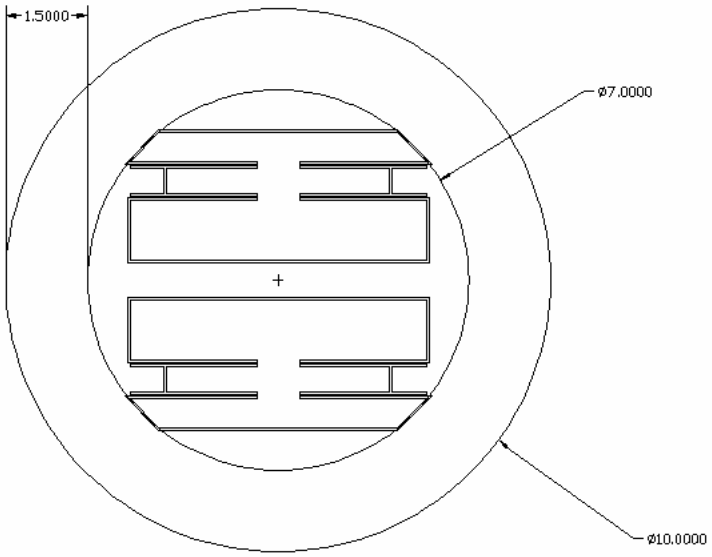


**Figure 3-1: Layout of the micro-gradiometer; the 1.5 cm ring on the external part will be left clean (without structures) as required by the processing technique**

**Figure 3-2: Micro-gradiometer: layout, front view**

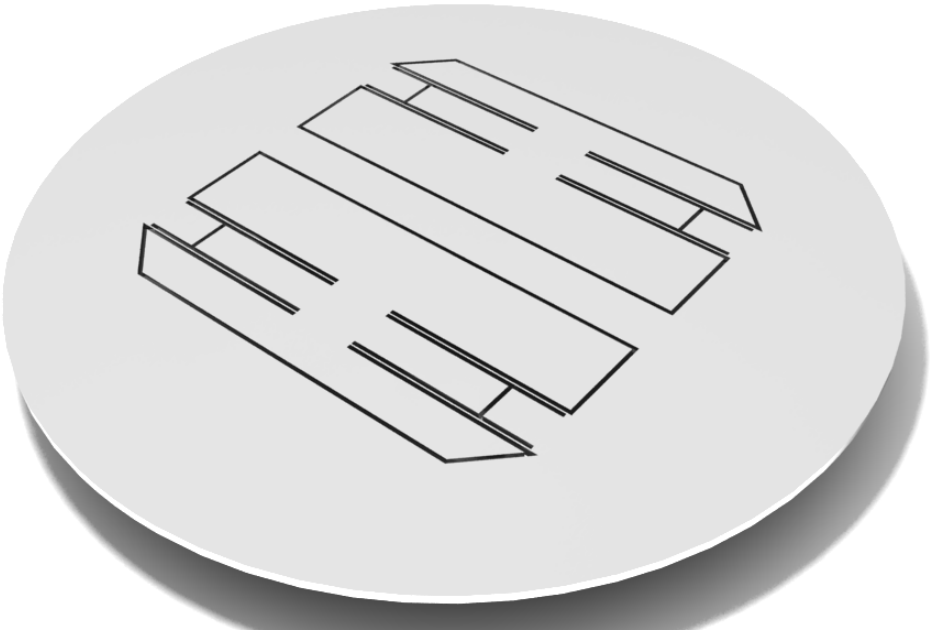

**Figure 3-3: Micro-gradiometer: layout**

### 3.1.2. Test Masses

The test masses are shown in Figure 3-4. They are basically two trapezoids, which dimensions are: Major base: *5.44 cm*; Minor base: *4.38 cm*; height: *2.34 cm*; straight side: *1.81 cm*. The masses are attached to the frame my means of 4 springs (white in the figure), two per side, in order to avoid tilting in the masses. One ring of *1.5 cm* in diameter need to be left clean (without structure) as required by the fabrication process.

The mass of each proof mass is approximately *1.34 g*. This is not sufficient to reach the required level of accuracy in terms of gravity gradient (*Eötvös*) this is the reason why the final version of the instruments foresees additional masses to increase the signal. The proposed additional masses are four cubes of gold with dimensions *1x1x1.5 cm*$^3$. They will be attached on and underneath the test masses using a bonding technique. With this technique, two (very) flat surfaces are put together under vacuum and then they stick without using any glue or similar substances.

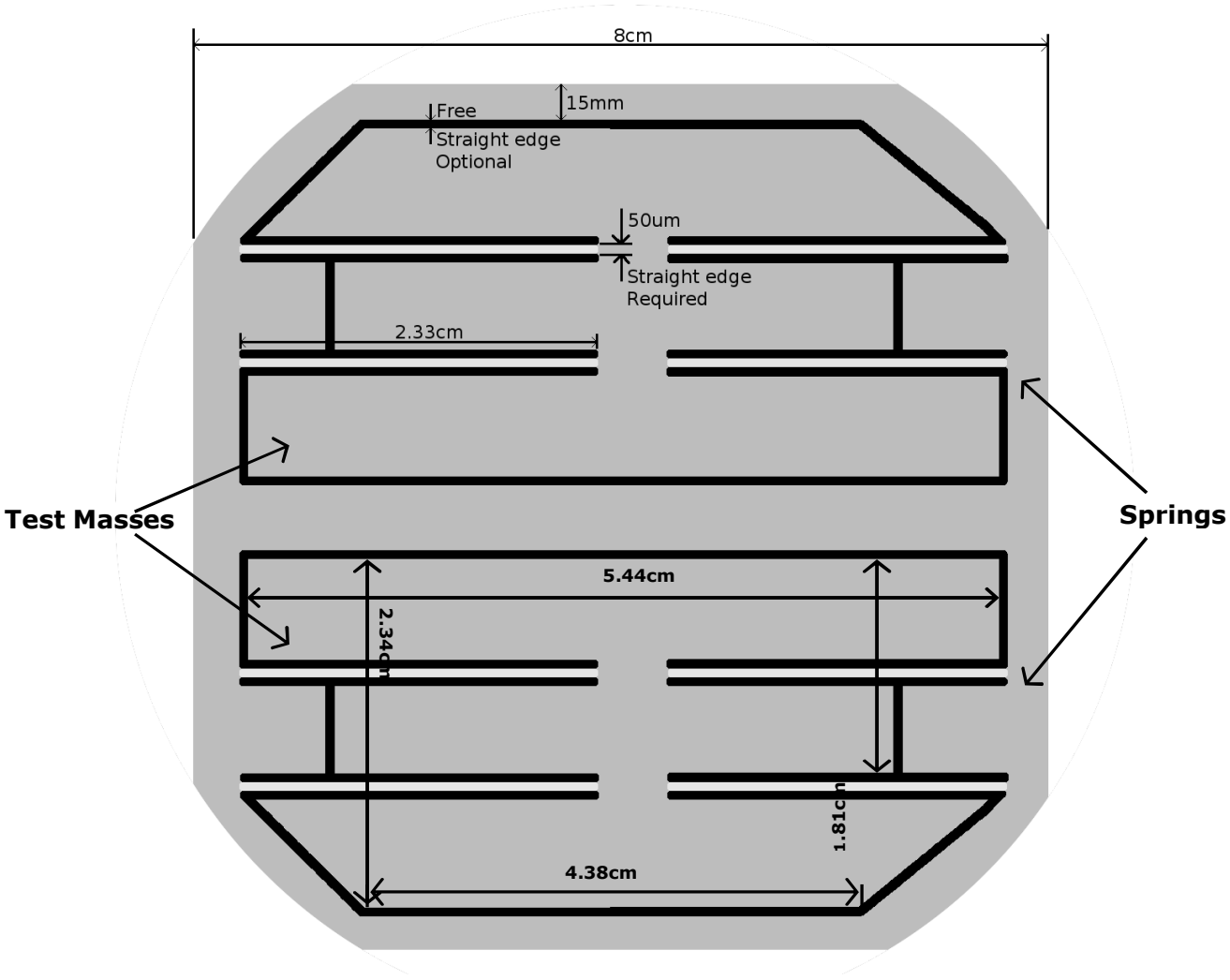


**Figure 3-4: Silicon wafer layout with cut sides. The silicon wafer will be cut on the side when it will be assembled in a instrument-like configuration**

In order to measure the spring constant ($k$) and the quality factor ($Q$) of the system (see section 3.2) the masses will be exited by an actuator and the movements will be recorder by a microscope and an imaging system (vibrometer, see section 4.3). In order to record an image and measure movement, the instruments need some reference points on the imaged surface. For this reason the masses will be furnished with marks in the interesting points (see Figure 3-5) in order to make possible the measurements, both absolute and relative.

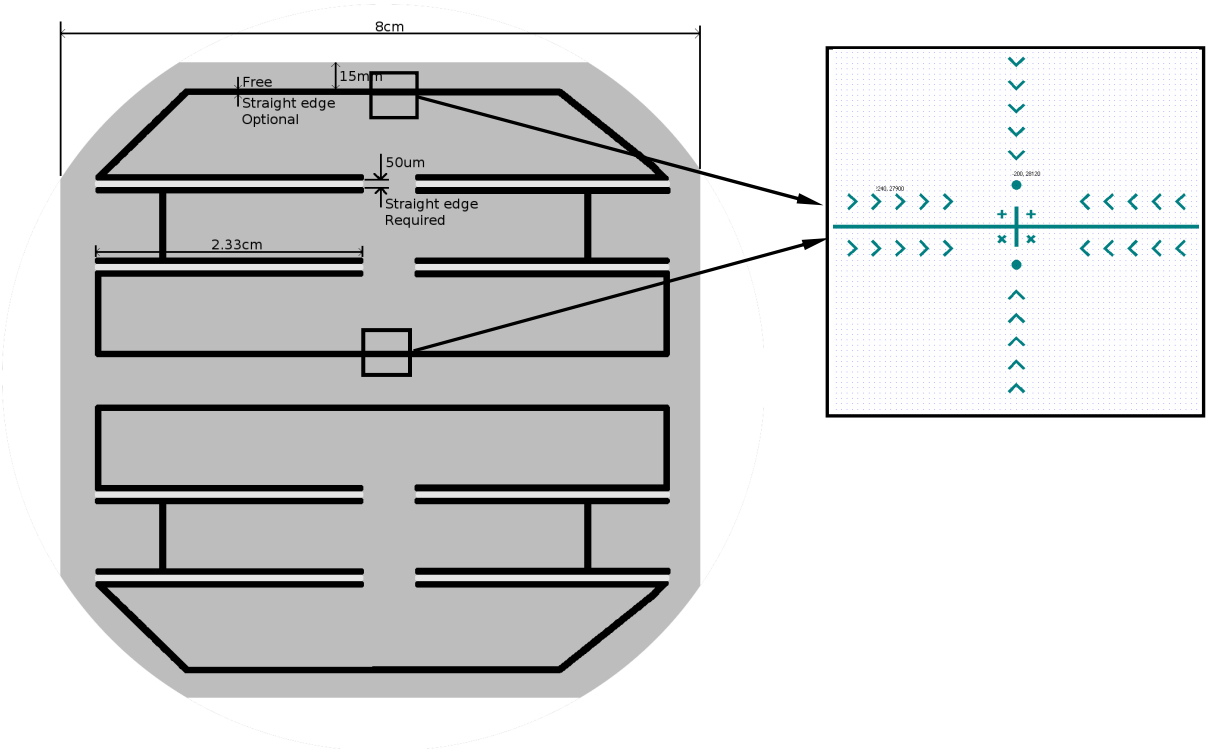


**Figure 3-5: Structures for optical read-out and their locations on the silicon wafer**

### 3.1.3. Springs

The masses are attached to the support by means of four springs. These springs can be modeled as rectangular clamped-clamped beams. The system can be analyzed as follows: two springs on the same side can be considered as parallel springs and their spring constants can be summed:

$$k = k_1 + k_2 \tag{3.2}$$

Moreover we can consider the springs from opposite sides as one spring, with length equal to the sum of the lengths of the springs and loaded in the centre with a mass equal to the test mass (see Figure 3-7), neglecting the masses of the springs themselves.

We can derive the spring constant in the following way [15]: the mass can be regarded as a point load; the mathematical description for such a load is the Dirac function:

$$\delta(x-a) \tag{3.3}$$

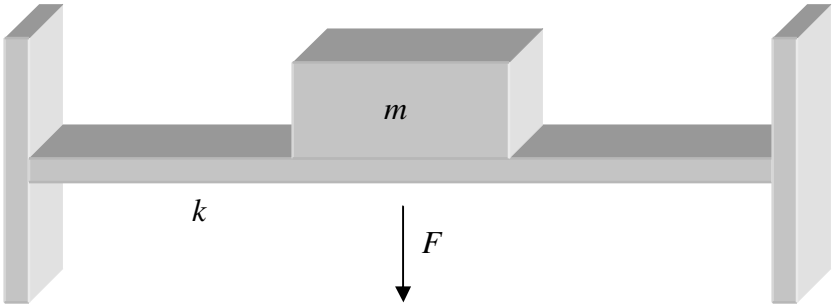


**Figure 3-6: Equivalent Spring System**

It is defined as zero value in the entire domain except at x=a. Moreover it has the property that its integral over the domain is equal to 1:

$$\int_{-\infty}^{\infty} \delta(x-a) = 1 \tag{3.4}$$

The differential equation we need to resolve is then:

$$EIw''' = F\delta(x-a) \tag{3.5}$$

Where $E$ is the Young Modulus [$N/m^2$], $I$ is the Momentum of Inertia [$m^4$], $w'''$ is the third derivative of the displacement (along $x$-axis) and $F$ is the force due to the mass $M$.

The integration of equation (3.5) along the length of the beam, recalling the property of the Dirac function expressed by equation (3.4), leads to:

$$EIw''' = F \tag{3.6}$$

The general solution of the differential equation, with the boundary condition (clamped-clamped ends, in this case) leads to:

$$w = \frac{F}{48EI} x^2 (3\ell - 4x) \tag{3.7}$$

Now we are able to calculate the spring constant of a clamped-clamped beam, since:

$$k = \frac{F}{w} \tag{3.8}$$

We have:

$$k = \frac{48EI}{x^2 (3\ell - 4x)} \tag{3.9}$$

The Young Modulus for Silicon is:

$$E_{silicon} = 150 \quad GPa = 150 \times 10^9 \quad N/m^2 \tag{3.10}$$

And the momentum of inertia, for a rectangular beam is:

$$I = \frac{b \cdot h^3}{12} \tag{3.11}$$

In our case we are interested in the *x* direction, so *b=500 μm*; *h=50 μm*; *l=2.33x2=6.44 cm* (see Figure 3-7). Using this values we obtain: *k=1.4823* [*N/m*].

Plugging this value and the value of the mass in equation for the resonance frequency (see section 3.2), we get:

$$\omega_n = \sqrt{\frac{k}{m}} = 33.2594 \quad [rad/s] = 5.2961 \quad [Hz] \tag{3.12}$$

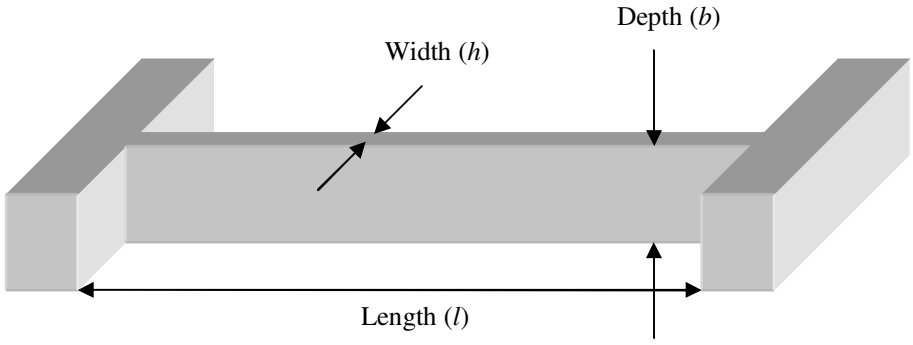


**Figure 3-7: Dimensions of the equivalent spring**

### 3.1.4. Air Damping

For the type of design proposed in this work, the damping is primarily due by the presence of air. This results from the air that may be trapped between the masses, the springs and the frame. Due to the small distance between those elements (50 *μm*, much smaller in case of the sense fingers of the capacitive read-out, see section 3.1.5) the air cannot move away from the gaps, causing damping.

The analysis about this phenomenon is based on linearized form of Reynolds equation. A formulation of the damping coefficient proposed by Zhang [25] for an isothermal air film, rectangular plates and small deviations from the nominal gap $d_0$ [*m*] is expressed by equation (3.13).

$$D = \frac{96}{\pi^4} \mu \frac{L^3 W^3}{L^2 + W^2} \frac{1}{d_0^3}, \quad \left[\frac{Ns}{m}\right] \tag{3.13}$$

$D$ represents the Damping Factor that will be defined in section 3.2, equation (3.18). The elements in equation (3.13) are: $\mu$: dynamic viscosity of the medium in the gaps [$Pa \cdot s = kgm^{-1}s^{-1}$]; $L$: length of the plate [$m$]; $W$: width of the plate [$m$].

Inserting the dimension of our system, we would have a value of the order of $10^{-3}$ $kg/s$ for the damping coefficient induced by the air presence. From here, we found the necessity to have a vacuum system.

This formulation expressed in equation (3.13), however, is only valid for pressure close to atmospheric pressure. Two basic approaches for considering air damping in rarefied air do exist. The first one is based on the concept of *effective coefficient of viscosity*, while the second one in based on the free molecular approach. [26]

According to the first approach, equation (3.13) remains the same, but the coefficient of viscosity should be replaced by an effective coefficient of viscosity, dependent on pressure through the Knudsen number ($Kn = \lambda / d$, where $\lambda$ is the mean free path of the molecules of the gas and $d$ is the gap distance).

Anyway, for $Kn >> 1$ the collisions among the molecules of the gas are so reduced that the gas can hardly be considered as a viscous fluid. In this case the gap became very small with respect to mean free path and a free molecular model needs to be considered. In our case:

$$\lambda \approx 10 \quad cm, \quad d = 50 \quad \mu m \rightarrow Kn = 2 \times 10^{3} \tag{3.14}$$

Christian proposed a free molecular model for damping in vacuum [27] where the interaction between gas molecules is neglected and the damping force on an oscillating plate is found by the momentum transfer rate from the vibrating plate to the gas molecules.

An approximation of the damping force is:

$$F_T \cong 4\sqrt{\frac{2}{\pi}}\sqrt{\frac{M_m}{RT}} PA\dot{x} \tag{3.15}$$

Where $M_m$ is the molar mass of the gas; $R$ is the universal molar gas constant ($R = 8.31$ [$J/mol/K$]); $P$ is the pressure; $A$ is the area of the plate; $\dot{x}$ is the velocity of the plate.

We can calculate the damping factor $D$, as:

$$D = F_T / \dot{x} \tag{3.16}$$

Inserting the values $M_m|_{air} = 28.97 \times 10^{-3}$ [$Kg/mol$], $R = 8.31$ [$J/mol/K$], $T = 293.15$ [$K$], $P = 10^{-3}$ [$mbar$] $= 10^{-1}$ [$Pa$], $A = 2.72 \times 10^{-5}$ [$m^2$], in equation (3.16), we obtain:

$$D \cong 3 \times 10^{-8} \quad \left[ Kg / s \right] \tag{3.17}$$

This value is one order of magnitude smaller than the damping due to the mass-spring system, calculated for the transfer function of the system (Figure 3-11), where $D \approx 4.5 \times 10^{-7}$.

Table 2 shows the classification of the different vacuum range. Our system will operate mostly between high and medium vacuum.

| ***Vacuum range*** | ***Pressure [mbar=hPa]*** |
|---|---|
| *Ambient pressure* | *1031* |
| *Low vacuum* | *300-1* |
| *Medium vacuum* | $1\text{-}10^{-3}$ |
| *High vacuum* | $10^{-3}\text{-}10^{-7}$ |
| *Ultra high vacuum* | $10^{-7}\text{-}10^{-12}$ |
| *Extremely high vacuum* | $<10^{-12}$ |
| *Outer space* | *100 μPa to 3 fPa* |

**Table 2: Vacuum Range classification (ref: [39])**

### 3.1.5. Gradiometer read-out

The foreseen read-out is a capacitive read-out. The system will use a full-custom mixed signal ASIC (Application Specific Integrated Circuit) currently under development at SRON in Utrech as part of the long term program for design, development, production and space-qualification of miniaturized high-performance sensor read-out and control electronics. This system will allow for an optimized system level design, a very high resolution (24 bit) ADC/DAC, a very low frequency measurement bandwidth ($10^{-4}\text{-}10$ *Hz*) and low power consumption, mass and volume. [7]

Figure 3-8 shows the read-out system and its position in the layout of the silicon wafer. The read-out is composed by couples of fingers. One finger is attached to the mass while the other finger is attached to the frame. The fingers are conductive (see Figure 3-9) and are connected to create a circuit. When a displacement occurs, the fingers approach of move away one another, changing the capacitance between them. This change in capacitance will be sensed by the ASIC and related to the displacement.

Figure 3-9 shows a vertical section of the read-out system. It is possible to see that the fingers occupy only the upper part of the wafer and not the entire depth. Moreover, it is possible to see how the fingers will be electrically connected in order to create a circuit.

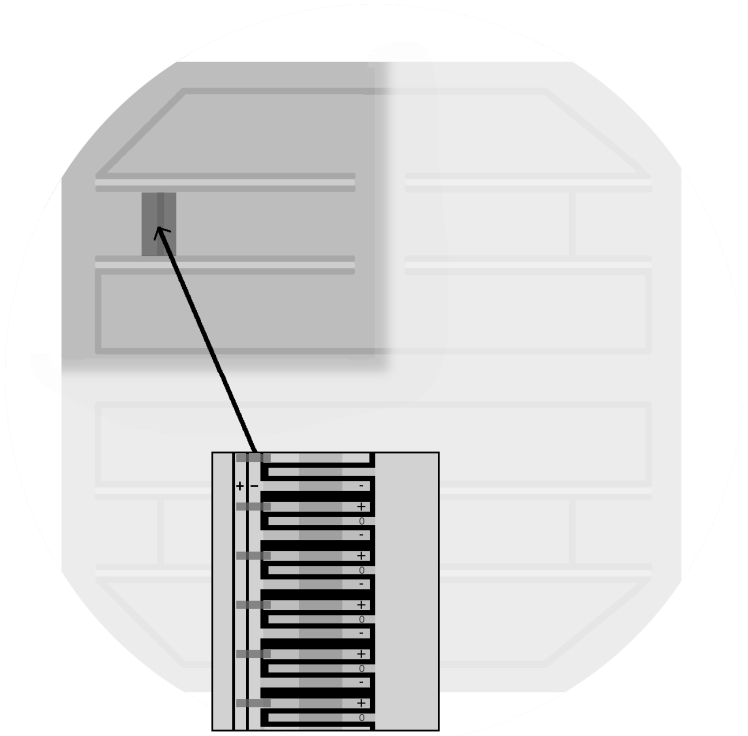

**Figure 3-8: Read-out fingers and their location in the layout of the silicon wafer.**

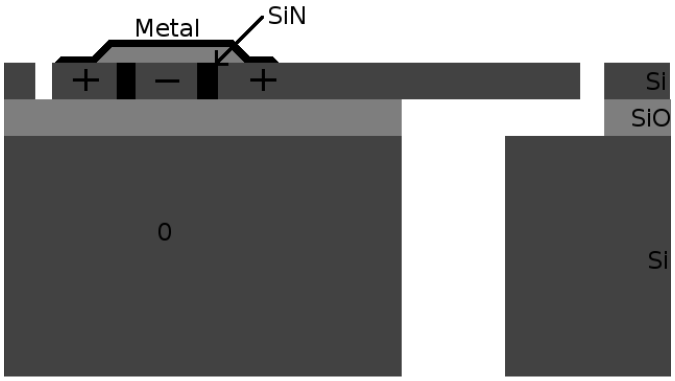


**Figure 3-9: Vertical section of the read-out system: the fingers occupy only the upper part of the wafer, not the entire depth. They are electrically connected in order to create a ciruit.**

## *3.2. Mass-spring-damping system characterization*

After having described the different components of the MEMS gradiometer, we need a mathematical description of the system, in order to characterize it and its behaviour. [28]

This mass-spring-damper system can be regarded as a single-input single-output (SISO) second order linear system.

The static behavior of the system can be described by:

$$\begin{cases} F = ma \\ x_{static} = \dfrac{F_k}{k} = \dfrac{ma}{k} \\ F_D = Dv \end{cases} \tag{3.18}$$

Where $F$ is the applied force, $m$ is the mass, $a$ is the acceleration, $k$ is the spring constant, $D$ is the damping factor, $v$ is the velocity.

The dynamic behavior is expressed by the equation:

$$m\ddot{y} + D\dot{y} + ky = F_{external} \tag{3.19}$$

Equation (3.19) can be written in another form:

$$\ddot{y} + 2\zeta\omega_n \dot{y} + \omega_n^2 y = \frac{1}{m} f(t) \tag{3.20}$$

This formulation can be helpful in the physical description of the phenomenon, since we introduce the parameter $\zeta$ or *Damping Ratio*, defined as the amount of damping in the system, and $\omega_n$, *Natural (or Resonance) Frequency*, defined as the frequency of oscillation in an idealized system with zero damping or in a system that does not dissipate energy (since the damping is related to the rate of dissipation of the energy in the system).

Comparing equations (3.19) and (3.20) we can find the following relations:

$$\omega_n = \sqrt{\frac{k}{m}} \quad \left[\frac{rad}{s}\right] \tag{3.21}$$

$$\zeta = \frac{D}{2\sqrt{km}} = \frac{D}{2m\omega_n} \tag{3.22}$$

Moreover, we can define the Quality Factor as:

$$Q = \frac{1}{2\zeta} = \frac{m\omega_n}{D} \tag{3.23}$$

### 3.2.1. System transfer function

In dealing with a linear system, a significant body of theory has been developed for analyzing single-input single-out put system without having to go through the classical methods of solving the input-output differential equation for the system. This body of theory involves the use of the complex variable $s=\sigma+j\omega$, sometimes known as complex frequency variable.

Let's us consider again the mass-spring-damper system, the basic equations are shown in different form with respect the previous section:

$$m\dot{v} = F_m = F - F_k - F_D \tag{3.24}$$

Equation (3.24) can be expressed in the $s$ domain (where $s=\sigma+j\omega$ represents the complex variable):

$$msV(s) = F(s) - F_k(s) - F_D(s) \tag{3.25}$$

Equation (3.25) can be rearranged as:

$$V(s) = \frac{1}{ms}\left[F(s) - F_k(s) - F_D(s)\right] \tag{3.26}$$

Using the following transformations for the different parameters we can write:

1. Velocity of the mass: $v(t) = \dfrac{dx(t)}{dt} \rightarrow V = sX(s)$
2. Hooke's Law: $F_k(t) = k \cdot x(t) \rightarrow F_k(s) = kX(s)$
3. Damper Law: $F_D(t) = D \cdot v(t) \rightarrow F_D = DV(s) = DsX(s)$

$$V = \frac{1}{ms}\left(F - \frac{k}{s}V - DV\right) \tag{3.27}$$

The block diagram that describes the system is shown in Figure 3-10:

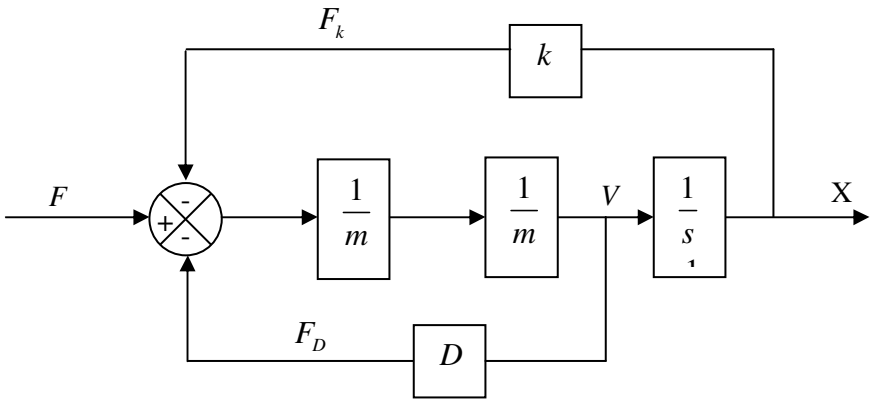


**Figure 3-10: Block Diagram of the Mass-Spring-Damper System**

Equation (3.27) can be further rearranged as:

$$V\left(1+\frac{k}{ms^2}+\frac{D}{ms}\right)=\frac{1}{ms}F \rightarrow V=\frac{sF}{ms^2+Ds+k} \tag{3.28}$$

And finally:

$$X=\frac{V}{s}=\frac{F}{ms^2+Ds+k} \tag{3.29}$$

For the overall transfer function the ratio between the output and the input, we have:

$$T(s)=\frac{X(s)}{F(s)}=\frac{1}{ms^2+Ds+k} \tag{3.30}$$

We can notice that the denominator in equation (3.30), when set to zero, is another form of the system characteristic equation (equation (3.19)):

$$ms^2+Ds+k=0 \tag{3.31}$$

The overall system transfer function contains all the information needed to predict the system response. In particular we can say that the amplitude of the steady sinusoidal response to a sinusoidal input of unit amplitude is the magnitude of the transfer function when $s=j\omega$, and the phase angle of the output sinusoid relative to the input sinusoid is the angle of the same transfer function.

The dynamic performances of a system are very often described by a Bode Diagram. This is a logarithmic chart that portrays the magnitude and phase characteristics, named after H. W. Bode.

Because the transfer function $T(j\omega)$ is complex, it may be expressed in complex exponential form as:

$$T(j\omega)=Te^{j\varphi_T} \tag{3.32}$$

where $T$ and $\phi_T$ are both function of the frequency and are expressed as:

$$\begin{aligned} T(\omega)&=\left|T(j\omega)\right| \\ \varphi_T&=\angle T(j\omega) \end{aligned} \tag{3.33}$$

or, using Cartesian coordinates, the transfer function may be expressed in terms of its real and imaginary parts:

$$T(j\omega)=\mathrm{Re}\left[T(j\omega)\right]+j\,\mathrm{Im}\left[T(j\omega)\right]=T\cos\varphi_T+jT\sin\varphi_T \tag{3.34}$$

With the Bode diagram, the magnitude $T(\omega)$ versus frequency $\omega$ and phase angle $\phi_T(\omega)$ versus frequency $\omega$ characteristics are drawn on separate plots that share a logarithmic frequency axis.

In the case of the second order system of equation (3.20) exited with a harmonic force we have [28]:

$$T(\omega) = \frac{1}{\sqrt{\left[1-(\omega/\omega_n)^2\right]^2 + 4\zeta^2(\omega/\omega_n)^2}} \tag{3.35}$$

$$\varphi_T(\omega) = -\tan^{-1}\frac{2\zeta(\omega/\omega_n)}{1-(\omega/\omega_n)^2} \tag{3.36}$$

Figure 3-11 shows the Bode plot for an idealized system that represents our accelerometer. The input parameters are: $m=1.34$ [$g$], $\omega_n=33.26$ [$rad/s$], $k=1.4823$ [$N/ms$], $Q=10^5$, $D=4.4568x10^{-7}$ [$Kg/s$].

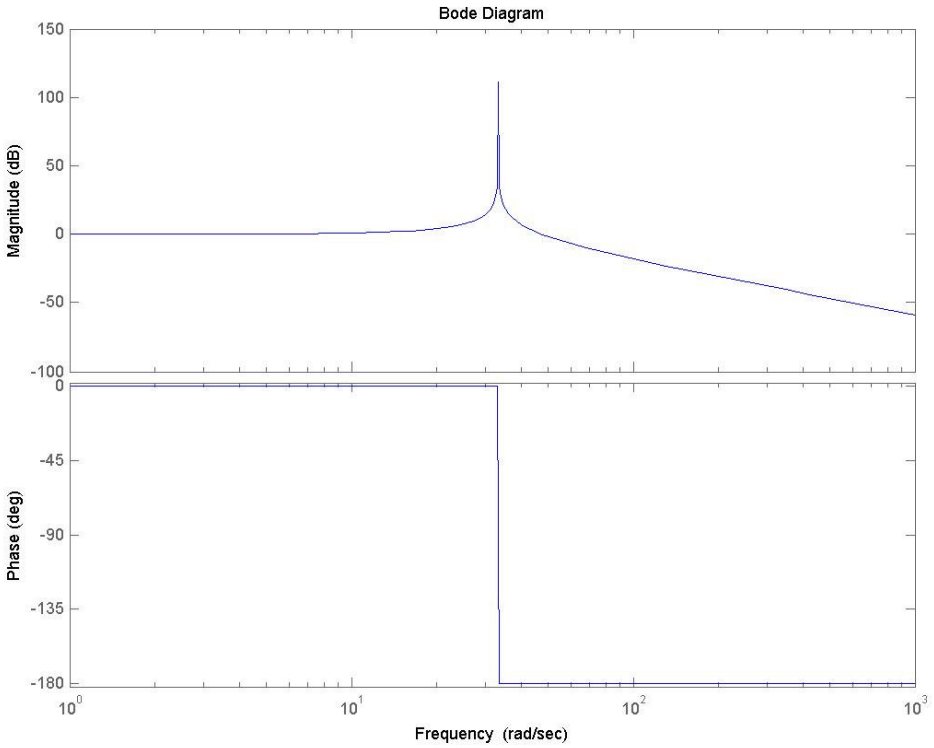


**Figure 3-11: Example of Bode diagram for a mass-spring-damping system with m=1.34 g, k=1.4823 N/ms, Q=$10^5$, D=4.4568x$10^{-7}$ Kg/s**

Once the Bode diagram has been plotted, it is possible to link the parameters present in it with the parameter we want to measure, and are needed for the characterization of the system as an accelerometer: spring constant, *k*, and quality factor, *Q*. In fact, using the following relations we can link *k* and *Q* with the natural frequency and the half of the *-3dB* bandwidth, $\sigma$; both parameter are easily measurable from a Bode diagram (Figure 3-11). [29]

We have:

$$k = m \cdot \omega_n^2 \tag{3.37}$$

And:

$$Q = \frac{\omega_n}{2\sigma} \tag{3.38}$$

Where:

$$\sigma = \zeta \cdot \omega_n \tag{3.39}$$

$2\sigma$ represents the frequency interval between two points on the amplitude resonance curve that are $1/\sqrt{2}=0.707$ of the maximum amplitude. [30]

### 3.2.2. Sampling frequency

Our purpose is to measure the frequency response of the mass-spring system excited with a harmonic signal. This process will be performed by means of a computer that will reconstruct a digital signal from an analog one. The choice of the sampling frequency for this kind of process is crucial.

A continued, band-limited signal of maximum frequency $\omega_{max}$ can be recovered by a sample signal if the sampling signal frequency $\omega_S$ is greater that twice the maximum signal band frequency:

$$\omega_S > 2\omega_{\max} \tag{3.40}$$

Or, if the T is the sampling period:

$$T < \pi / \omega_{\max} \tag{3.41}$$

Moreover, we define the *Nyquist Frequency* as:

$$\omega_N = \omega_S / 2 \tag{3.42}$$

A very common problem is represented by the *Aliasing* phenomenon. It is manifested by presence of harmonic components in the sample signal that are not present in the original, continuous signal.

The Frequency of aliasing harmonics is defined as:

$$\omega_a = \omega_S - \omega_c \tag{3.43}$$

Where $\omega_S$ is the sampling frequency and $\omega_C$ is the frequency of the continuous signal. [28]

## 3.3. Processing technique

The proposed processing technique is a DRIE (Deep Reactive Ion Etching) to be performed at MESA+ at Twente University.

According to simulation performed by Cuperus at UTwente, in order to remove the common-mode acceleration, the resonance frequencies of both accelerometers of the gradiometer need to be matched at *0.1%*. In order to keep the resonance frequency of the accelerometers under *0.1%* match, shapes of the springs need to be as much similar as possible.

The processing technique may produce two different types of errors:

- Errors along the length of the springs: even small errors in the production can lead to unacceptable differences in spring constants.
- Errors in shape (cross section): when the shape of the springs changes from rectangular to trapezoidal (see Figure 3-12), the working line of the spring force will move causing an effective moment in the mass-spring system, which is, of course, strongly unwanted.

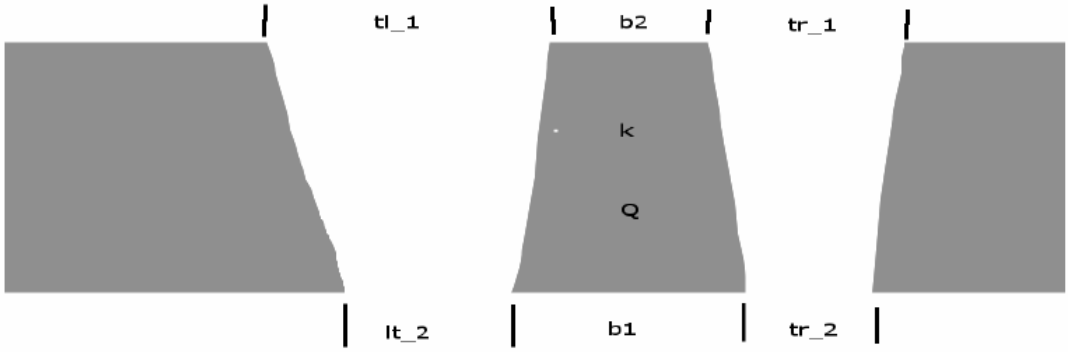


**Figure 3-12: Cross section of a spring with possible errors due to process technique. If the shape of the springs is not rectangular, the working point of the springs will shift, introducing a momentum in the system.**

The processing technique will be performed in the following steps:

1. Wet oxidation: a silicon dioxide layer will be created on both sides of the silicon wafer. On front side will be used a mask, on the back side a etch-stop
2. A photoresist layer will be posed on the front side of the wafer

3. The mask with the structure to be etched will be posed on the front side of the wafer
4. A dry etch with C4F8 will be performed in order to transfer the pattern to the silicon-oxide layer
5. The photoresist layer will be stripped away with oxygen plasma
6. The back side will be coated with polyimide in order to allow it to be lighted and baked
7. Cryogenic DRIE etch with SF6+CHF3 will be performed to etch trances through the silicon wafer. This is the most delicate step, since shapes of the springs is build up now
8. The polyimide layer on the backside is stripped away
9. The oxide layer on the back side is removed

# 4. Mechanical Test on a MEMS based Gravity-Gradiometer

In order to characterize the micro gravity-gradiometer, spring constant and quality factor need to be precisely measured. This kind of measurement is not an ordinary one and presents several difficulties. This is the reason why a dedicated test setup has been designed and realized.

The requirements for the test are:

- Vacuum: in order to decrease Brownian noise (see section 3), damping due to presence of air (see section 3.1.4) and recreate pressure conditions closer to space environment.
- In-plane actuation: we need to have the sensitive axis of the instrument perpendicular to the gravity acceleration, in this way the influence of the gravity on the measurement is minimized.
- Low frequencies actuation: the resonance frequency of the instrument is in the 1-10 Hz bandwidth
- Small displacement: the target is fraction of micrometer, since the system has a high quality factor and the gap between the masses and the frame is small as well ($50\ \mu m$)
- Capture imaging and analysing system, in order to measure displacements with high accuracy

The system realized to meet the requirements is composed by a vacuum chamber, an actuator and two support structures. The actuator and the structures, needed to support the actuator and the silicon wafer, will be housed in the vacuum chamber.

The imaging and processing system has been found in the MSA-400 Micro System Analyzer (or Vibrometer), present at the TST (Transducers Science and Technology) department at UTwente. The vacuum chamber and the structures have been dimensioned to fit under the lens of this instrument. The different components of the test setup will be described in the following sections.

## *4.1. Test Concept*

The test concept is explained in Figure 4-1. The general idea is to provide a mechanical excitation to the silicon wafer (sine excitation, in terms of frequency $f$ and amplitude $A$, or step excitation) by means of an actuator. The produced signal is controlled with a function generator and a computer.

The signal ($x_{in}$), than, is transmitted to the micro-gradiometer by the actuator ($x'_{in}$) and the displacement of the masses ($x_{out}$) is registered and analyzed by the vibrometer.

The vibrometer is able to register both $x'_{in}$ and $x_{out}$ signals by following two different points on the surface of the micro-gradiometer. One of the two points will be on the supporting frame while the other one will be on the moving mass. This feature allows both absolute and relative displacement measurement. In particular, the relative displacement measurement will

insulate the contribution of the actuator displacement from the displacement of the masses. In this way the software of the vibrometer can directly calculate the frequency response plot of the mass-spring system.

At this point, using fitting techniques (see section 5.5.2), the transfer function of the mass-spring system can be reconstructed and, from it, the $k$ and the $Q$ of the system can be calculated.

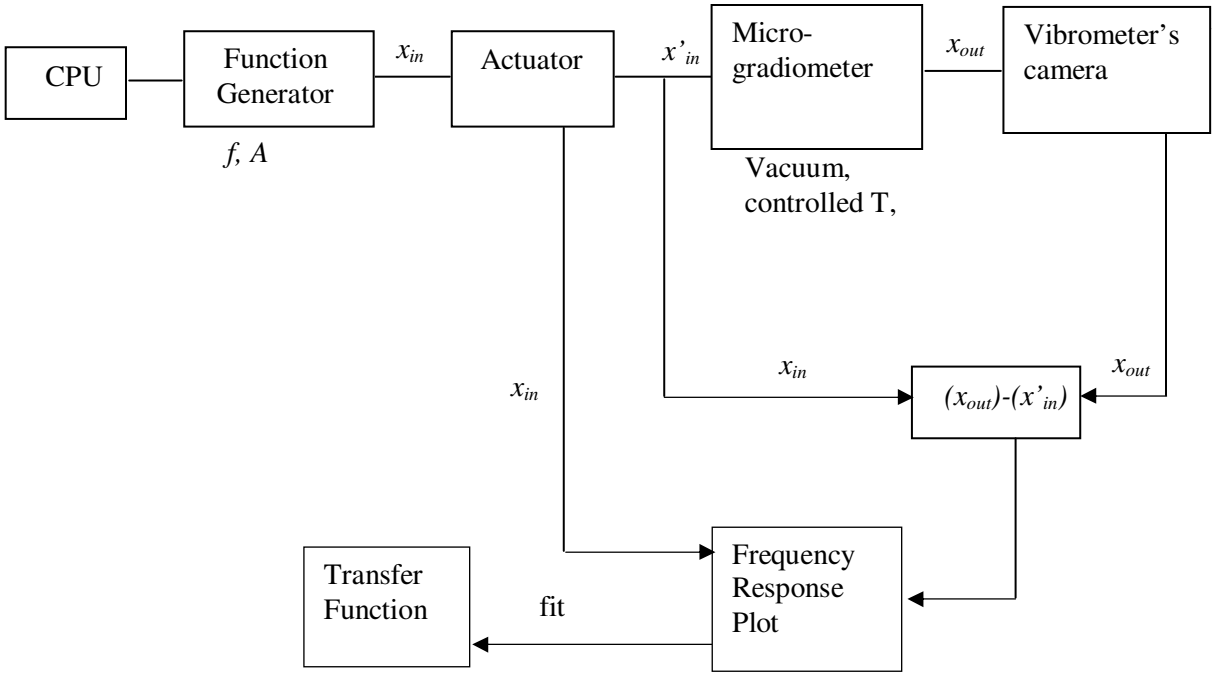


**Figure 4-1: Box Diagram of the Mechanical Test concept**

## 4.2. Test setup description

As already pointed out at the beginning of the chapter, the micro-gradiometer will be placed in a vacuum chamber. The movement will be provided by a piezo-actuator; this actuator will be attached to two structures in order to put it at the right focal length and to allow the silicon wafer to be attached to it. All the elements present in the test setup will be described in the following sections.

### 4.2.1. Actuator

The actuator used in this work is a one axis, low voltage, linear stage from Piezosystem Jena Company (model nanoX200 [31]). The main characteristics of the actuator are listed in Table 3. Figure 4-2 and Figure 4-3 show two views of the actuator. In Figure 4-3 the actuator is mounted on a support structure. Figure 4-4 shows the electronics apparatus together with the actuator. The electronics consists of a One-channel analog amplifier (30V300 model, [32]).

This actuator allows movement in in-plane direction with sufficient resolution (0.4 nm according to the specifications; this value, however, strongly depends on the electronics and the conditions of use of the actuator) with a reasonable price (about 5k €, electronics included). Moreover, it is vacuum compatible.

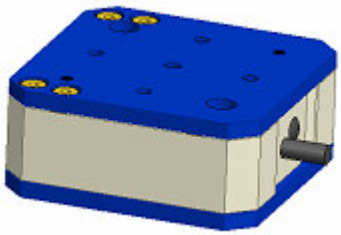

**Figure 4-2: NanoX 200 piezo-actuator (image: NanoX200 datasheet)**

| | |
|---|---|
| ***Stroke*** | *240 µm* |
| ***Resolution*** | *0.4 nm* |
| ***Electrical capacitance (+/-20%)*** | *5.2 µF* |
| ***Voltage range*** | *-10V…+150V* |
| ***Stiffness (+/- 10%)*** | *1.1 N/µm* |
| ***Max. load*** | *>100N* |
| ***Push/pull force capacity*** | *100/100 N* |
| ***Resonant frequency (+/- 20%):***<br>***no load***<br>***50 g***<br>***100 g***<br>***300 g*** | <br>*700 Hz*<br>*600 Hz*<br>*400 Hz*<br>*250 Hz* |
| ***Rotational error*: $\Theta_x$***<br>***$\Theta_y$***<br>***$\Theta_z$***<br><br>** typical values at -10…150V* | *5 µrad*<br>*5 µrad*<br>*5 µrad* |
| ***Dimensions (l x w x h)*** | *52x52x22 $mm^3$* |
| ***Temperature Range*** | *-20/80 ˚C* |
| ***Body Material*** | *Stainless steel/anodized aluminum* |
| ***Weight*** | *175 g* |

**Table 3: NanoX200 piezo-actuator characteristics (ref: [31])**

The functioning system of the actuator is based on piezoelectric effect. The actuator is equipped with four piezo-electric ceramic elements. Piezo-electric materials are used to convert electrical energy to mechanical energy and vice-versa.

Piezoelectricity is the property of all materials that have non-centrosymmetric crystal structure. It is found in inorganic material such as quartz ($SiO_2$) and lead zirconate titanate ($(Pb(Zr,Ti)O_3$ or PZT), in organic material and in some biological matter (hair, bones).

Piezo-electric materials are a class of low-symmetry materials that can be polarized by an applied electrical field and by an applied mechanical stress. [33]

The relation between the stress $\Pi_m$ [*N/m*] applied upon an elastic material and the resulting strain $x_m$ is given by the Hooke's law:

$$x_m = S_{mn}\Pi_n \tag{4.1}$$

Where $m,n=1,2,\ldots,6$ and $S_{mn}$ is the *Elastic Compliance*. The inverse relationship reads:

$$\Pi_m = c_{nm}x_n \tag{4.2}$$

Where $c_{nm}$ [*N/m*] is the Elastic Stiffness Tensor. The linear relationship between the applied stress $\Pi_m$ on a piezoelectric material and the resulting charge density $D_i$ is the so called *Direct Piezoelectric Effect*:

$$D_i = d_{im}\Pi_m \tag{4.3}$$

The values $d_{im}$ [*C/N*] are the Piezoelectric Coefficients. In general, $d$ is a 3$^{rd}$-rank tensor. On the other hand, piezo-electric materials change their dimensions when an electric field is applied:

$$x_m = d_{km}E_k = d^t_{mk}E_k \tag{4.4}$$

Equation (4.4) describes how the applied field is converted in strain within a piezo-electric. This effect is known as *Converse Piezoelectric Effect*; $d_{km}$ [*m/V*] are the converse piezoelectric coefficients of the *converse piezoelectric matrix*, while $d^t_{mk}$ are the coefficients of the transposed matrix. Typical values of the coefficients range from *2* to up to more than *2000 pm/V*.

Using thermodynamic considerations [34], it is possible to show that the piezoelectric coefficients $d$ for direct and converse piezoelectric effects are identical:

$$d_{direct} = d_{converse} \tag{4.5}$$

It is common to call the piezo-electric coefficient in the direction of the applied field, the *longitudinal coefficient*, and the one measured in the direction perpendicular to the field, the *transverse coefficient*. Other piezo-electric coefficients are called *shear coefficients*. All piezoelectric coefficients can be either positive or negative (it depends both by the material properties and by the direction considered).

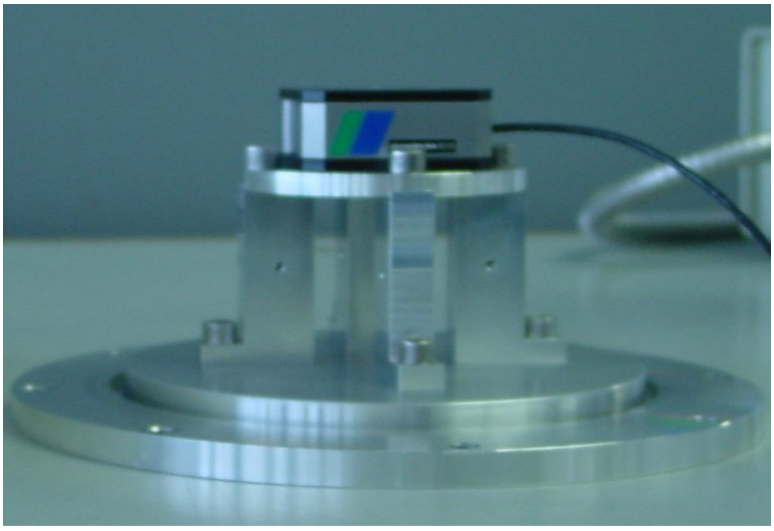

**Figure 4-3: Actuator on the support structure**

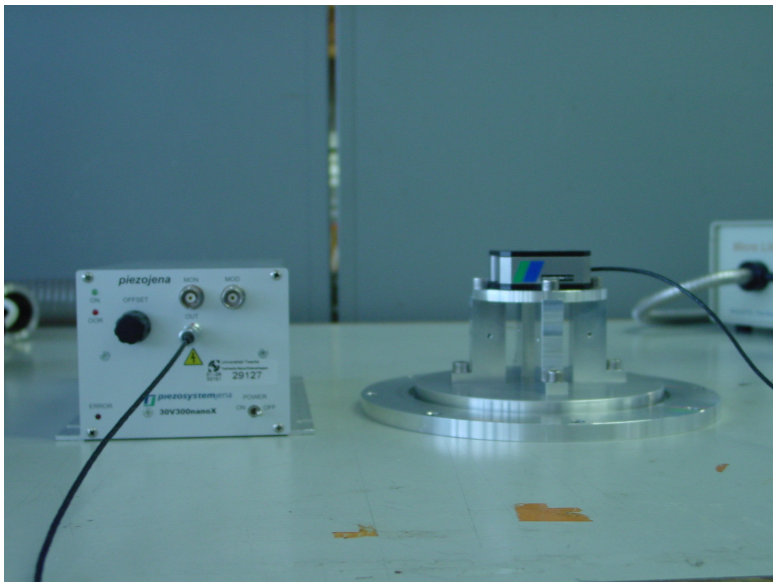


**Figure 4-4: Actuator with electronic apparatus (amplifier)**

### 4.2.2. Supporting Structures

The setup includes two supporting structures. They have been designed and realized to:

- Keep the actuator in the focus length of the lens of the vibrometer system. This structure is called *support plate*.
- Hold the silicon wafer suspended in horizontal position and transmits the movement from the actuator to the silicon wafer. This structure is called *wafer holder*. Two versions have been realized, a *3 mm* thick one and a *2 mm* thick one.

The two structures are sketched in Figure 4-5, Figure 4-7 and Figure 4-8, while in Figure 4-6 and Figure 4-9 the real aspect of the structure is shown.

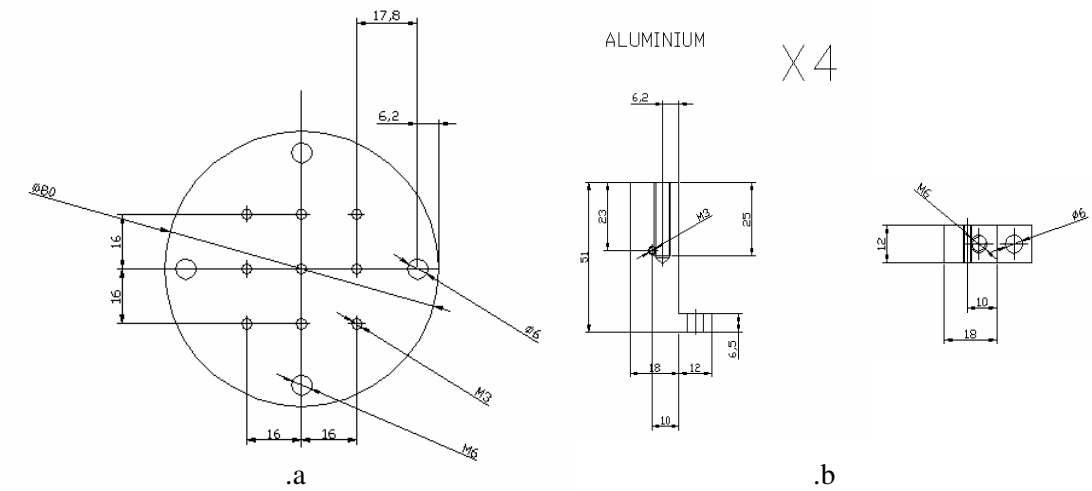


.a .b

**Figure 4-5: Support plate drawing, a. upper plate; b. legs**

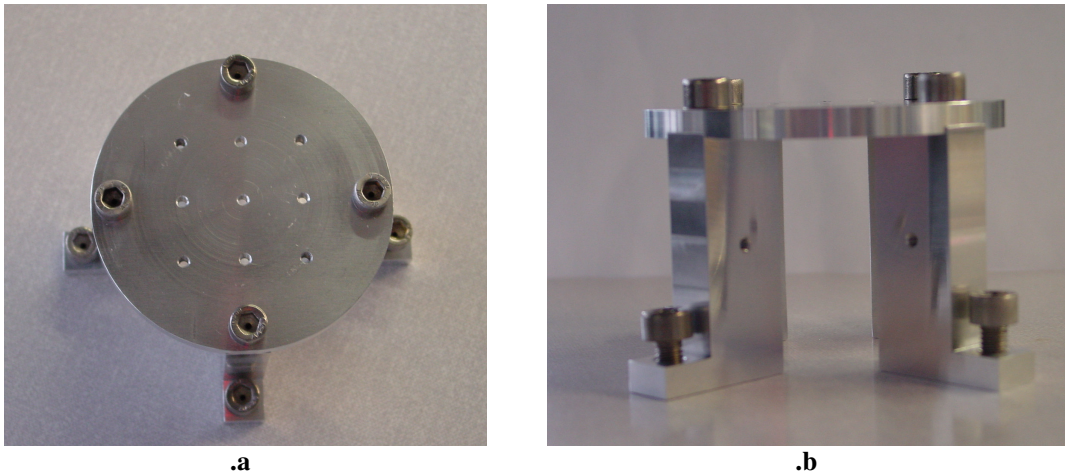

**.a** **.b**

**Figure 4-6: Support plate pictures, a. top view; b. side view**

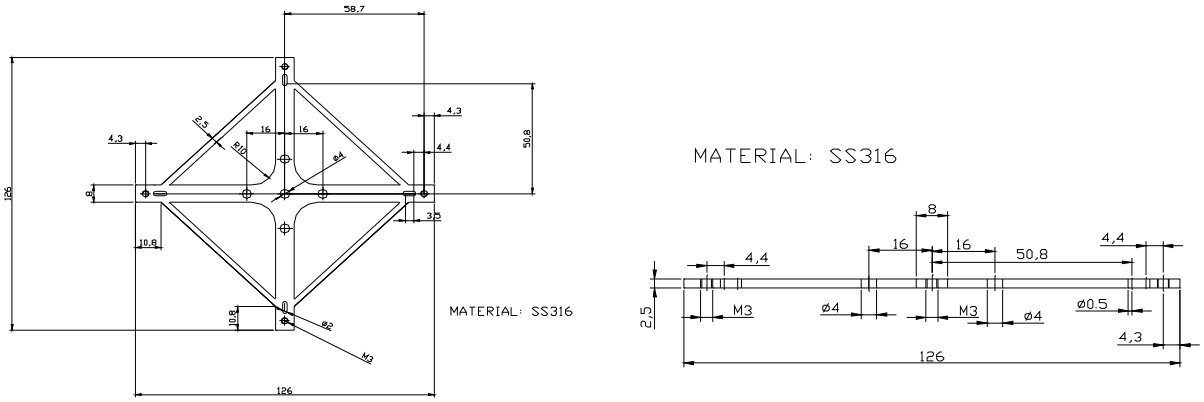


.a ;

**Figure 4-7: Wafer support drawings; .a: top view, .b: side view**

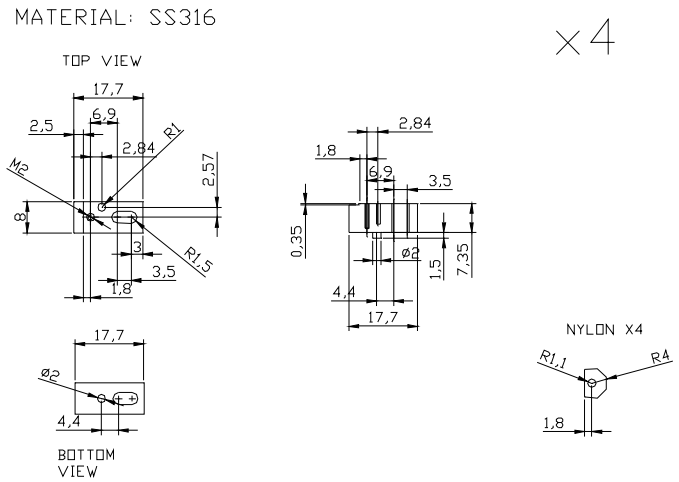


**Figure 4-8: Wafer support's components: holdings blocks**

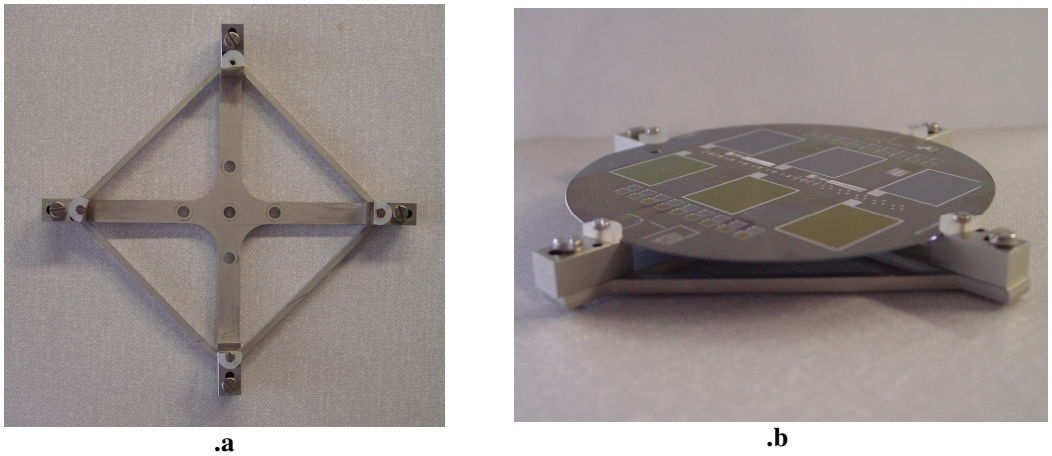

**.a** **.b**

**Figure 4-9: Wafer support pictures; .a: top view, .b: side view with a silicon wafer attached to the structure**

The whole assembly is shown in Figure 4-10 and Figure 4-11. Some considerations about the structures: they have been designed to have a high stiffness and resonance frequency far away form the bandwidth in which the setup is meant to operate (1-100 Hz).

This is the reason of the transversal metal connections between the arms of the wafer support. They will make the structure stiffer and avoid both vertical and horizontal oscillations of the arms.

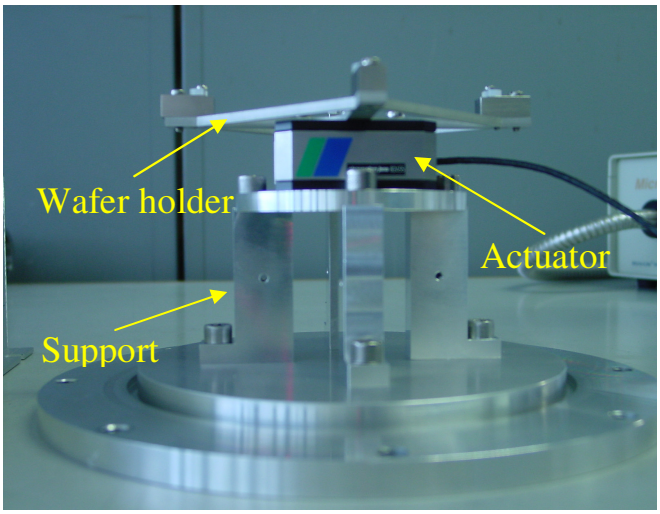


**Figure 4-10: Actuator with structures**

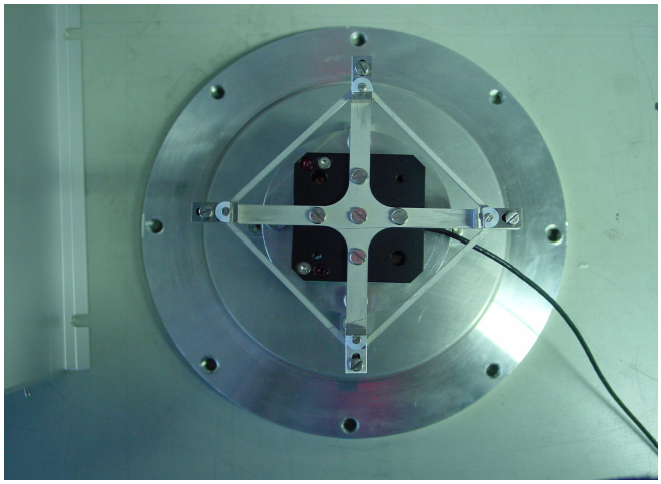

**Figure 4-11: Actuator with structures, upper view**

Simulations with finite elements method have performed on the two structures. Figure 4-12 shows the displacement of the support structure when excited with a horizontal force applied on the plate. In the picture the displacements are highly exaggerated. The lowest vibration mode frequency for this structure is close to 1465 Hz. Figure 4-13, on the other hand, shows the principal vibration mode for the wafer holder structure. As boundary conditions, the

central cross in the plate is held fixed. The lowest resonance frequency of this vibration mode for the wafer holder is around 600 Hz. We can conclude that both resonance frequencies are well above the useful bandwidth.

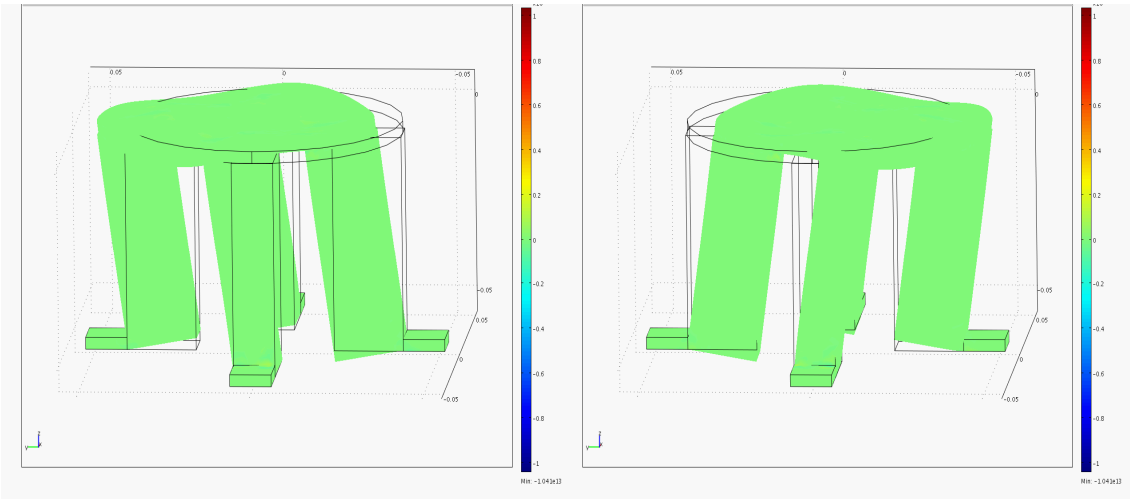

**Figure 4-12: Eigenmode frequency simulation for the support plate**

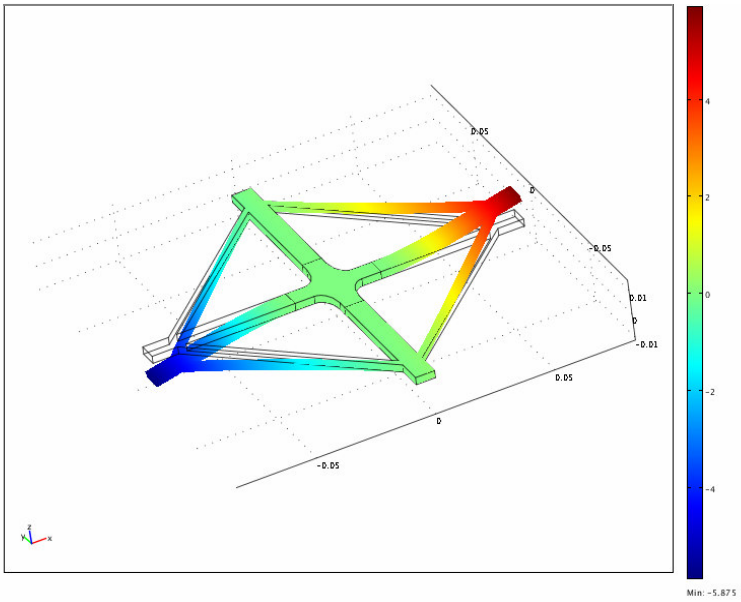


**Figure 4-13: Eigenmode frequency simulation for wafer holder**

### 4.2.3. Vacuum chamber

The actuator with all the structures will be housed inside a vacuum chamber. The chamber with all its components is shown in Figure 4-14, Figure 4-15, Figure 4-16 and Figure 4-17.

The chamber itself is a metallic cylinder (15 cm in diameter) with a glass window on the upper plate. The window has been tested and it does not interfere with the optical measurement. It does not introduce optical noise or disturbances. This has been verified by performing a random measurement without the glass and than with the glass between the lens and the object: the measurement was not affected by the presence of the glass.

The chamber is connected to a cross tube. The tube is connected to a pressure sensor, to a flange with electrical connector and a feed-through for a thermocouple and to a valve. Finally, the valve is connected to a vacuum turbo pump (Figure 4-16, Figure 4-17).

The electrical connector (Figure 4-17) is a 7 pins, vacuum compatible plug. Only 3 of the 7 available pins are used for alimentation of the actuator. This allow for future electrical connections that will be needed when the micro gravity-gradiometer will be equipped with the capacitive read-out. In this case, the read-out can be connected without modifying the structure of the setup.

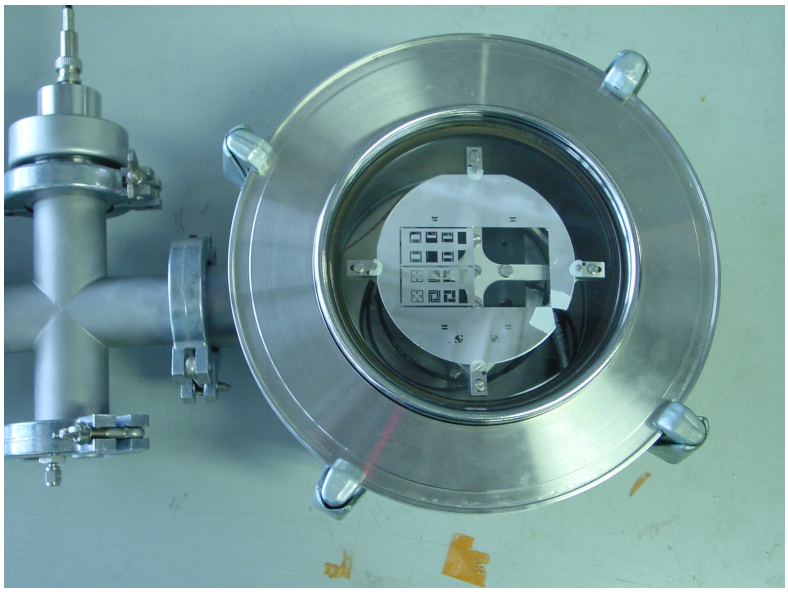

**Figure 4-14: Vacuum chamber with connections, upper view**

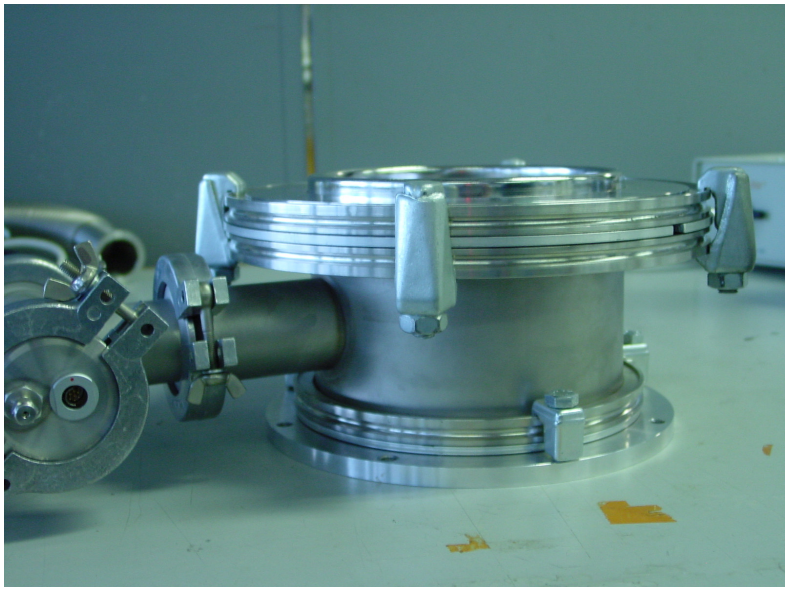

**Figure 4-15: Vacuum chamber with connections, side view**

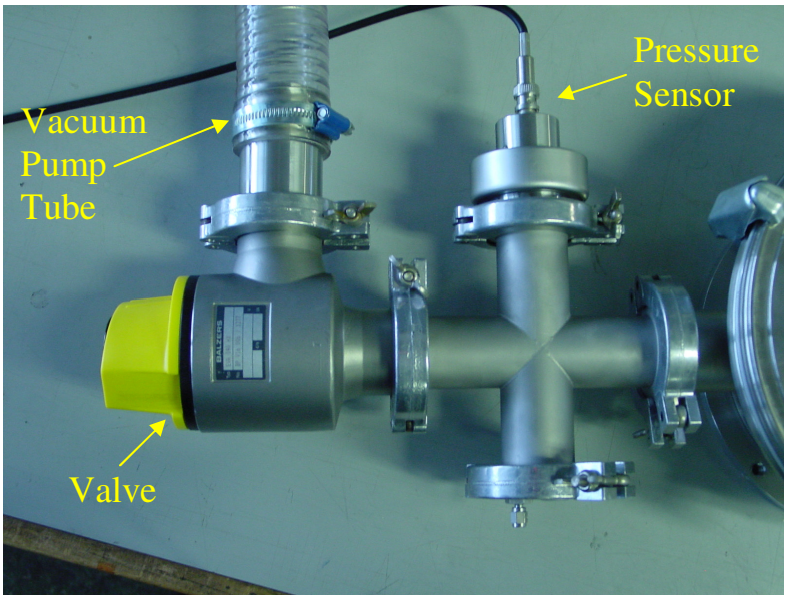


**Figure 4-16: Setup connections, top view**

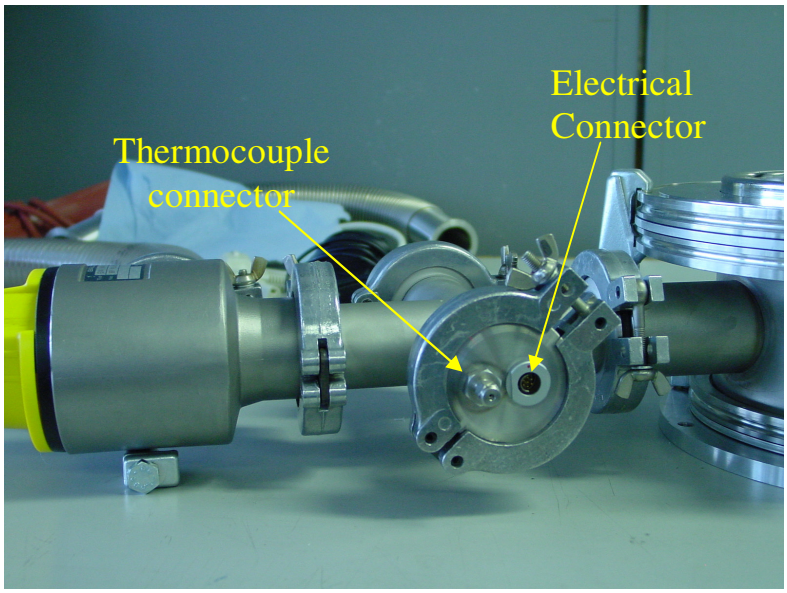


**Figure 4-17: Setup connections, side view**

### *4.3. Read-out System*

The selected read-out system is a MSA-400 Micro System Analyzer (Figure 4-18) [35]. This machine enables us to measure the displacement and phase of an object in horizontal direction.

This system is primarily designed for high frequency out-of-plane (vertical) measurements. In these conditions, its accuracy is extremely high. Our purpose is to perform measurement in low frequency, in-plane (horizontal) direction. It is still possible to perform such measurement, even if we have had encountered some difficulties. Those problems were related, above all, to the acquisition software (section 4.3.1) and to the fact that we had limited access to the machine, being it property of a different department. Despite those problems, this system is still the best choice (in terms of precision) for our measurements.

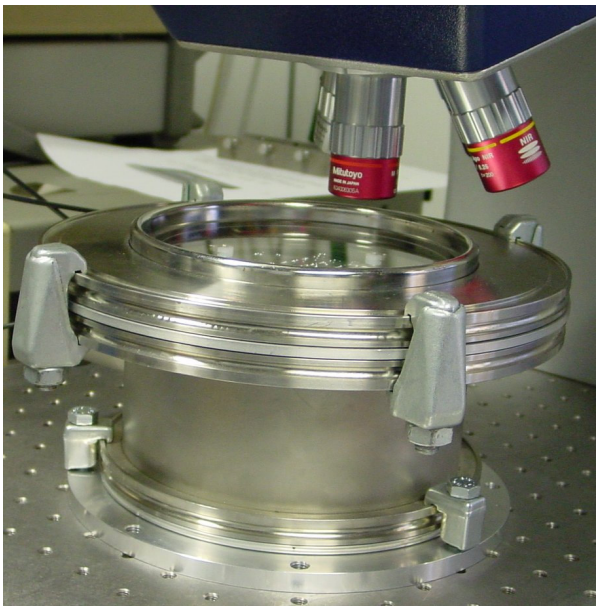


**Figure 4-18: Vacuum chamber under the lens of the Micro System Analyzer (Vibrometer)**

### 4.3.1. Image acquisition strategy

The system uses a stroboscopic illumination and digital imaging to record motion of moving objects in time and to capture their position. Short light pulses synchronized with the motion of the object capture the position at precise angle phase. By shifting the time of these pulses by phase angle increments, the motion of a moving object can be sampled and reconstructed.

The flash duration is adapted to the actual vibration frequency. The image quality is thus independent from the frame rate of the camera. The internal signal generator periodically excites the component with a sine or a pulse signal. A "pattern generator" uses a LED to generate ultra-short flashes of light (<80 ns) synchronously with the phase position of the excitation signal. A high level of phase accuracy is thus obtained. [35]

The electronic camera shutter is in turn synchronized with the excitation. It remains open until enough light at the same phase of the periodic motion has been collected (see Figure 4-19). [35]

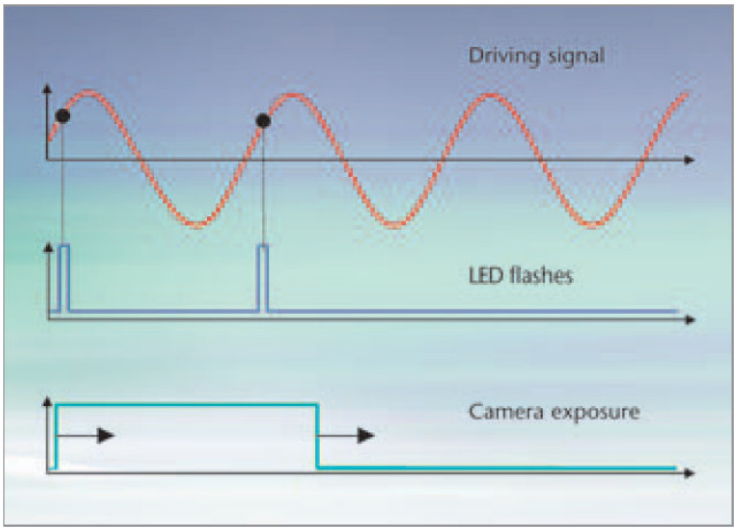


**Figure 4-19: Vibrometer's image acquisition strategy (Image: Polytec)**

This very image acquisition strategy, carries a series of drawbacks when operate in low frequency range, especially for a step response measurement. The image acquisition system is designed to acquire just one measurement every cycle (Figure 4-20). The maximum $\Delta t$ between two measurement can be *80 ns*. If the $\Delta t$ is larger than *1/25 Hz* (that is the sampling frequency of the camera), the cycle is skipped and the measurement is taken at a successive cycle. This is possible because the camera is synchronized with the ultra fast light flash.

Our system being very under damped, it will take several minutes (up to 10 minutes) to the vibration to decay, hence, a step measurement will become extremely long (up to few days).

This is mainly a software problem and it could be fixed. Any case, a step measurement performed in one cycle would have a maximum sampling rate of *25 Hz* that, in turns, means a Nyquist frequency (see section 3.2.2) of *12.5 Hz*. This is just enough for our measurements purpose.

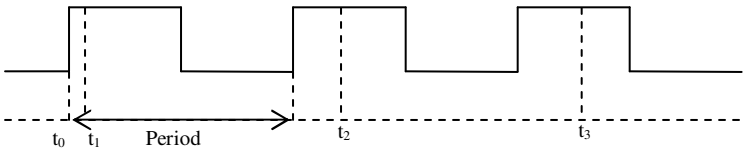


**Figure 4-20: Measurement strategy of the vibometer's software: only one measurement per period (or cycle) is recorded, the time difference between two measurement point can be 80 ns**

The best choice, however, will be to perform a frequency sweep measurement. This kind of measurement has fewer drawbacks but still needs to be performed very carefully. The key parameter is, in this case, the settling time: this is the time that the vibrometer left to the system to rest between two measurements at different frequencies. In order to have a clean measurement we would need to set a very high settling time (some minutes) but this, in turns, greatly increases the duration of the measurement itself.

Moreover, the possibility of perform differential measurements will allow to insulate the movement of the masses from the movement of the frame due to noise.

### 4.3.2. Pattern acquisition and recognize system

The movement of an object is reconstructed by means of a pattern acquisition and recognize system. The software can record an area of the image with clear features on it. The displacement is calculated by recognizing the same pattern on successive images and calculating the distance between the two patterns by comparing the images taken at different instants.

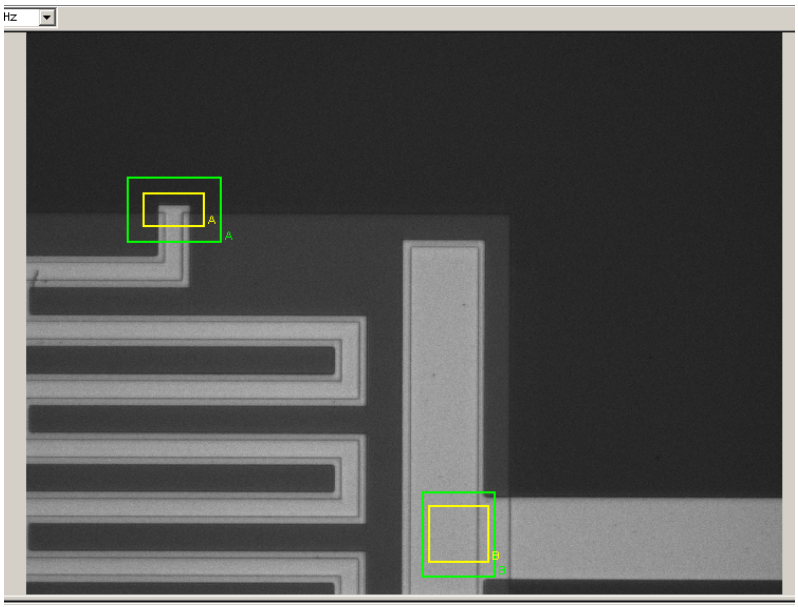


**Figure 4-21: Pattern acquisition software**

Figure 4-21 shows a typical pattern acquisition image. Two different areas can be selected at the same time (this feature allows for differential measurements). Both areas are surrounded by two rectangles: the smaller rectangle (yellow rectangle) includes the features that will be taken as reference for the displacement calculation, while the bigger rectangle (green rectangle) bounds the region of the image in which the features will be researched in successive images.

# 5. Test Setup Validation

Once the test setup has been realized and assembled, the further step is to perform a validation of the system. This step is needed in order to gain information about the behaviour of the system and ensure that it is suitable for the tests that have to be performed.

The validation consists of different types of tests and measurements:

- Vacuum test: the goal is to check the system for leakages in the connections or other problems that may affect the vacuum tightness of the system (like out-gassing).
- Quasi-static measurements: the goal is to define the behaviour of the system in quasi-static conditions. This behaviour is principally affected by the presence of hysteresis.
- Dynamic measurement: the goal is to define the behaviour of he system with respect to frequency in order to define the useful bandwidth for measurements. The product of these measurements is displacement-frequency graph of the system.
- Noise characterization: since we need a very precise measurement of very small displacement, noise is an important issue. Two main noise source are considerer and characterized: environmental noise and electronic noise
- Test simulation: a test simulation has been performed using a system with characteristics similar to the gradiometer: low resonance frequency and high quality factor. The scope of this test is to ensure the suitability of the system for this kind of measurements.

## *5.1. Vacuum Tests*

In section 3.1.4 we discussed the necessity to have the system under vacuum in order to keep air damping under control. One more constraint comes from the actuator: because of the great reduction of dielectric breakdown strength of air, the piezoelectric actuator should not be operated in the pressure range $10^{-1}$-$10^{2}$ *mbar* [31]. Using a value of the pressure of about $10^{-3}$ *mbar* we can both keep the air damping to a low value and avoid any problem with the piezo-electric actuator.

A series of tests has been performed in order to define the behaviour of the setup when under vacuum conditions.

Connections have demonstrated to be tight enough; no significant leakage has been recorded. The main problem we have had when pumping down the vacuum chamber is represented by the out-gassing. Air may be trapped inside the walls or small creeps in the walls of the chamber, in the electrical wires and in the actuator itself (for instance, in the glue used to assemble it).

A way to face the problem is to heat the chamber up for a certain time in order to free the air molecules trapped in the different components of the system. The heating up process has been performed using a simple thermal wire based on Joule effect.

Scope of these tests is to optimize the out-gassing procedure and characterize the behaviour of the system under vacuum conditions.

The out-gassing procedure consists of the following steps:

1. Heat up the vacuum chamber using a thermal wire and wrapping it with aluminium foils, in order to reduce heat losses.
2. Switch on the vacuum pump.
3. Disconnect the thermal wire and let the system cool down while the vacuum pump is still working. In this phase pressure drops since the temperature diminishes.
4. Close the valve and switch off the vacuum pump.

At this point the value of the pressure in the chamber is recorded by means of a pressure sensor. A first test has been performed under the conditions described in Table 4:

| | |
|---|---|
| ***Out-gassing process time*** | *12 hours* |
| ***Temperature of the thermal wire (at the end of the process)*** | *60º C (P=120 W)* |
| ***Temperature of the actuator (measured with a thermocouple at the end of the process)*** | *37ºC* |

**Table 4: Out-gassing process parameters for the first test**

The pressure history after cooling down the system, closing the valve and shutting down the pump is shown in Figure 5-1.

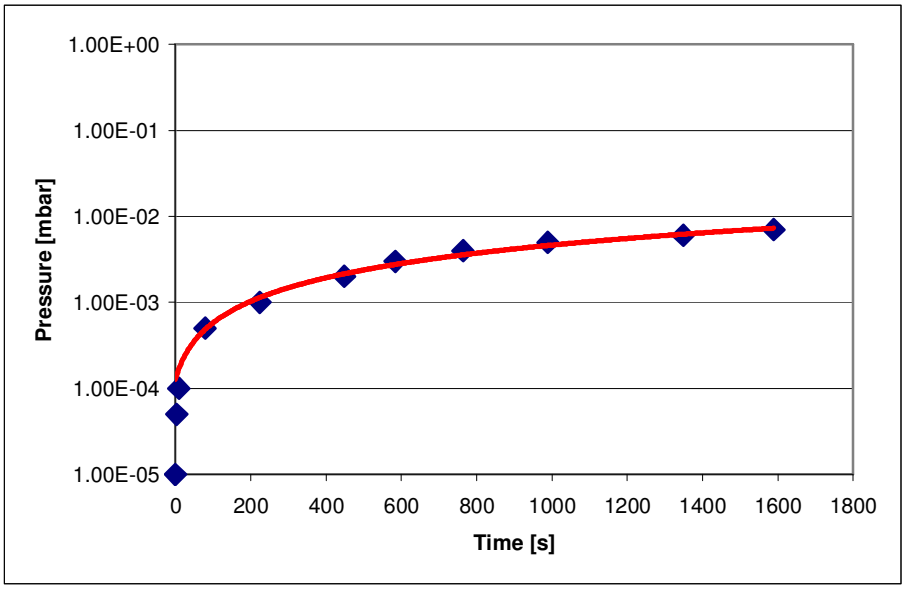


**Figure 5-1: Pressure history of the vacuum system**

The lowest value of pressure reached after cooling down the system was: $p \approx 7x10^{-6}$ *mbar* (temperature of the actuator: *25ºC*). The pressure reaches a value of about $10^{-2}$ *mbar* in approximately *30* minutes. This behaviour is not satisfactory: the pressure level of $10^{-2}$ is reached too fast. A complete measurement with a gradiometer would take up to several hours.

This test, anyway, has been performed using a quite low temperature for heating up the vacuum cell. The reason lays in the fact that the temperature operation limit of the actuator is around 80ºC (this is, however, the operational temperature range). We did not want to push the instruments to its limits, but, since the result of this test was not completely satisfactory, we tried again with a higher temperature. The parameters used for this new test are listed in Table 5.

| | |
|---|---|
| ***Out-gassing process time*** | *96 hours* |
| ***Temperature of the thermal wire (at the end of the process)*** | *85º C (P=130 W)* |
| ***Temperature of the actuator (measured with a thermocouple at the end of the process)*** | *82ºC* |

**Table 5: Out-gassing parameters for the second test**

This time the minimum pressure value reached after cooling down the system was $4.0x10^{-7}$ *mbar*. The system remained between the pressure values of $10^{-4}$-$3x10^{-3}$ *mbar* for about *24* hours after closing the pressure valve. This result is completely satisfactory both in terms of pressure level and time.

In conclusion we can say that the system does not present leakage but is very affected by out-gassing. In order to have a good vacuum condition, attention must be paid to the out-gassing process. A couple of days of out-gassing would be more than enough to ensure a good vacuum level for a sufficient time.

## *5.2. Quasi-static Measurements (Hysteresis measurements)*

The quasi-static behavior of a piezo-electric actuator is dominated by the phenomenon of hysteresis. Dielectric, elastic and ferromagnetic properties of a material all have a role in the complex phenomenon of the hysteresis.

Goal of this test is to measure the hysteresis of the instrument. This will give information about the reliability if the system, through the knowledge of the possible errors in position of the instrument. Only the piezo-actuator has been tested, without any structure connected to it.

The measurement consists of focusing and following a spot of the surface of the actuator while a DC current signal is provided. A micro-camera (magnification *7x*, *500 μm/50*) has been used in order to image the surface of the actuator.

It is possible to superimpose a grid to the image acquired by the camera. A white spot on the plate is taken as reference point and is followed throughout the measurements. The dimension of the squares of the grid is of *25 μm*. Every time the white spot crosses a line of the grid, the voltage is recorded using an oscilloscope. The voltage is changed manually turning the knob of the amplifier in a quasi-static mode (DC mode). The electronic apparatus used consists of the amplifier from Piezosystemjena Company [32] and an oscilloscope used to measure the voltage values.

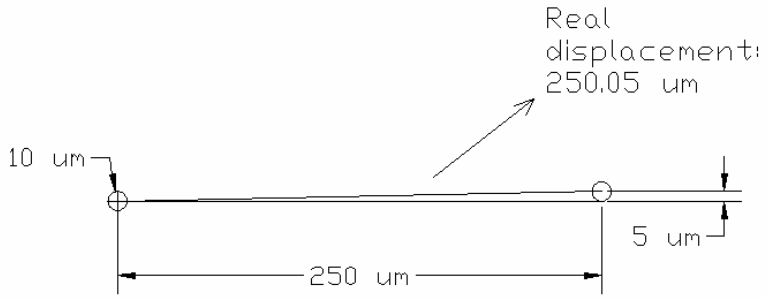


**Figure 5-2: Real displacement of the reference point**

The dimension of the white spot is approximately *10 μm* (see Figure 5-2). The actuator was not perfectly aligned with the gridline; however, the real displacement should differ only about *0.05 μm* (*50 nm*) from the nominal one (that is *250 μm*), see Figure 5-2.

Two kinds of tests have been performed. The first test (section 5.2.1) is a whole stroke measurement. The hysteresis of the actuator is measured throughout the whole stroke length of the instrument.

The second test (section 5.2.2) consists of a measurement of the hysteresis in small loops. This test simulates the behavior of the system in dynamic operations. Since, when operated in AC mode, the input signal will have small amplitude, the displacement will be a fraction of the whole stroke length.

### 5.2.1. Whole stroke measurement

Figure 5-3 shows the images acquired for this measurement; the reference point is marked by the red arrow. The measured points at *0, 100, 200, 250, 200, 0 µm*, are shown in Figure 5-3.a, b, c, d, e and f, respectively. The entire set of measurement is reported in the graph of Figure 5-4.

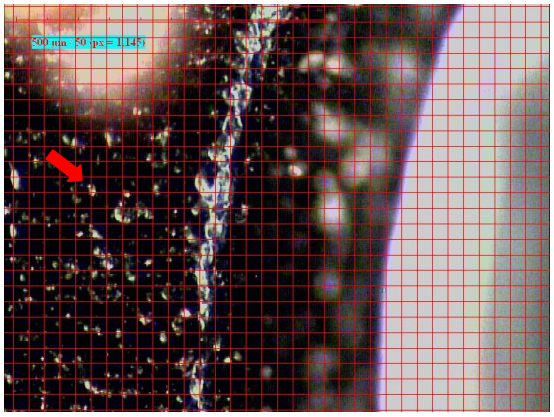

**a. V=-1.81, d=0 µm**

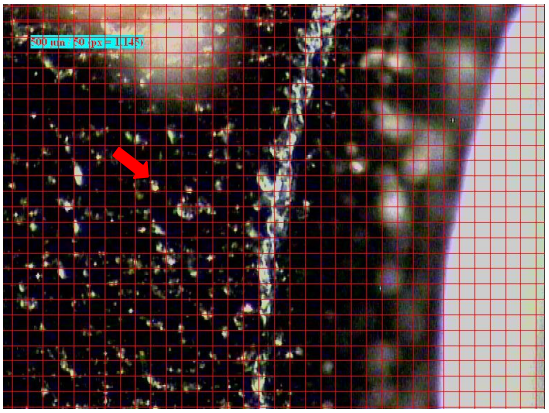

**b. V=5.08, d=100 µm**

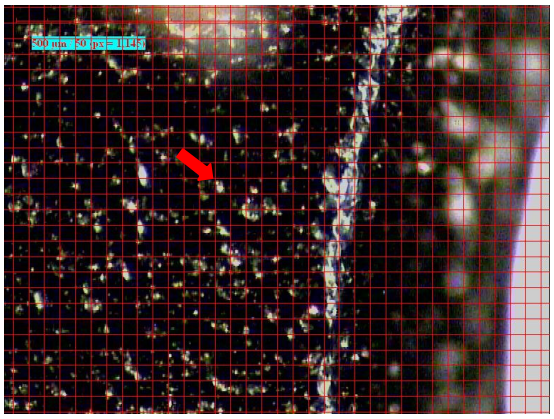

**c. V=10.1, d=200 µm**

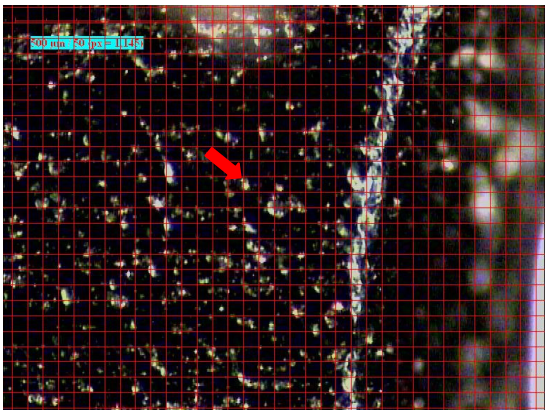

**d. V=12.2, d=250 µm**

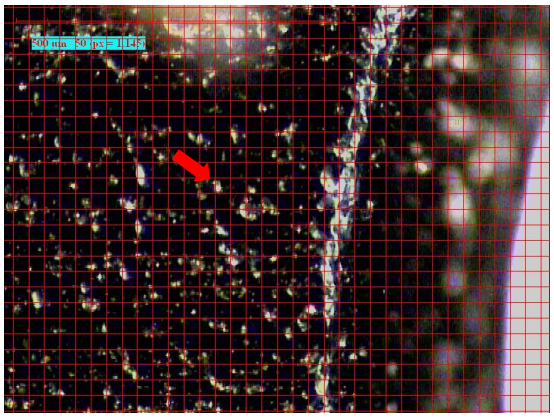

**e. V=8.26, d=200 µm**

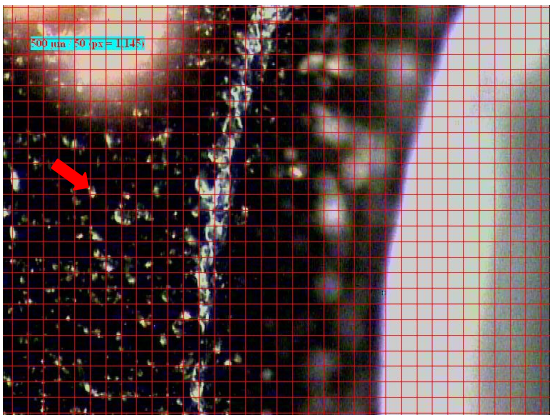

**f. V=-1.81, d=0 µm**

**Figure 5-3: Captured images from whole stroke measurement**

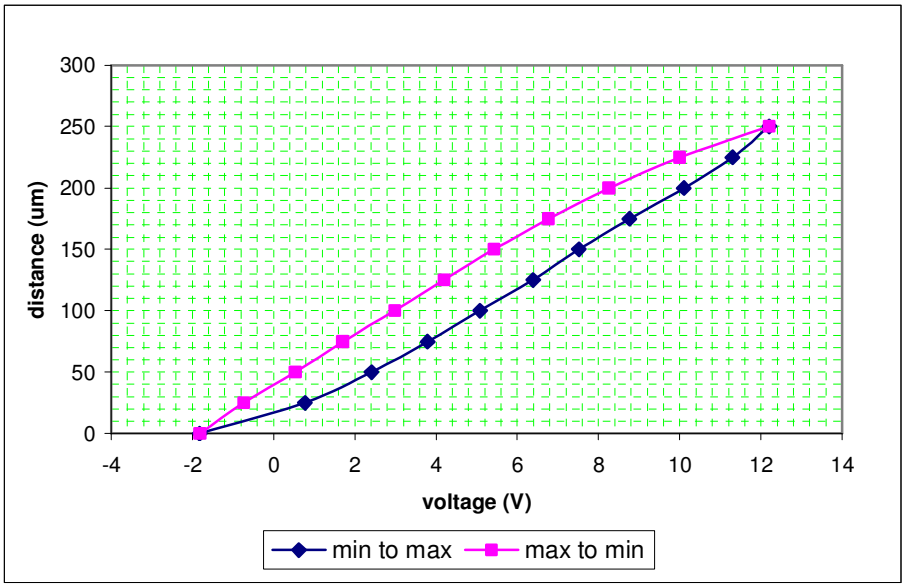


**Figure 5-4 : Hysteresis measurement on the whole stroke length**

From the graph, is very clear the hysteretic behavior of the system. The maximum hysteresis can be calculated as the ratio between the maximum difference of distance at the same voltage, and the maximum distance.

Taking as reference the displacement at *V=5.08 V*, the distance on the first branch (from the minimum value to the maximum value, or increasing branch) reads *100 μm*, while the distance on the second branch (from the maximum value back to the minimum value, or decreasing branch) reads *143.27 μm*. Therefore, the difference is *43.27 μm*, the total stroke length is *250 μm* and the hysteresis is:

$$Max\ Hysteresis:\ 43.27/250=0.1730 \rightarrow 17.30\%$$

### 5.2.2. Hysteresis in loops

A further measurement had the scope to check the behavior of the actuator when it operates in small loops rather than the whole stroke length. With small loop here, we meant a loop which starting and final points are inside the hysteresis figure shown in Figure 5-4.

The measurements have been performed in the same way described in the previous section. Only the two most representative measurements are presented in this section.

In measurement presented in Figure 5-5, the starting point is at *d=100 μm* and *V=3.23 V*; it is on the decreasing branch. The end point is at *d=200 μm*.

We can see that the loop seems to recreate the hysteresis figure in smaller proportion. The maximum hysteresis is *~12.5%*.

In measurement of Figure 5-6, the starting point is at *d=100 µm* and *V=2.97 V*. It is on the decreasing branch. The loop goes down to *50 µm*, then up to *150 µm* and again back to *100 µm*.

Again the loop seems to recreate a hysteresis figure between the lowest point and the highest point of the loop. The maximum hysteresis is *~12%*.

This behavior is consistent with ones that can be found in literature [36]. A hysteresis equal to *12%* should not interfere with the measurements, but, anyway it can be taken into account for computation of the uncertainty of the measurements.

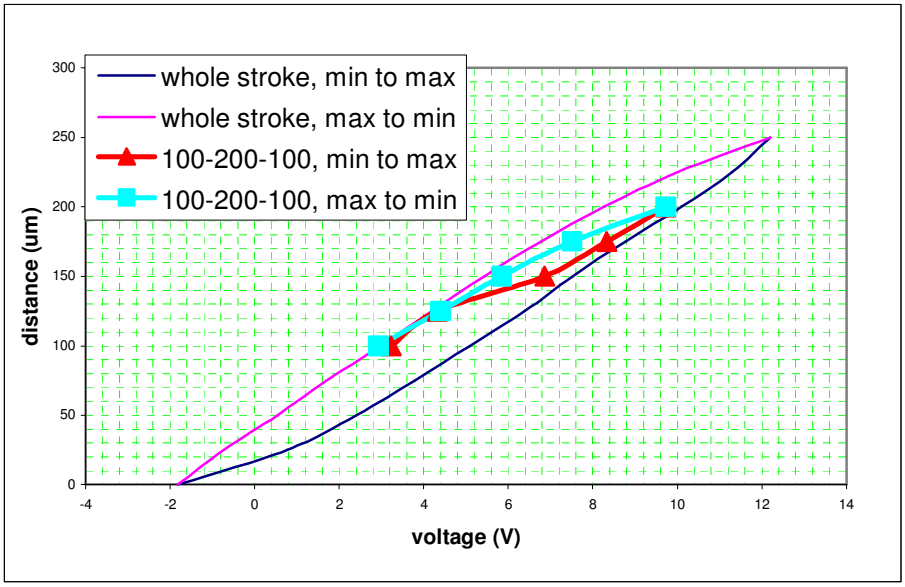


**Figure 5-5: Hysteresis measurement; Loop 100-200-100**

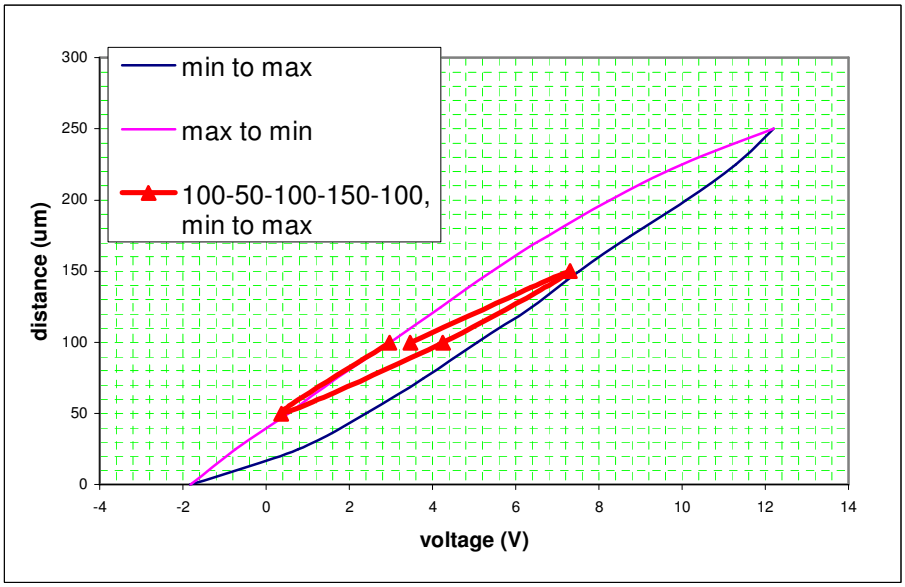


**Figure 5-6: Hysteresis measurement; Loop 100-50-100-150-100**

## 5.3. Dynamic Measurements

In these measurements the whole setup described in section 4 is tested. In order to characterize the system, we used a silicon wafer without any etched structure onto it. In this way, we will measure the displacement that would be transmitted from the actuator to the masses of the gradiometer, passing trough the supporting structures (not the displacement of the masses, object of the tests the system has been designed for). As read-out system, the Micro-analyzer system (section 4.3) is used.

The test consists of exiting the actuator with a sine wave, measure the response of the system both in displacement and phase.

Scope of the tests is to determine the transfer function of the instrument, both the amplitude and phase response. From the graphs we can gain information about the real amplitude of the instrument at every frequency and determine the useful frequency bandwidth, the cut-off frequency and the resonance frequency (or frequencies).

### 5.3.1. Atmospheric pressure test

First tests have been made at atmospheric pressure (*1 bar*). Two cases are considered: test with *3 mm* thick wafer holder and test with *2 mm* thick wafer holder. This test has different scopes. Together with the transfer function of the system in atmospheric pressure, we can determine which one between the two wafer holders (section 4.2.2) the *3 mm* thick or the *2 mm* thick is more suitable for future measurements. Moreover, we can gain information about the changing of the transfer function of the system with changes in the mass.

*3 mm thick wafer support*:

The parameters used for this test are listed in Table 6. The parameters of the sine electrical signal (Voltage offset and Peak-to-peak Voltage) are displayed in Figure 5-7.

| | |
|---|---|
| ***Bandwidth*** | *1 Hz-10 kHz* |
| ***Magnification*** | *x10* |
| ***Voltage offset*** | *0.15 V* |
| ***Peak-to-peak voltage*** | *0.1 V* |

**Table 6: 3mm thick wafer support test paramteres**

“Magnification” in the parameters refers to the lens used to image the silicon wafer on top of the structures.

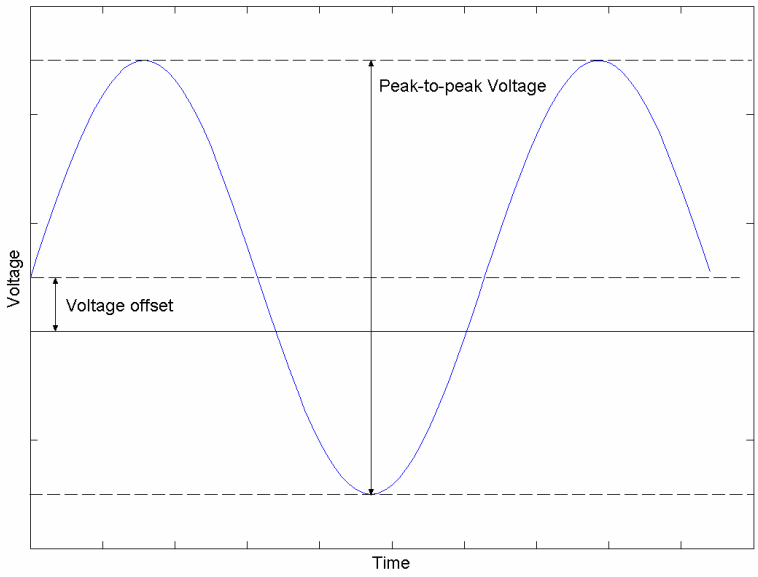


**Figure 5-7: Sine electrical input signal. Voltage offset and Peak-to-peak voltage are the parameters that can be changed in different measurements**

The bode plot and the phase diagram resulted from the measurement are shown in Figure 5-8 and Figure 5-9 respectively.

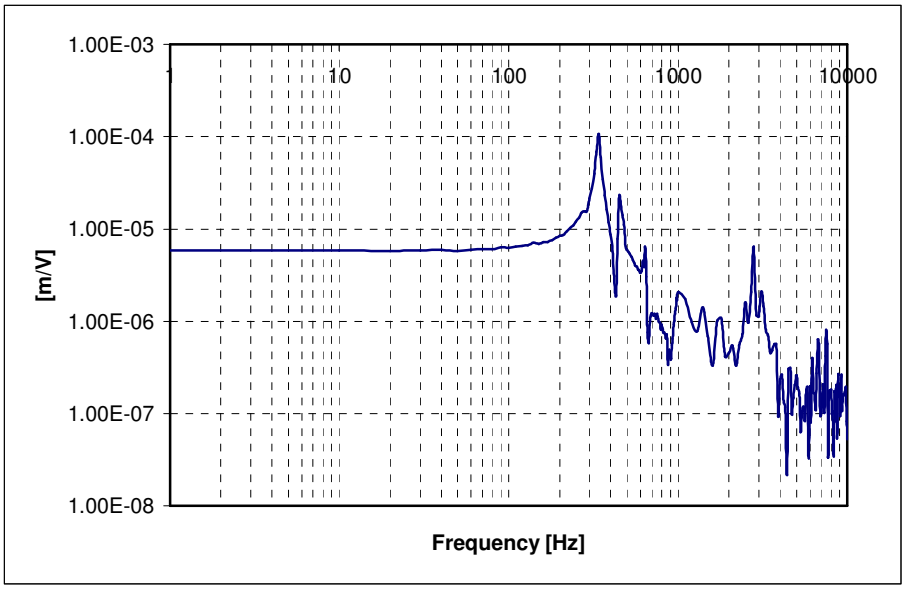


**Figure 5-8: Amplitude diagram 3mm thick support wafer**

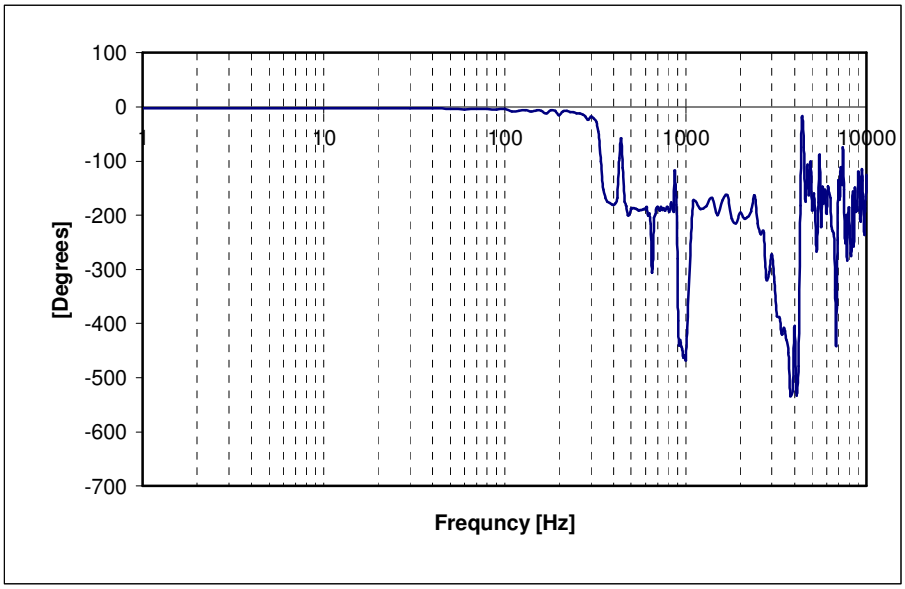


**Figure 5-9: Phase diagram 3mm thick support wafer**

We can draw some conclusions from those diagrams: first of all, the behavior of the system is linear in the bandwidth *1-100 Hz* approximately. Moreover, the system has a typical 2nd order system behavior (see section 3.2) until *400 Hz* (linear region, peak that corresponds to the resonance frequency and -3dB region). We can recognize a first peak at *340 Hz*. This peak, most probably depends on the intrinsic resonance frequency of the piezo-actuator (see section 4.2.1). The phase diagram confirms this analysis: until *400 Hz* it is a typical phase shift diagram of a 2nd order system (180° phase shift before and after the resonance frequency). After the mean peak, the behavior of the system becomes to be extremely chaotic and difficult to model. This most probably depends on the fact that vibrations modes of the support structures start to be excited.

*2 mm thick wafer*

This test has been performed using the same wafer and the *2 mm* thick wafer holder. The parameters used for this test are the same used for the previous test and listed in Table 6.

The Bode diagram and the phase diagram are shown in Figure 5-10, Figure 5-11 respectively.

We can notice that the mean peak has shifted to *350 Hz*. A second peak at *420 Hz* is also present and has the same dimension as the mean one. This second peak was also present in the previous test, although it was much smaller. The shifting of the peak is consistent with the values suggested by the actuator datasheet [31]. The values for the resonant frequency against the mass, as reported on the datasheet (the reported accuracy is *+/-20%*), are showed in Figure 5-12 while the presence of the second peak can be explained by a decreased stiffness of the *2 mm* thick wafer holder, with respect to the *3 mm* thick one.

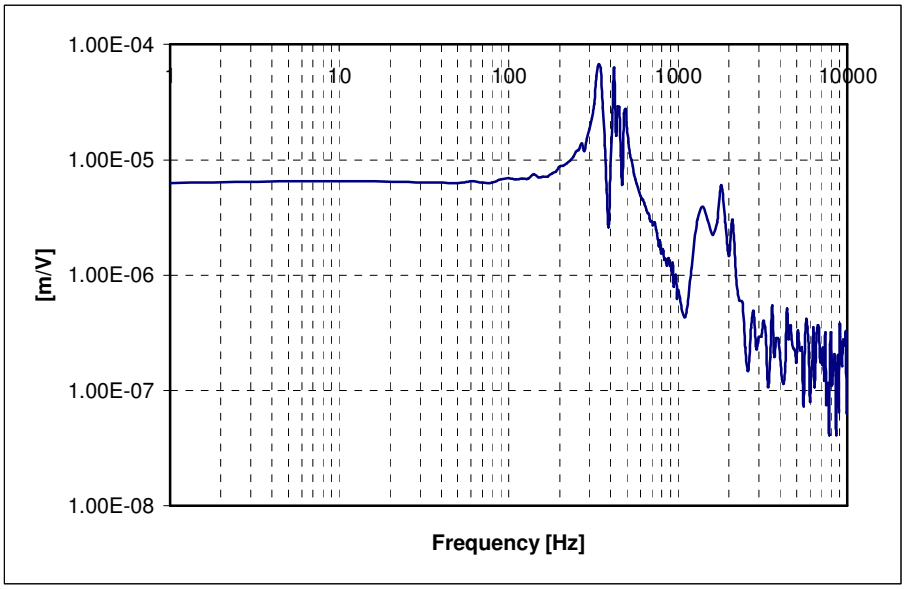


**Figure 5-10: Amplitude diagram 2mm thick support wafer**

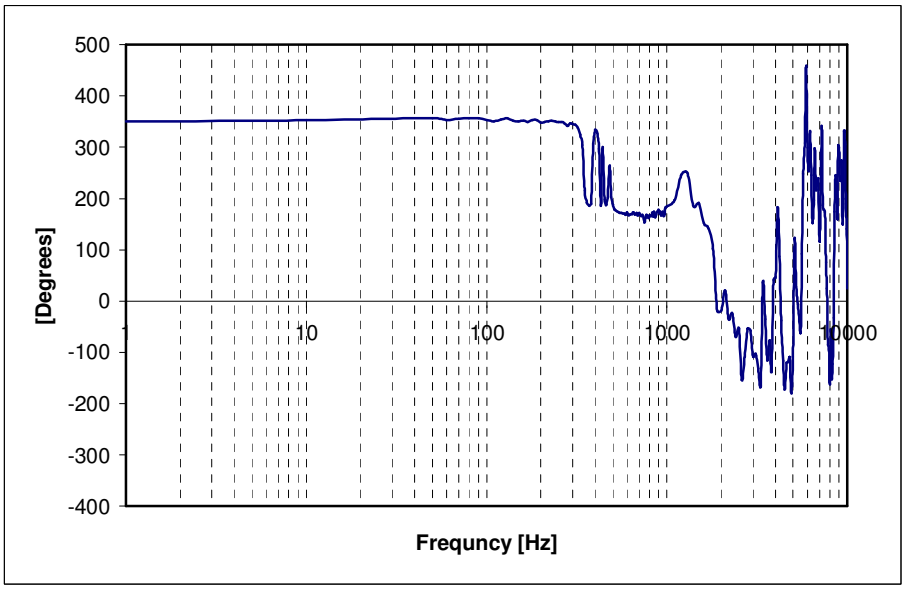


**Figure 5-11: Phase diagram 2mm thick support wafer**

The estimated mass of the structure mounted on the actuator (wafer holder plus wafer) is about *180 g* for the *3 mm* thick holder and about *165 g* for the *2 mm* thick holder (the holder is made of Stain steel SS316, $\rho$=*8.00 g/cm*$^3$).

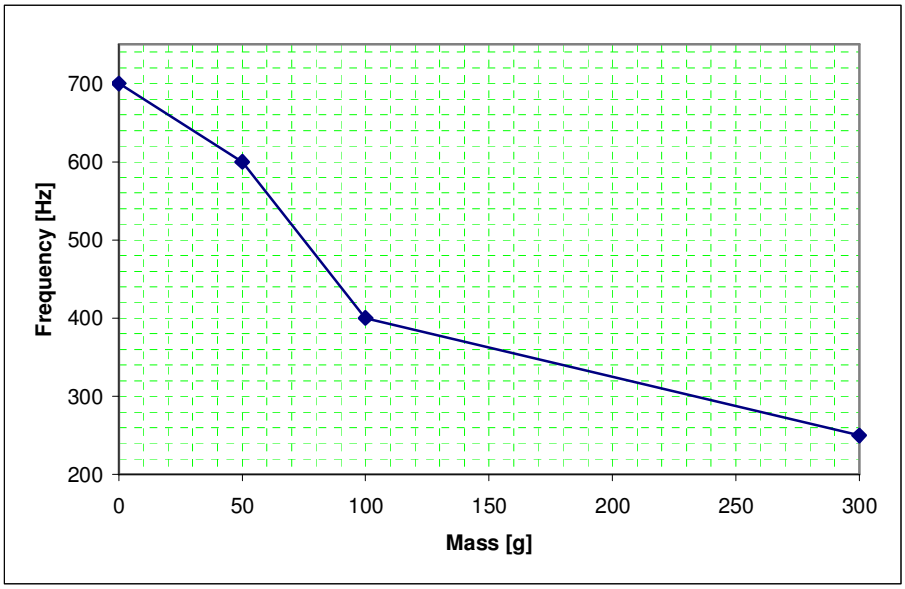


**Figure 5-12: Diagram of load mass against natural frequency for the piezo-electrical actuator. The values are taken from the datasheet of the instrument [31].**

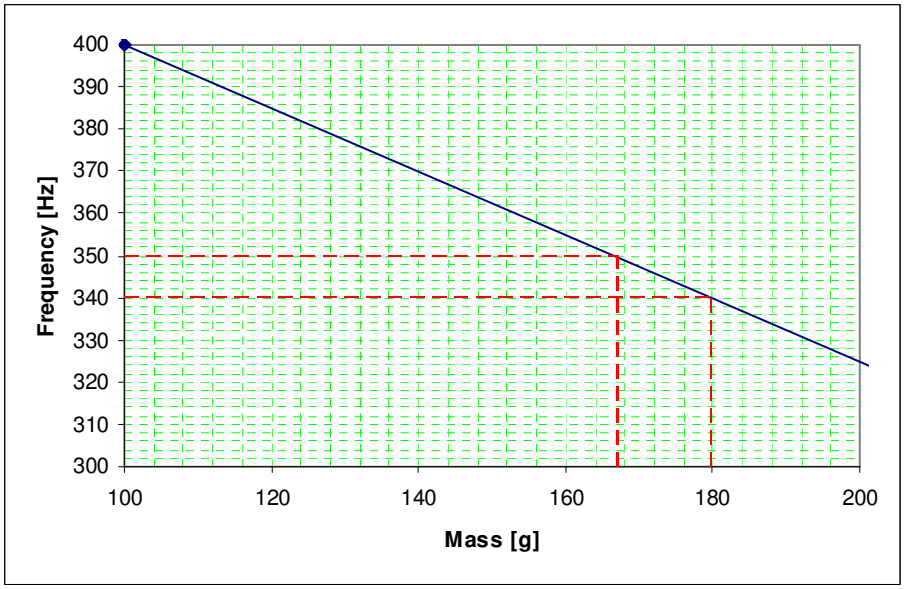


**Figure 5-13: Diagram load mass against natural frequency, zoom in**

The change in resonance frequency is also compatible with the relation expressed by equation 3.21. In fact, a change of mass of *15* grams, will lead in a change of resonance frequency of about *10 Hz*:

$$\begin{cases} m_1 = 180g, \quad \omega_{n1} = 340Hz = 2135.2rad/sec \\ m_2 = 165g, \quad \omega_{n2} = 350Hz = 2198.0rad/sec \end{cases} \qquad (5.1)$$
$$m_1 \cdot \omega_{n1}^2 \approx m_2 \cdot \omega_{n2}^2 = k = 820634.22N/ms$$

### 5.3.2. Vacuum Tests

The successive step is to test the system under vacuum condition. The test has been performed after the out-gassing procedure described in section 5.1. The silicon wafer is the same used for the previous tests (wafer without etched structures). The test parameters used for this test are listed in Table 7:

| | |
|---|---|
| ***Bandwidth*** | *1 Hz-10 kHz* |
| ***Magnification*** | *x10* |
| ***Voltage offset*** | *0.15 V* |
| ***Peak-to-peak voltage*** | *0.1 V* |
| ***Pressure: beginning of the test*** <br> ***end of the test*** | $P=3.6x10^{-4}$ *mbar* <br> $P=8.0x10^{-4}$ *mbar* |
| ***Duration of the test*** | *90 min (approx.)* |

**Table 7**

The results of the tests are showed in Figure 5-14 and Figure 5-15.

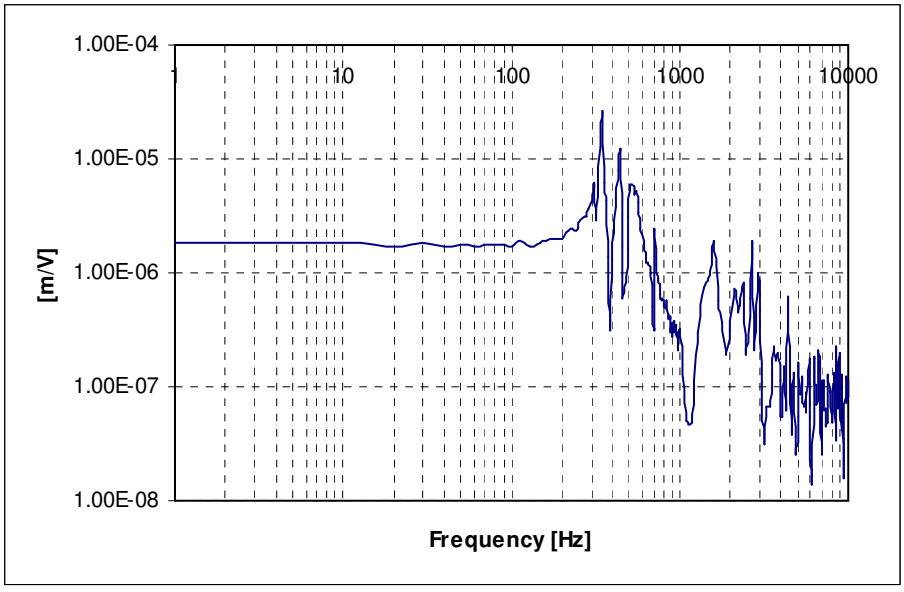


**Figure 5-14: Amplitude diagram, Vacuum test**

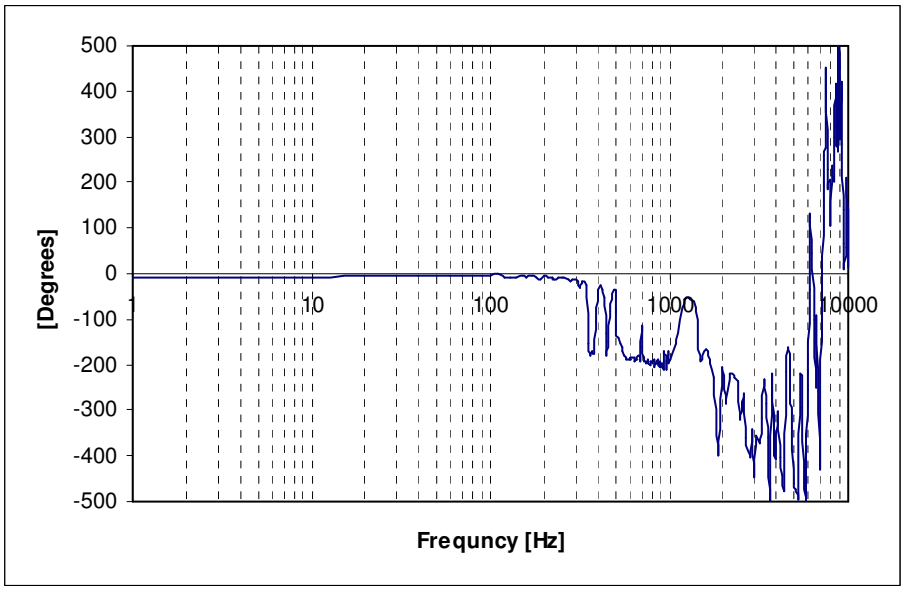


**Figure 5-15: Phase diagram, Vacuum test**

Figure 5-16 represents a comparison between test using *1 bar* pressure and the vacuum test. We can notice that the shape of the two curves is approximately the same, but the values of the displacement in the vacuum test (especially in the bandwidth *1-100 Hz*) are smaller with respect to the displacements at atmospheric pressure. This was an unexpected result, since the pressure should not have influence on the behavior of the piezoelectric elements and on the displacement values.

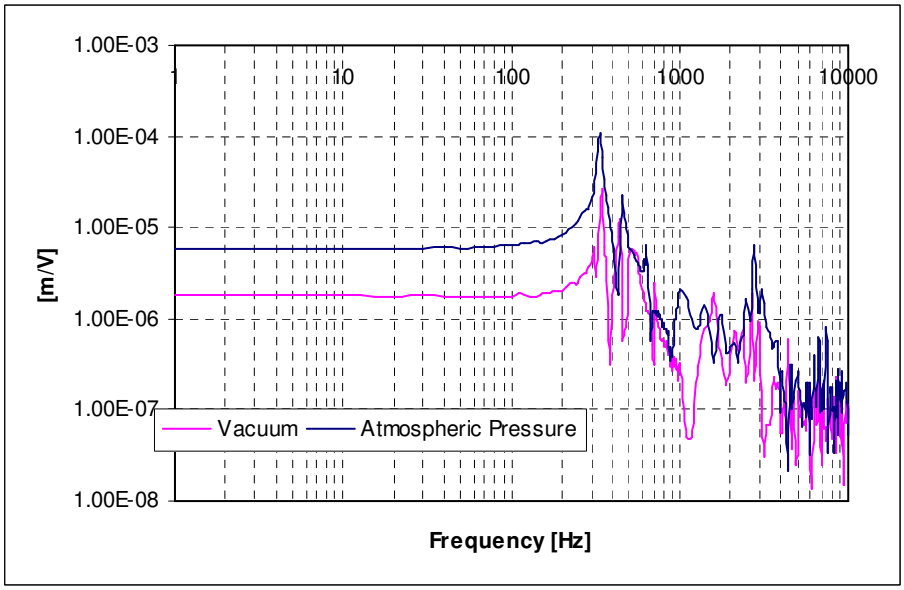


**Figure 5-16: Amplitude comparison between atmospheric pressure test and vacuum test**

The cause of this effect had been recognized in the de-polarization effect of the piezoelectric elements inside the actuator that, in turns, depends on the high temperature used for the out-gassing process (*80ºC*).

For this reason, another test has been performed after a depolarization process, in order to verify this assumption.

### 5.3.3. Polarization tests

The re-polarization process consists of slowly feeding the piezo-actuator with the maximum voltage and then come back to the minimum value of the voltage. After having performed the re-polarization of the piezo-electric elements, the test described in the previous section has been repeated. The parameters used are the same listed in Table 7. The comparison between the results of the displacement, of this test and the previous tests is shown in Figure 5-17.

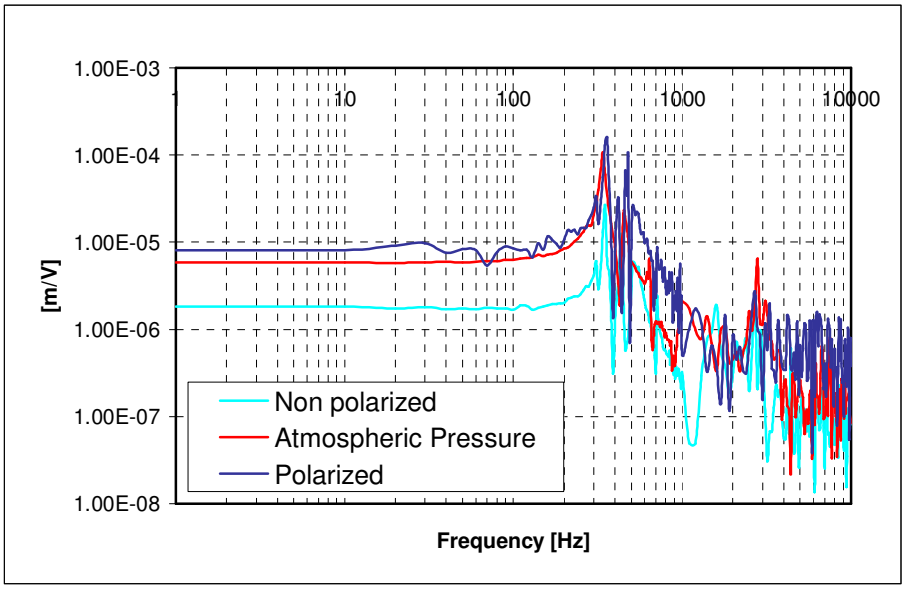


**Figure 5-17: Amplitude comparison between Polarized, non polarized and atmospheric pressure**

The results show clearly that the values of the displacement are similar to the value of the tests without out-gassing. This confirms the idea that the decreasing in displacement values was due to depolarization. In reality the displacements for this test are slightly bigger than the values gained from the tests in atmospheric pressure. This means that polarization, in a certain degree, always occurs, even without high temperature. It is recommendable, hence, to perform a polarization before every measurement.

## *5.4. Noise characterization*

Another important issue, for the performance of a good measurement, is noise. Measurements we intent to perform on a gradiometer require a very quiet environment. The input displacement needs to be very small (fraction of micrometer) even very small noise source may create unacceptable inaccuracies in the measurements.

The major error sources have been recognized in the noise from the environment and the noise from the electronics. They will be object of the next sections.

### 5.4.1. Environmental noise

Some years ago, vibration measurements have been performed by F. Segerink, in and around the EL-TN and CT building, in order to quantify vibration criteria for laboratories involving nanotechnologies and improvement of sensitive measurement setup by obtaining knowledge of vibration of the building's floor and the effect of vibration isolation.

Using those results, we can perform a study aimed to characterize the environment in which we will perform our tests.

The environmental noise measurements have been performed with an accelerometer. The measurements have been preformed in *x* and *y* direction that correspond to south-north and west-east direction, respectively.

The considered location is the $6^{th}$ floor; we can consider its situation very close to the environment in which the vibrometer is installed ($7^{th}$ floor). The measurements comprise a damping vibration table of the equipment called "Shemm". The vibrometer is also installed on a damping vibration table.

Furthermore, the analysis will be focused on the low frequency band (*1-500 Hz*), being the most interesting for our purpose (the resonance frequency of the gradiometer will be in the *1-10 Hz* bandwidth) and, at the same time, the bandwidth with the highest noise level. The results of the measurements are presented in the next graphs.

*Ground Measurements:*

Figure 5-18 and Figure 5-19 show the results of the measurements for acceleration and displacement of the floor, in *x* and *y* directions.

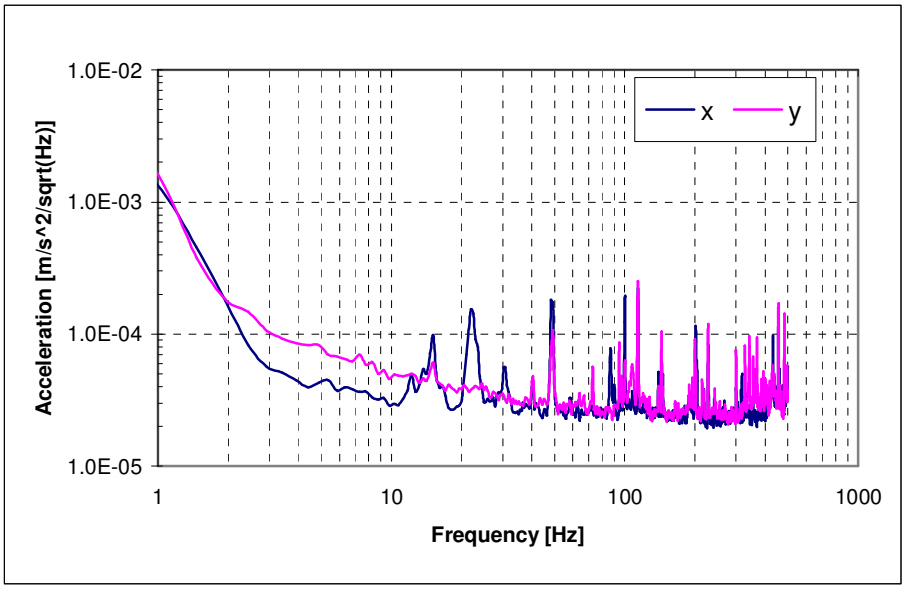


**Figure 5-18: Acceleration measurement, 6th floor, ground**

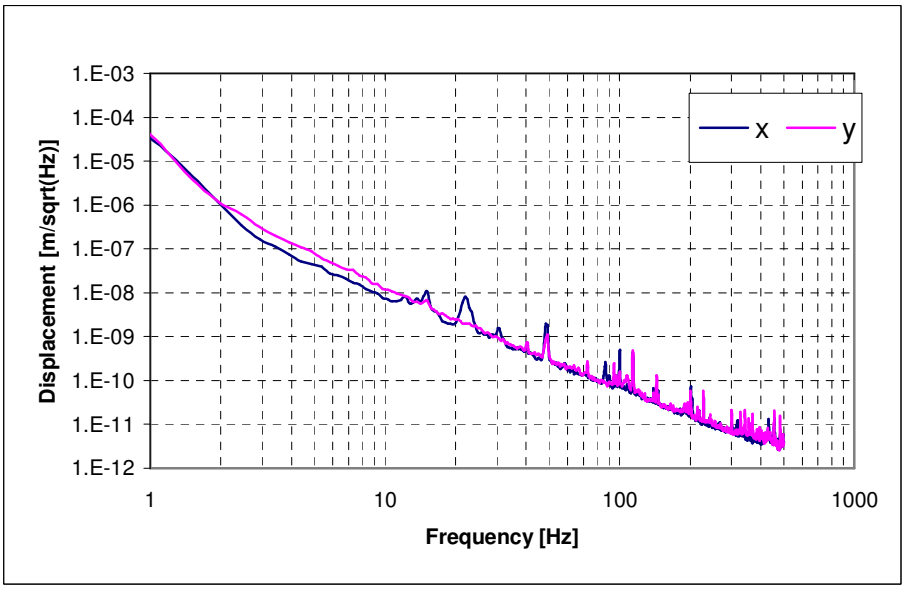


**Figure 5-19: Displacement measurement, 6th floor, ground**

From these measurements, we can already recognize that the most quiet direction is the *x* (south-north) direction, that corresponds to the longest (and most stiff) side of the building. This is especially true in the *2-10 Hz* bandwidth.

*Optical table Measurements:*

Figure 5-20 and Figure 5-21 show the results of the measurements for acceleration and displacement performed on the optical table of the "Shemm" equipment. Again, *x* and *y*

directions are considered. The measurements on the optical table confirm the observation that the *x* direction is the quietest.

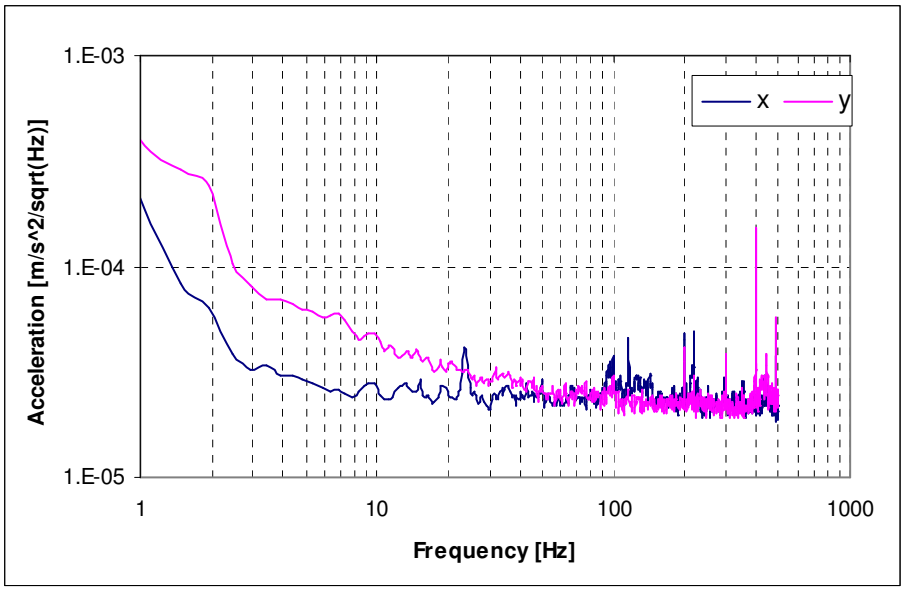


**Figure 5-20: Acceleration measurement, 6th floor, optical table**

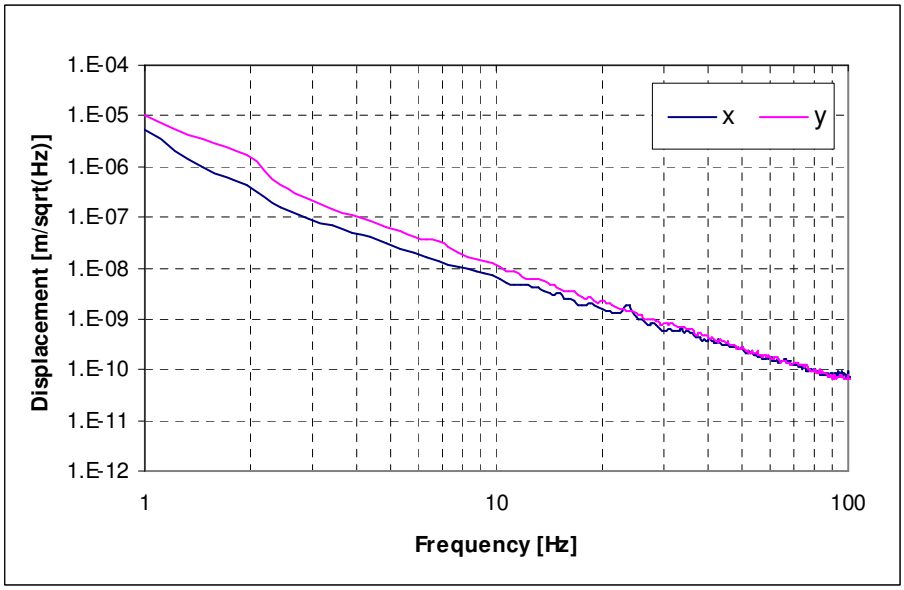


**Figure 5-21: Displacement measurement, 6th floor, optical table**

*Comparison ground-optical table:*

Figure 5-22 and Figure 5-23 present the comparison between the noise level of the floor and the optical table. This time, only the *x*-direction is considered, being the quietest direction.

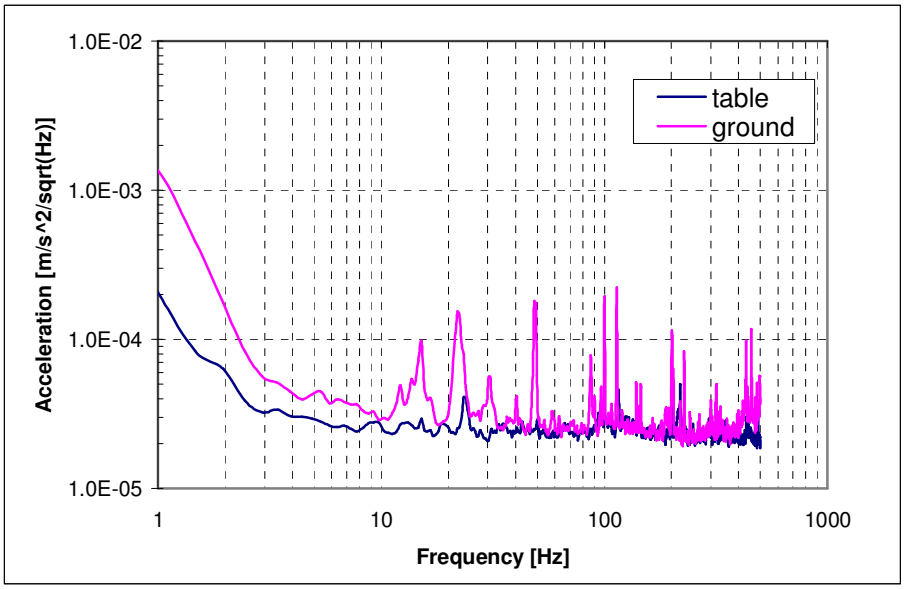


**Figure 5-22: Acceleration comparison between ground-optical table**

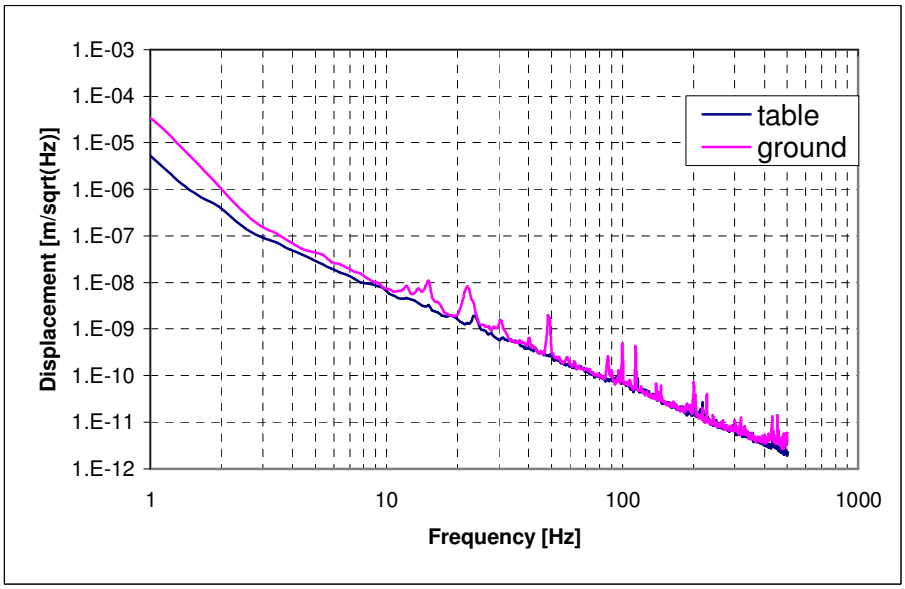


**Figure 5-23: Displacement comparison between ground-optical table**

In conclusion, it is possible to say that the displacements on the optical table are one order of magnitude smaller with respect the ground displacement, in the *1-10 Hz* bandwidth. Above *10 Hz*, the two displacement levels are more or less similar. However, the damped optical table cuts the displacements peak. This behaviour is even more critical in the acceleration measurement. In this case the peaks are very efficiently cut by the optical table. The results of these measurements will be compared with electronic noise and actuation level from the actuator in the following sections.

### 5.4.2. Electronic noise

The electronic equipment used for the tests comprises the function generator integrated in the MS4-400 Micro system analyzer [35] and the amplifier from Piezosystemjena Company [32]. The electrical noise generated by the electronic equipment has been measured by connecting the function generator and the amplifier to a power spectrum analyzer and feeding them with a sinusoidal signal at *1 kHz* frequency (the peak due to the input signal has been removed since it is not significant for a noise measurement purposes). The result of the measurement is shown in Figure 5-24.

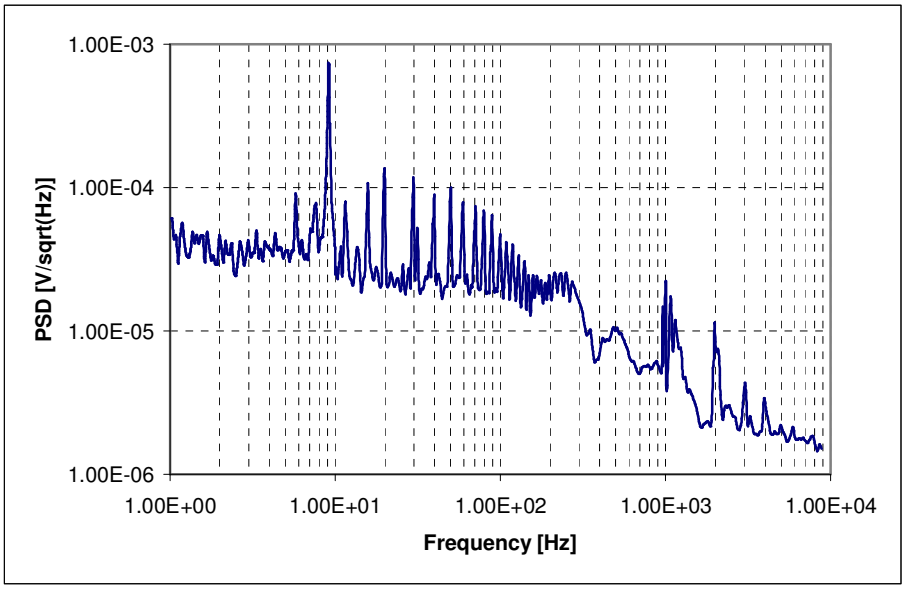


**Figure 5-24: Power spectral density of the electronic noise**

The electronic noise curve presents several peaks; they are due to the power net. The frequency of the net is *10 Hz*, while the other small peaks depend on uneven harmonics of the power net.

### 5.4.3. Noise comparison

In order to fully compare the noise values gained from environmental and electronic noise measurement, with displacement of the actuator, we need to convert the amplitude spectral density and the power spectral density of the displacement and electronic noise measurements in displacement.

We will accomplish this conversion according to the equation:

$$x_{noise} = ASP \cdot \sqrt{f / N} \quad [m] \tag{5.2}$$

Where *ASP* is the Amplitude spectral density of the displacement due to noise [$m/\sqrt{Hz}$]; $f$ is the considered frequency [$Hz$]; $N$ is the number of measurement points in one period. Here we are assuming that the reference bandwidth ($f/N$) is proportional to the considered

frequency, divided by *N=36*, where *36* is the number of measurements that the vibrometer performs at each frequency (the 36 measurements are taken during different periods but the total time covered by them is equal to one period, see section 4.3.1).

In the same way we need to pass from the Power spectral density of the electrical noise measurement to a displacement. We need a conversion parameter that is intrinsic property of the piezo-electric actuator. This value, taken from the calibration curve of the instrument (provided by the manufacturer), is:

*Voltage/displacement conversion=1.6 μm/V*

If we divided the values of the graph in Figure 5-24 by *1.6*, we obtain the correspondent values in Amplitude spectral density [*m/√Hz*]. Now we can use again equation (5.2) to pass from an amplitude power density to a displacement value.

The result of the comparison between the displacement level and the two major noise sources is shown in Figure 5-25.

It can be seen from the graph, that the environmental noise is dominant in the low frequency region, while the electrical noise is dominant at the high frequencies. Anyway, the noise level is quite low and only in the frequencies *<1 Hz* it is comparable to the displacement of the actuator.

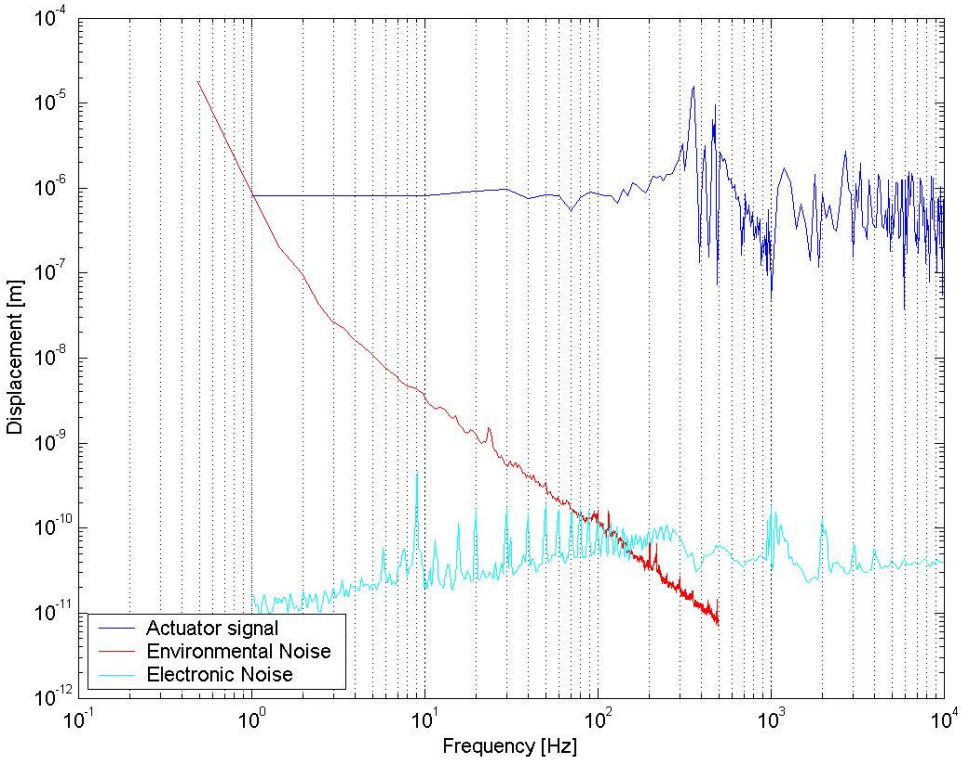


**Figure 5-25: Comparison actuation displacement, environmental noise displacement, electrical noise displacement**

Starting from the graph in Figure 5-25, we can have an estimation of the resolution of the system: we can approximate $Q$ (see section 3.2) as the ration between the maximum displacement and the input displacement at resonance frequency. If we consider as maximum displacement the length of the gap between the masses and the frame, *50 μm*, and as input displacement the value of the noise taken from the graph in Figure 5-25, we can have the maximum measurable $Q$ at each frequency (Figure 5-26). The graph shows also how the reduction of one order of magnitude of the noise can allow a measurement of a $Q$ of one order of magnitude higher.

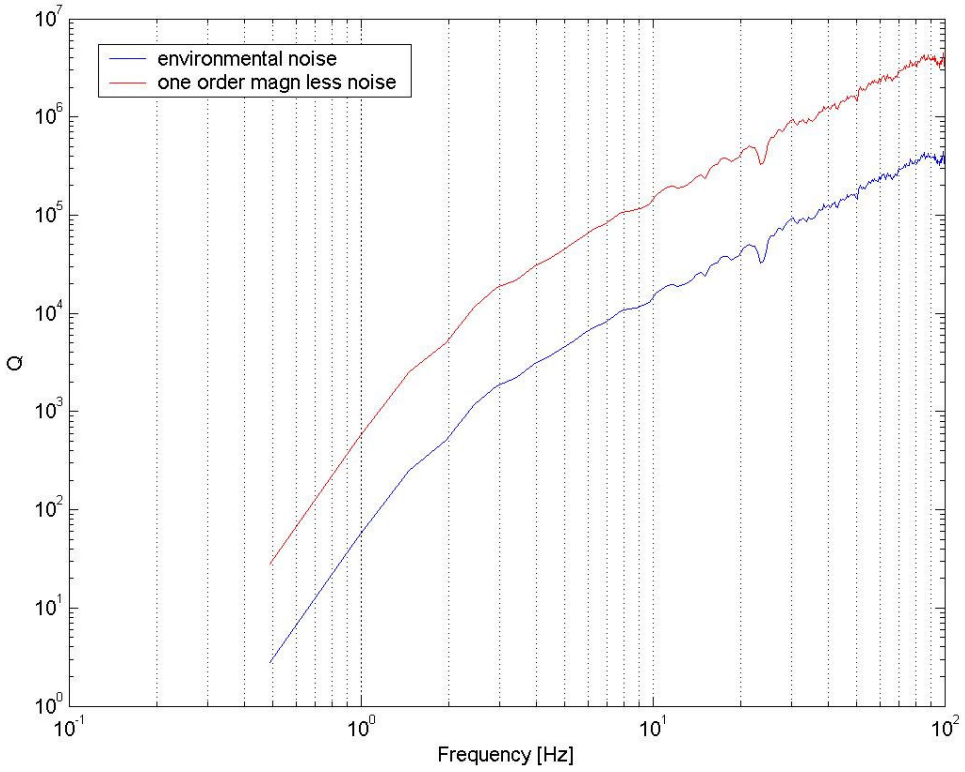


**Figure 5-26: Resolution of the system in terms of maximum measurable Q. The input displacement is the noise level and the maximum allowed displacement is 50 μm**

## *5.5. Test Simulations*

At this point, in order to complete the validation of the system, we need to verify that we are able to actually perform a measurement on a system similar to the gradiometer (low resonance frequency, $\omega_n$, high quality factor, $Q$), tests have been performed on a system that has similar characteristics. The system is composed of a spring with a mass attached to it (Figure 5-27). The system has a resonance frequency around *10 Hz* and will be a good proof to ensure the system is properly working.

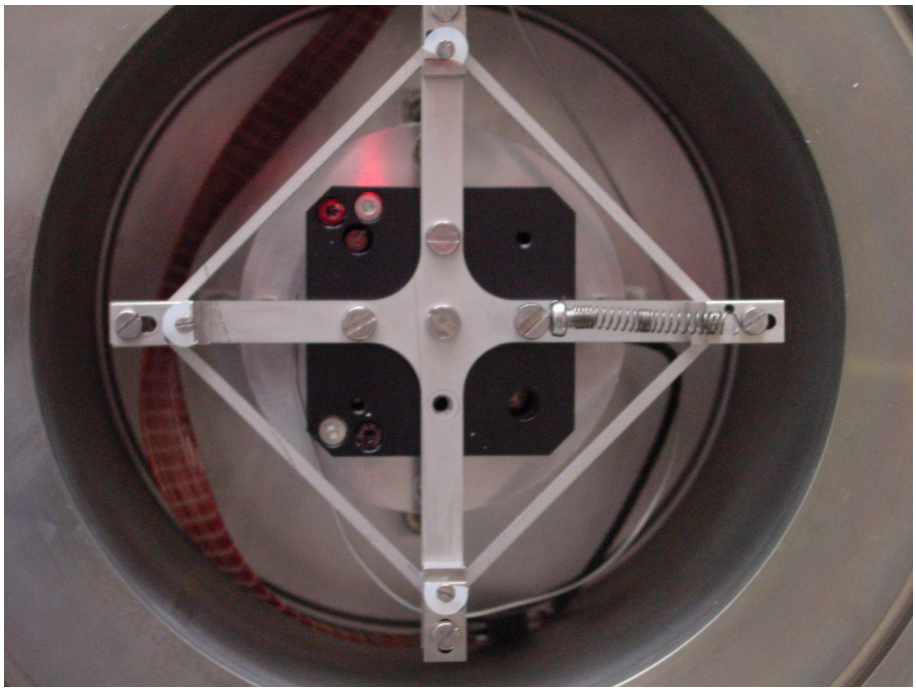

**Figure 5-27: Mass-spring system for test simulation**

### 5.5.1. Frequency sweep

As discussed in section 4.3.1, the best way so far to perform a measurement of a system with low resonance frequency and high *Q*, is a frequency sweep. The system will be exited with sinusoidal signals at different frequencies. Displacement and phase shift will be recorded.

The measurements are performed in a bandwidth of *7-13 Hz*, *10-12 Hz*, and *11.00-11.30 Hz* bandwidth respectively. The bandwidth is successively reduced in order to recognize the resonance frequency with a high accuracy. The parameters of the first measurement are listed in Table 8.

Using a *2.5x* magnification lens, it is possible to have in the same image the moving mass and a fixed mass, used as reference for the differential measurement. Figure 5-28 shows the two masses with the region of the image used for measurement of displacement (colored rectangles).

Some clarifications about the meanings of the parameters are needed. The “bandwidth” defines the frequency interval we are interested in. The “initial period” length is the duration of the first period (it is basically the 1 over the first frequency of the frequency bandwidth). The “settling time” is a crucial parameter for this kind of measurement; it is the time after which a new measurement is performed, the time in which the system is in a rest until a new measurement starts. By increasing the settling time it is possible to refine the measurement. The “frequency step” defines the step of the change in frequency of the input signal. The “shots per period” represents the number of measurement points in a period. This is a fixed number, which means that the sampling frequency changes with respect the frequency we are

investigating. The meanings of the voltage and magnification parameters have already been explained in section 5.3.1.

| | |
|---|---|
| ***Bandwidth*** | *7-13 Hz* |
| ***Initial period length*** | *1/7 s* |
| ***Settling time*** | *5000 ms=5 s* |
| ***Frequency Step*** | *0.5 Hz* |
| ***Shots per period*** | *36* |
| ***Voltage Amplitude*** | *0.2 V* |
| ***Voltage Offset*** | *0.1 V* |
| ***Magnification*** | *2.5x* |

**Table 8: 7-13 Hz bandwidth Test Parameters**

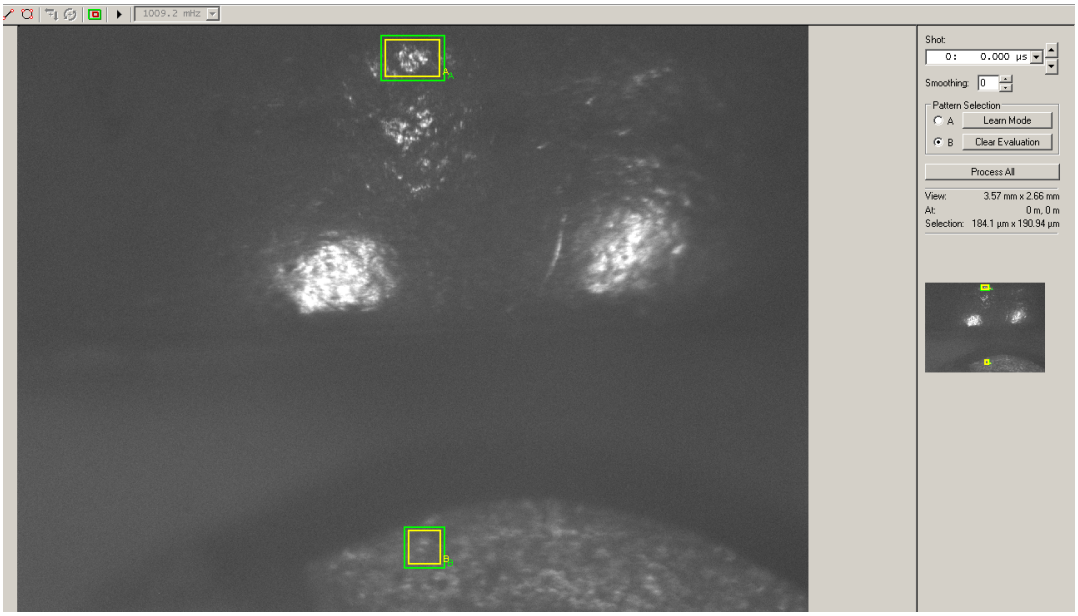


**Figure 5-28: Mass-spring system as imaged by the vibrometer lens at 2.5x magnification**

The result of the test is shown in Figure 5-29 and Figure 5-30. It is possible to notice that the displacement of the mass fixed to the actuator is very small compared to the displacement of the moving mass. As a consequence, the differential displacement curve is very close to the moving mass displacement curve. We can clearly recognize a peak around *11 Hz*. In order to further increase the accuracy of the measurement, a new test, with smaller frequency step is needed.

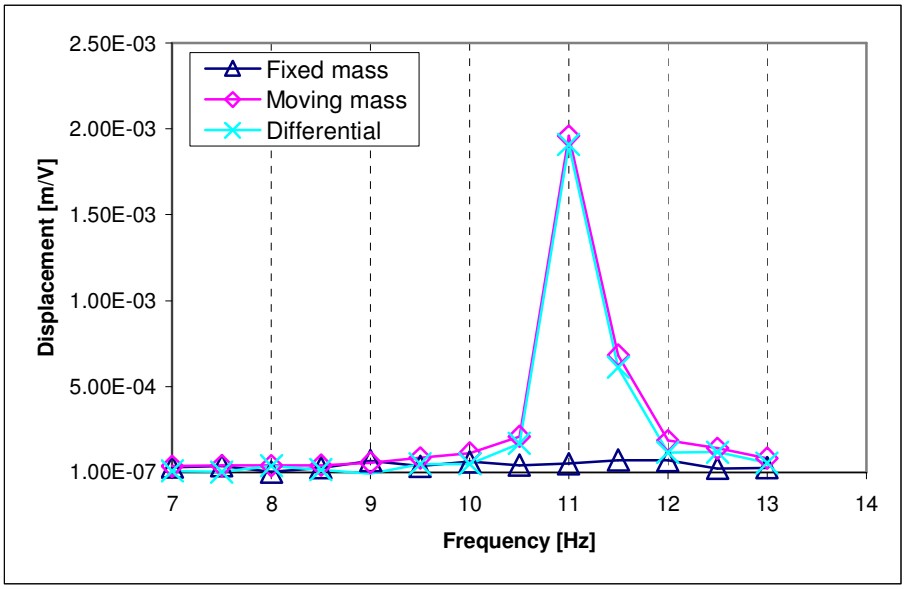


**Figure 5-29: Displacement plot 7-13 Hz bandwidth test**

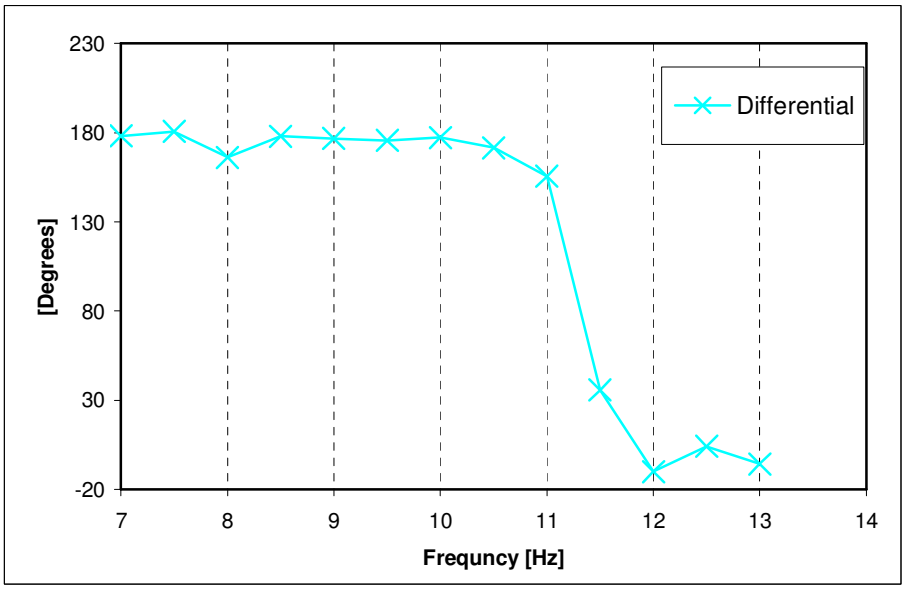


**Figure 5-30: Phase plot 7-13 Hz bandwidth test**

The parameters of this new measurement are listed in Table 9. This time the bandwidth is *10-12 Hz* and the frequency step is *0.1 Hz*.

| | |
|---|---|
| ***Bandwidth*** | *10-12 Hz* |
| ***Initial period length*** | *1/10 s* |
| ***Settling time*** | *5000 ms=5 s* |
| ***Frequency Step*** | *0.1 Hz* |
| ***Shots per period*** | *36* |
| ***Voltage Amplitude*** | *0.2 V* |
| ***Voltage Offset*** | *0.1 V* |
| ***Magnification*** | *2.5x* |

**Table 9: 10-12 Hz bandwidth Test Parameters**

The results of this test are shown in Figure 5-31 and Figure 5-32. We can see that if we decrease the bandwidth and the frequency step, we can measure the resonance frequency with better resolution. Moreover, the peak of the displacement increases as well since we go closer and closer to the resonance frequency.

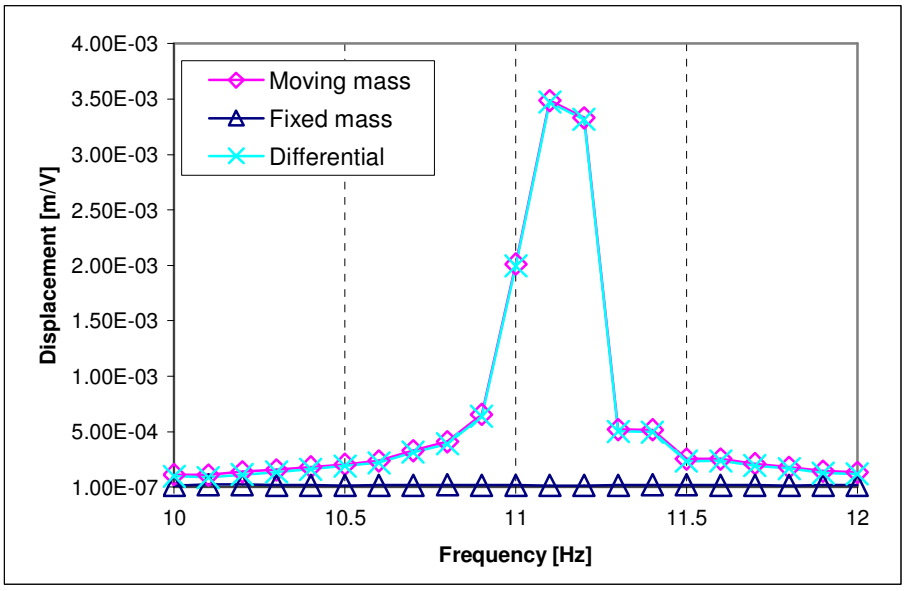


**Figure 5-31: Displacement plot 10-12 Hz bandwidth test**

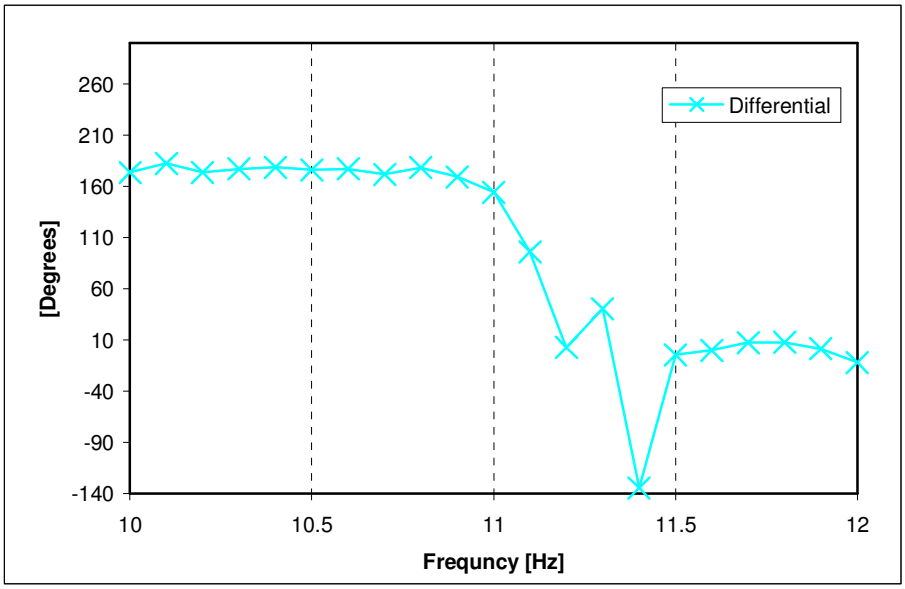


**Figure 5-32: Phase plot 10-12 Hz bandwidth test**

The accuracy can be further increased by decreasing the frequency step in the settings. This is what has been done for the next measurement. The parameters of this new measurement are listed in Table 10.

| | |
|---|---|
| ***Bandwidth*** | *11.00-11.30 Hz* |
| ***Initial period length*** | *1/11 s* |
| ***Settling time*** | *5000 ms=5 s* |
| ***Frequency Step*** | *0.02 Hz* |
| ***Shots per period*** | *36* |
| ***Voltage Amplitude*** | *0.2 V* |
| ***Voltage Offset*** | *0.1 V* |
| ***Magnification*** | *2.5x* |

**Table 10: 11.00-11.30 Hz bandwidth, 2.5x magnification Test Parameters**

The results are shown in Figure 5-33 and Figure 5-34. With this last measurement we reached an accuracy of *0.02 Hz* in measuring the resonance frequency of the system.

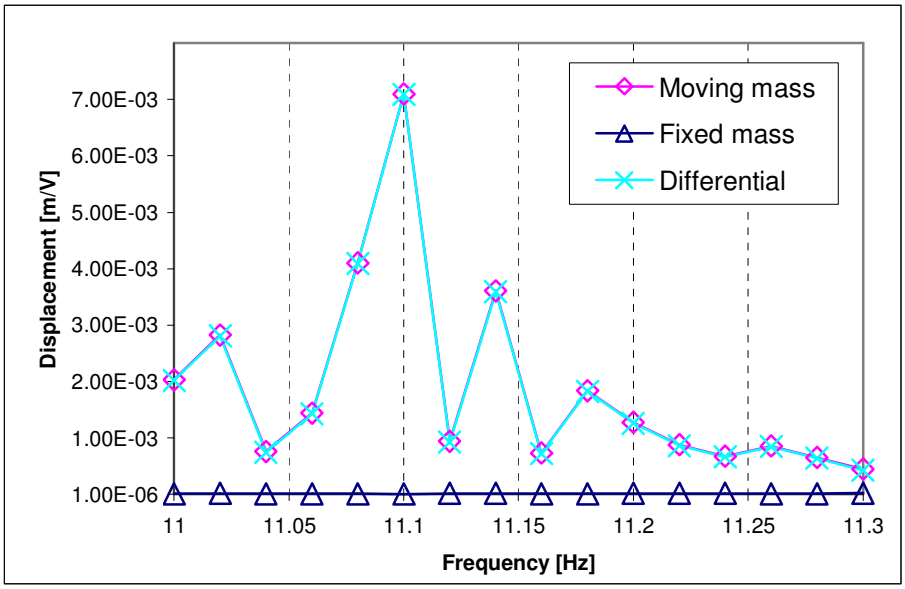


**Figure 5-33: Displacement plot 11.00-11.30 Hz bandwidth test**

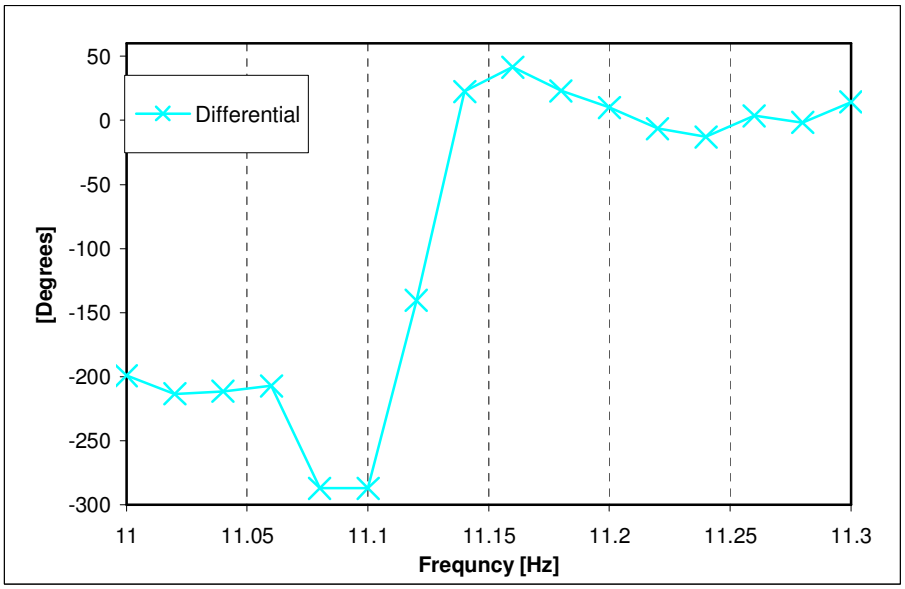


**Figure 5-34: Phase plot 11.00-11.30 Hz bandwidth test**

At this point, one last test has been performed; this measurement has the same bandwidth and frequency step as the previous one but a *10x* magnification lens will be used. Since this is the lens that will be used for the test of the gradiometer, we needed to check that this lens is as reliable as the *2.5x* magnification lens. Only the moving mass can be visualized with this magnification, so no differential measurement can be performed this time. The parameters used for this test are listed in Table 11.

| | |
|---|---|
| ***Bandwidth*** | *11.00-11.30 Hz* |
| ***Initial period length*** | *1/11 s* |
| ***Settling time*** | *5000 ms=5 s* |
| ***Frequency Step*** | *0.02 Hz* |
| ***Shots per period*** | *36* |
| ***Voltage Amplitude*** | *0.02 V* |
| ***Voltage Offset*** | *0.01 V* |
| ***Magnification*** | *10x* |

**Table 11: 11.00-11.30 Hz bandwidth, 10x magnification Test Parameters**

The results of this test are shown in Figure 5-35, Figure 5-36.

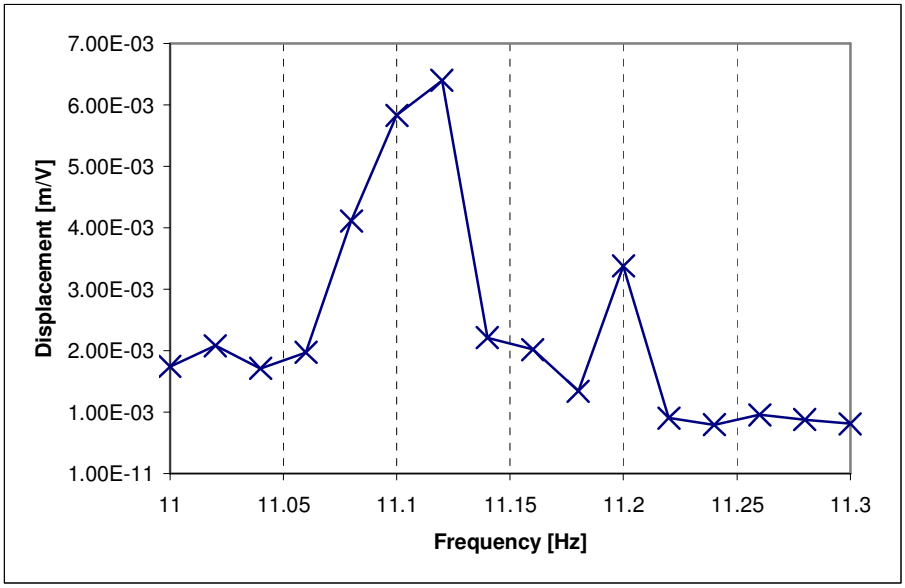


**Figure 5-35: Displacement plot 11.00-11.30 Hz bandwidth test, 10x lens**

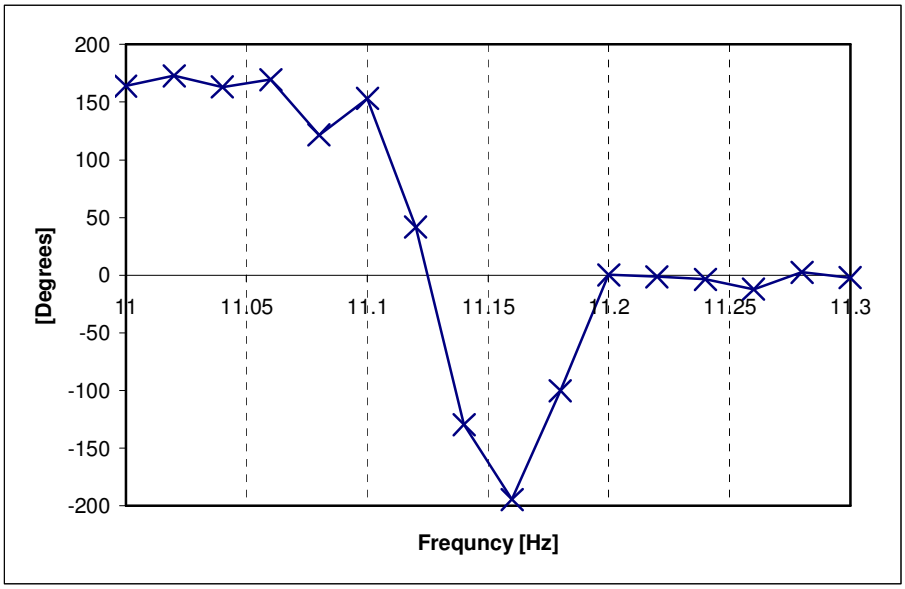


**Figure 5-36: Phase plot 11.00-11.30 Hz bandwidth test, 10x lens**

Finally we can compare the results of the two tests with different magnification; the comparison is shown in Figure 5-37.

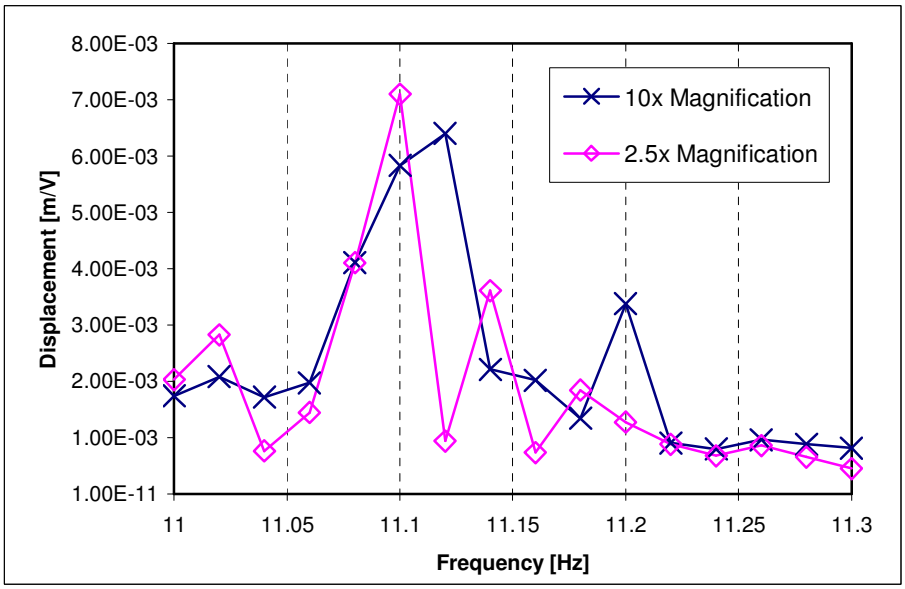


**Figure 5-37: Comparison 10x magnification test, 2.5x magnification lens**

The difference between the two graphs may be due to a focus problem. Another conclusion we can draw is that, according to the phase diagram of the previous measurement, the peak should be at *11.12* instead of *11.10*. This last measurement seems to confirm it.

### 5.5.2. Parameters measurement

As a final step, an attempt to calculate the parameter of the system has been done. In order to calculate the parameters a matlab script written by Cuperus, was used. The script uses a fitting technique based least square criterion [37].

The method described in this paper is based on Least Square Criterion. Let us consider a physical discrete system (it can be described by a finite set of discrete parameters in any of its states). Let $\bar{x} = \{x^1, ..., x^m\}$ be the values of a parameter set. In this formulation the parameter set contains both known data (measured data) and unknown (parameters).

Physical theories impose constrains to the possible values of the parameter: the constrains can take the form of functionals:

$$\bar{f}(\bar{x}) = 0 \tag{5.3}$$

In most usual cases it is possible to define a partition to the set of parameters such as:

$$\bar{x} = \begin{bmatrix} \bar{d} \\ \bar{p} \end{bmatrix} \quad or \quad \bar{d} = \bar{g}(\bar{p}) \tag{5.4}$$

Where $\bar{d}$ is a data set vector, $\bar{p}$ is a parameter vector and $\bar{g}$ is a linear operator. Equation (5.3) can be written as:

$$\bar{f}(\bar{x}) = \bar{d} - \bar{g}(\bar{p}) \tag{5.5}$$

Where $\bar{f}(\bar{x})$ assumes the form of a non-linear relationship.

In our case the data vector is a discrete vector, $d^i$, and the parameter vector is a continuous vector $p(r)=p(\omega_n,\zeta)$. Equation (5.4) can be written as:

$$d^i = g^i\left[p(r)\right] \tag{5.6}$$

The data (measurement) vector can be described by a discrete vector of expected data, $\bar{d}_0$, and a covariance matrix, $C_{d_0 d_0}$. If we have any a-priori knowledge of the function, $\bar{p}_0(r)$, we describe it with a function of expected value, $p_0(r)$, and a covariance matrix, $C_{p_0 p_0}(r, r')$.

If we assume null covariance between $\bar{d}_0$ and $\bar{p}_0(r)$, the covariance operator is:

$$C_0 = \begin{bmatrix} C_{d_0 d_0} & 0 \\ 0 & C_{p_0 p_0} \end{bmatrix} \tag{5.7}$$

In order to compute the values of the parameter we have to minimize the argument of the exponential:

$$\rho(x) = const \cdot \exp\left\{-\frac{1}{2}\left(\overline{x} - \overline{x}_0\right)^T \cdot C_0^{-1} \cdot \left(\overline{x} - \overline{x}_0\right)\right\} \tag{5.8}$$

Equation (5.8) represents the Gaussian probability density function. The algorithm allowing the calculation of $\hat{d}$ and $\hat{p}$ (components of the vector $\hat{x}$ which minimize the exponential of the Gaussian density function) is:

$$\hat{\overline{p}}_{k+1} = \overline{p}_0 + C_{p_0 p_0} \cdot G_k^T \cdot \left(C_{d_0 d_0} + G_k \cdot C_{p_0 p_0} \cdot G_k^T\right)^{-1} \cdot \left[\overline{d}_0 - \overline{g}\left(\hat{\overline{p}}_k\right) + G_k \cdot \left(\hat{\overline{p}}_k - \overline{p}_0\right)\right] \tag{5.9}$$

In our case we have that:

$$g = \frac{1}{\sqrt{\left[\left(1 - \frac{\omega}{\omega_n}\right)^2\right]^2 + 4\zeta^2\left(\frac{\omega}{\omega_n}\right)^2}} \tag{5.10}$$

That is the same as equation (3.35). And $G_k$ is the matrix of the partial derivatives of g, defined as:

$$G^{i\alpha} = \partial g^i / \partial p^\alpha \tag{5.11}$$

The iteration process stops when the values $\left(\hat{\overline{p}}_{k+1} - \overline{p}_0\right)$ (defined as Total Corrections) are small enough.

Figure 5-38 shows the result of this procedure: the crosses represent the measured values while the continued line is the resulting curve from the fitting technique.

From the curve we can get the values of the following quantities:

$$\omega_n = 69.6767 \quad [rad / sec]$$
$$\zeta = 0.0015$$

Moreover it is possible to can calculate the following parameters:

$$Q = \frac{1}{2\zeta} = 333.33 \tag{5.12}$$

And, using the measured value of the mass of the screw (*m=1.0118 g*), the spring constant is:

$$k = \left(\omega_n\right)^2 \cdot m = 4.863 \quad [N / m] \tag{5.13}$$

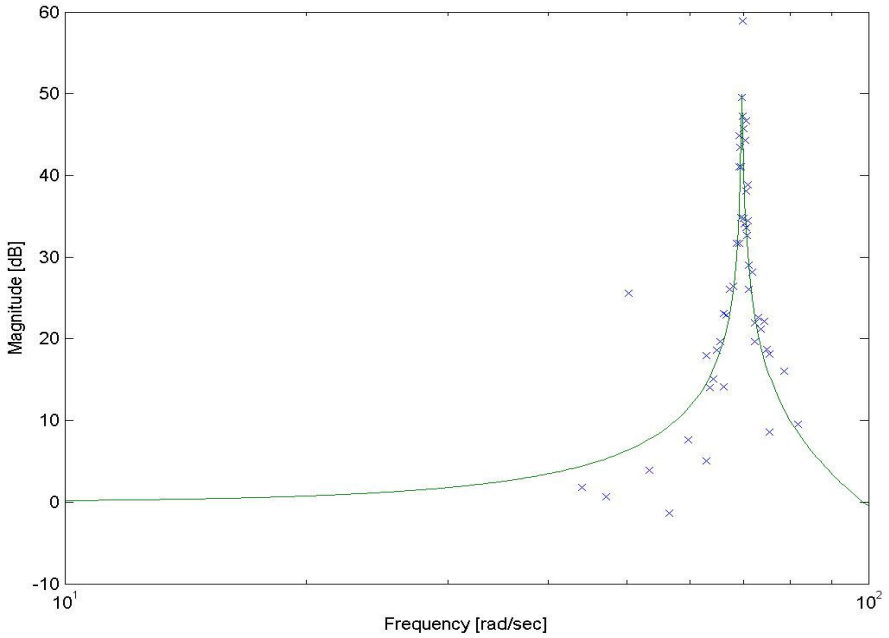


**Figure 5-38: Fitting diagram against measured diagram**

Finally we can feed the values calculated into a matlab script in order to check the reliability of the fitting technique. Figure 5-39 shows the comparison between the measured points, the fitting curve and the bode diagram obtained with the matlab script. It is possible to see that the two curves are almost superimposed.

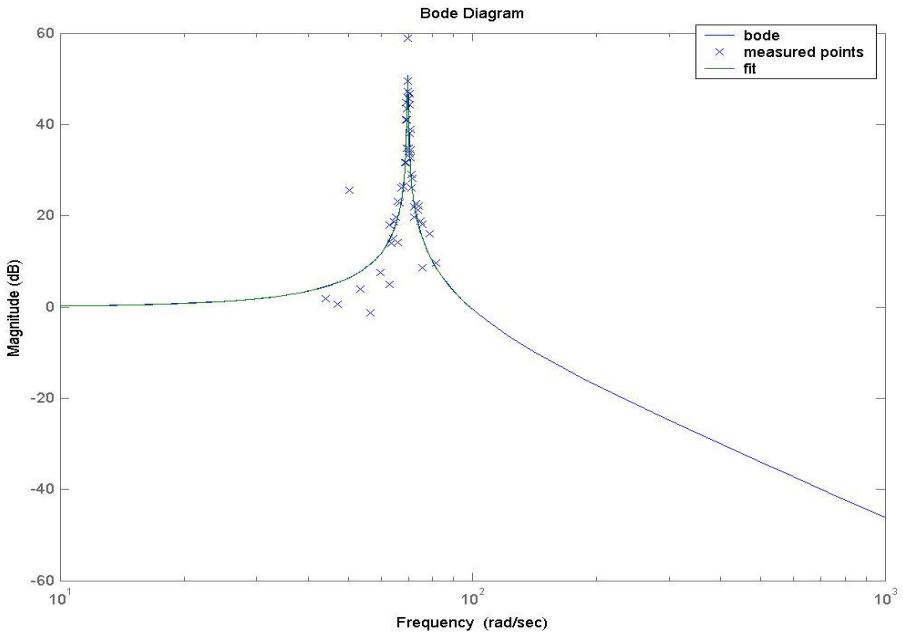


**Figure 5-39: Comparison between measured values, fitting curve and bode diagram**

# 6. Conclusions and Outlook

A test setup has been designed and assembled in order to perform mechanical tests on a MEMS based micro gravity-gradiometer. The requirements for the test set up are:

- Vacuum tests: the tests have to be performed below $10^{-3}$ *mbar*.
- In-plane actuation.
- Low frequency actuation: frequency bandwidth *1-10 Hz*.
- Small displacements: fraction of $\mu m$.
- High precision capture and analysis of motion.

The designed setup is composed of the following elements:

- Vacuum chamber. It comprises electrical connection, a feed-through for a thermocouple, a pressure sensor and connector to the vacuum turbo pump.
- Piezo-electric based actuator to perform in plane motion.
- Supporting structure to connect the actuator to the silicon wafer and keep it in the right distance from the lens of the imaging system.

The image analysis system selected is a Micro System Analyzer for MEMES. The system is primarily designed for high frequency vertical actuation. Nevertheless, it can be still used for our purposes. Two different kinds of tests might be performed using this system: step response, and frequency sweep.

The step response test would not be affected by problems due to the small gap between the moving masses and the frame but would take a very long time to be completed. This depends on the acquisition software: it acquires only one measurement every period. If the period is long, as in our case, being our system highly underdamped, the test could take several hours (up to 12) to be completed.

The other option is represented by the frequency sweep test. This kind of test does not present software limitation but, due to the small gap and the high $Q$ of the system, it requires a very small input displacement in order to properly measure output displacements at resonance frequency. Another main advantage of this sort of test is the possibility of performing differential measurements. In this way it is possible to insulate the movement of the masses from the movement of the frame, reducing, hence, movements due to external noise.

After the assembly, the test setup has been validated with the following results:

*Vacuum tests:*

The system does not present leakage and the out-gassing procedure has been defined. In order to keep the value of the pressure under the value of $10^{-3}$ *mbar* for a time sufficient for a test (a couple of hours), the setup has to be heated with a thermal wire at *80°C* for a period close to 48 hours.

*Quasi Static measurements:*

The quasi static (DC) behavior of the piezo-electric actuator is dominated by hysteresis. The maximum hysteresis is approximately *17%* for the whole stroke length and about *12%* for loops. These values are rather small and will not interfere with the measurements.

*Dynamic measurements:*

The dynamic behavior of the whole setup presents a linear behavior in the frequency bandwidth *1-100 Hz*, a peak due to intrinsic resonance of the actuator is present at *340 Hz*. After this peak the system presents an extremely chaotic behavior due to the exited vibration modes of the structures that compose the setup. Two different wafer holder structures have tested. They differ by their dimensions (and hence, by their masses). The thickest wafer holder has demonstrated to be the more reliable for our tests due to its higher stiffness.

*Re-polarization:*

The high temperature used for the out-gassing process causes depolarization in the piezo-electric elements of the actuator. A re-polarization process needs to be performed every time before starting a new test.

*Noise characterization:*

The analysis of the two main noise sources (environmental and electrical) shows that the environmental noise is dominant in the low frequencies range while the electrical noise is dominant in the high range. In our case, the level of noise is the limiting factor for a displacement measurement. The graph in Figure 5-26 shows the resolution of the system in terms of maximum measurable $Q$ at each frequency. It is possible to see how, at *5 Hz*, the maximum measurable $Q$ is approximately $5x10^3$. The graph also shows that a reduction of the noise level of one order of magnitude is translated in a increment of measurable $Q$ of one order of magnitude.

*Test simulation:*

From a test simulation with a system with low resonance frequency, it has been possible to verify that we can actually measure resonance frequency with 0.02 Hz accuracy and, thanks to fitting technique based on last square criterion [37], it has been possible to calculate all the characteristic of the system.

## *Recommendations*

- A software update can be required to the manufacturing company of the Micro Analyzer in order to perform step response test in a reasonable time. The software update should allow the performance of more measurement during the same period.
- Frequency sweep measurement can be refined by increasing the settling time. This will lead to a cleaner and more precise measurement.
- Reducing environmental noise, by choosing a more quiet location or using active damping, will increase the higher measurable $Q$ and reduce uncertainty in measurements.

## *Outlook*

The influence of pressure on the micro gravity-gradiometer should be verified by performing tests at atmospheric pressure (*1 bar*) as well as tests in vacuum, and compare their results.

The system will be very suitable for tests on the complete MEMS based micro gravity-gradiometer design (with electrical read-outs included). This test situation will be different from the situation for purely mechanical test.

- The masses will be held fixed with a feedback control while an external signal is applied. The small gap between masses and frame will not be an issue anymore. This time a very small signal is not a requirement anymore. The actuator, anyway, is able to provide a signal with enough power for this new situation.
- The electrical connection can be easily integrated in the setup without changes in the design: the electric plug has 7 pins and only 3 of them are currently used for electrically connections.

# Bibliography

[1] http://www.microned.nl
[2] A. De Simone; Theoretical background for a gravity field determination mission on Europa; Literature Research Report; Technical University of Delft; 2008
[3] H. Chan, H. Paik; Superconductive gravity gradiometer for sensitive gravity measurements. I. Theory; University of Maryland; Physical Review D; 1987
[4] R.Klees; Planetary Gravity Field Handbook, 2007, DEOS Department, Delft University of Technology
[5] P.W.L. van Barneveld; Europan Tidal Deformation: Providing theoretical framework for altimetry data to determine ocean presence; MSc Thesis Report, 2005, Delft University of Technology
[6] R R. Rummel, Department of Geodesy; Satellite Gradiometer; Delft Univ. of Technology; 1986
[7] R. Koop, J. Bouman, M. Smit, A. Selig, T. Zegers, J. Haanstra, R. Cuperus, R. Wiegerink, J. Flokstra, B. Vermeersen, P. Visser, A. V.d. Berg; Prospect for a Gradiometry Mission for High-resolution mapping of the Martian Gravity Field; 2006
[8] M. Blanc, S. Sasaki, M. Fujimoto, R. Pappalardo, L. Zelenyi; LAPLACE, a mission to Europa and Jupiter's system for ESA's Cosmic Vision Program
[9] J. Anderson et al.; Europa's differentiated internal structure: Interface from four Galileo encounters; Science 281:2019-2022; 1998
[10] Dessler; Physic of the Jovian Magnetosphere; Cambridge University Press; 1983
[11] Kilverson; Galileo Magnetometer measurements: a stranger case for a subsurface ocean at Europa; Science 289; 2000
[12] Morrison at al.; Satellites of Jupiter. University of Arizona Press; 1982
[13] W.M.Grundy, B.J.Buratti, A.F. Cheng; New Horizons Mapping of Europa and Ganymede; Science, 318: 234-237
[14] X. Jiang, F. Wang, M. Kraft, B. E. Boser; An integrated Surface Micromachined Capacitive Lateral Accelerometer with 2μG/√Hz Resolution; University of California at Barkely, Southampton University; 2002
[15] M. Elwenspoek, R. Wiegerink; Mechanical Microsensors; 2001
[16] N. Yazdi, F. Ayazi, K. Najafi; Micromachined Inertial sensors; Proceeding of the IEEE, Vol. 86; 1998
[17] Reinder Cuperus, Gravity Gradient Sensor Technology for future planetary missions; Master Thesis; University of Twente, 2005
[18] J. Flokstra, R. Cuperus, R. Wiegerink, J. Sesé, H. Hemmes, C. Sotin; Gravity gradient sensor technology for future planetary missions, Deliverable 4; University of Twente, Univerité de Nantes; 2005
[19] A. Peters, K.Y. Chung, S. Chu; High-precision gravity measurements using atom interferometry; Metrologia; 2001, 30, 25-61
[20] M.V. Moody, H. Paik, R. Canavan; Three Axis Superconductive Gravity Gradiometer for sensitive gravity experiments; Review of scientific instruments, vol. 73; 2002
[21] H.J. Paik, Superconducting Accelerometer, Gravitational-Wave Transducers and Gravity Gradiometer; University of Maryland, U.S.A; 1996
[22] Ho Jung Paik, John M.Lumley; Superconductive gravity gradiometer on STEP e GEM; Dept. of physic, Univeristy of Maryland; Oxford Instruments Cambridge
[23] http://sci.esa.int/science-e/www/area/index.cfm?fareaid=107

[24] N. Yu, J.M. Kohel, J. Ramerez-Serrano, J. R. Kellogg, L. Lim and L. Maleki; Progress Towards a space-borne quantum gravity gradiometer; Jet Propulsion Laboratory, California Institute of Technology;
[25] L. Zhang, D. Cho, H. Shiraishi, W. Trimmer; Squeeze film damping in micromechanical systems; ASME, Micromechanical Systems, DSC-vol. 40; 1992
[26] M. Bao, H. Yang; Squeeze film air damping in MEMS; 2006
[27] R. Christian; The theory of oscillating-vane vacuum gauges; Vacuum 16; 1966
[28] J. Shearer, B. Kulakowski, J.Garden; Dynamic modeling and control of engineering systems; Prantice Hall; 1997
[29] Structural testing, part 1 and 2; Brüel & Kjær Handbook; Denmark
[30] J. Marion, S. Thornton; Classical Dynamics of particles and systems; Saunders College Publishing; 1995
[31] nanoX200 datasheet; Piezosystem Jena
[32] 30V300 1-channel OEM Amplifier datasheet; Piezosystem Jena
[33] N.Setter; ABC of Piezoelectricity and Piezoelectric materials; Ceramic Laboratory, EPFL, Lausanne, Switzerland
[34] M.Lines, A. Glass; Principles and applications of Ferroelectrics and related materials; Clarendeon; Oxford, 1979
[35] MSA-400 Micro System analyzer User Guide; Polytec
[36] D. Damjanovic; Hysteresis in Piezoelectric and Ferroelestic materials; Swiss Federal Institute of technology EPLC, Lousanne, Switzerland
[37] A. Tarantola, B. Valette; Generalized non linear problems solved using last square criterion; Institut eu Phisique du globe de Paris; 1982
[38] R.Cuperus et al.; to be published elsewhere
[39] http://en.wikipedia.org/wiki/Mean_free_path, http://en.wikipedia.org/wiki/Vacuum